DEPARTMENT OF PHYSICS AND ASTRONOMY
HEIDELBERG UNIVERSITY

MASTER THESIS IN PHYSICS

High-Resolution Optics for Modular Quantum Simulation

Submitted by:
Micha BUNJES
born in Herrenberg, Germany

Supervisor:
Prof. Dr. Selim JOCHIM

This Master Thesis has been carried out by

Micha BUNJES

at the

Physikalisches Institut Heidelberg

September 26, 2022

"Physics is like sex: Sure, it may give some practical results, but that's not why we do it."

Richard P. Feynman

Abstract

Heidelberg Quantum Architecture (HQA) is a new quantum simulator built to study the emergence of quantum phenomena in few to many-body systems. To pave the way for versatile quantum simulation, a modular concept is introduced that allows full utilization of optical systems. At the heart of the custom-designed mounting structure lies a high-resolution objective acting as a fixed optical reference. To verify the performance enabled by a numerical aperture of 0.66, a modular test bench and a sub-resolution nanopore device are used to scan the point spread function of this objective across the entire field of view, resulting in a minimum measured resolution of $704(31)$ nm. In addition, the angle between the mechanical and optical axis is measured at $0.13(9)°$. More properties like aberrations are investigated by their impact on the mounting process.

A crucial goal of HQA is an increased experimental cycle rate. To this end, a new proposal aims to accelerate the preparation of few-particle systems using a blue-detuned ring trap to increase local density and thermal scattering rate. After evaporation in this trap, the thermalization of atoms into a tight optical tweezer could be optimized. Two experimental solutions using axicons and Moiré lenses are explored.

Zusammenfassung

Heidelberger Quantum Architecture (HQA) ist ein neuer Quantensimulator, der entwickelt wurde, um die Entstehung von Quantenphänomenen in Wenig- bis Vielteilchensystemen zu untersuchen. Um den Weg für eine vielseitige Quantensimulation zu ebnen, wird ein modulares Konzept eingeführt, das die volle Nutzung optischer Systeme ermöglicht. Das Herzstück der maßgeschneiderten Montagestruktur ist ein hochauflösendes Objektiv, das als feste optische Referenz dient. Zur Überprüfung der optischen Leistung, die durch eine numerische Apertur von 0.66 ermöglicht wird, werden ein modularer Prüfstand und eine Nanopore, die kleiner als die Auflösung ist, verwendet. Dadurch wird die Punktbildfunktion dieses Objektivs über das gesamte Sichtfeld gescannt, was zu einer minimal gemessenen Auflösung von $704(31)$ nm führt. Darüber hinaus wird der Winkel zwischen der mechanischen und der optischen Achse mit $0.13(9)°$ gemessen. Weitere Eigenschaften wie Aberrationen werden durch ihre Auswirkungen auf den Montageprozess untersucht.

Ein wesentliches Ziel von HQA ist die Erhöhung der experimentellen Taktrate. Zu diesem Zweck zielt ein neuer Vorschlag darauf ab, die Präparation von Systemen mit wenigen Teilchen zu beschleunigen, indem eine blau verstimmte Ringfalle verwendet wird, um die lokale Dichte und die thermische Streuungsrate zu erhöhen. Nach Evaporation in dieser Falle könnte die Thermalisierung der Atome in eine enge optische Pinzette optimiert werden. Zwei experimentelle Lösungen mit Axicons und Moiré-Linsen werden untersucht.

Contents

List of Abbreviations

HQA	**H**eidelberg **Q**uantum **A**rchitecture
MOT	**M**agneto **O**ptical **T**rap
CAD	**C**omputer **A**ided **D**esign
DMD	**D**igital **M**icromirror **D**evice
AOM	**A**cousto **O**ptic **M**odulator
ODT	**O**ptical **D**ipole **T**rap
MT	**M**icro **T**rap
PSF	**P**oint **S**pread **F**unction
RMS	**R**oot **M**ean **S**quare
PV	**P**eak to **V**alley
FOV	**F**ield **O**f **V**iew

1 Prologue

This thesis introduces the newest developments in the late quantum simulation experiment, *Heidelberg Quantum Architecture* (HQA), currently under construction at Heidelberg University. Building on a solid foundation of experience gained by active exchange with running experiments, this new apparatus promotes a simplified, versatile, and accessible way of conducting quantum simulations. HQA aims to gain new knowledge of the complex quantum regime. With its many counterintuitive properties, quantum physics governs most natural phenomena in the everyday world, and new knowledge in this still unfamiliar field provides the groundwork for many technological advancements. Famous examples are, among others, the USB flash drive, magnetic resonance imaging (MRI), or the quantum tunneling of electrons in basic light switches.

The impact of quantum physics on the emergence of structural phenomena in many-body systems is an exciting topic for HQA since it allows the study of novel material structures. To this end, this thesis deals with the basics of preparing quantum systems, ranging from few to many-body states. Discussed are not only the theoretical advantages of the particles used in the experiment but also the technical realization of preparing these particles in scientifically exciting states. The subsequent chapters discuss two crucial aspects of the experiment. First, since the high-resolution optics of HQA provide a powerful view into the simulated quantum states, they are the subject of close examination. Second, the fourth chapter motivates high cycle rates in a quantum simulator and proposes a new atom state preparation by building upon previous work and improving the experimental cycle time.

1.1 A Partial History of Optics

The subject of optical physics has been a part of human history for a long time already. During the last centuries, people continuously strived to perceive the world in greater detail than the human senses allow. Of all senses, humans assign the most value to eyesight [1]. It provides the human brain with valuable information about the surrounding world, like distances between and toward objects or the color of materials, i.e., the wavelength distribution of light reflected by a material [2]. Unfortunately, since the eye is not spared from aging in the human body, its performance degrades over time, resulting in medical diseases like presbyopia, which impedes

the ability to put close objects in focus. In the past, such shortcomings of the human body pushed curious people toward the research of optical systems like sight-correcting spectacles [3].

Similarly, the interest in objects beyond the earth's atmosphere, e.g., stars or the planets, sparked the development of optical tools like the astronomical telescope. In the 17th century, Galileo Galilei developed the first refracting telescope, and later Isaac Newton built the first reflecting telescope [4]. These basic optical systems laid the groundwork for optical assemblies like Galilean or Keplerian beam expanders, which are basic two-lens setups still used in physics labs today.

Over the last centuries, optical systems evolved from the most elementary setups to more advanced designs, which can image the natural world with a level of detail that the human eye cannot achieve. Indeed, humanity started experimenting with visual abilities many centuries ago. For example, the first mention of lens-like objects connects to a Greek comedy dated roughly 423 BC [5]. Here, it was mentioned how glass or crystal allowed the melting of wax on a table. Likewise, Roman Seneca was the first to mention the use of a magnifying lens in the first century. He discovered that a water bowl could be used to magnify letters [6]. Later, this phenomenon would be described by a change in the refractive index in materials.

A significant invention was developed later when the first eye-correcting lenses appeared in the 13th century, aiding the diminishing eyesight that comes with age [5]. However, only in time was more effort put into a deeper understanding of the nature of light. For example, at the beginning of the 17th century, Kepler understood how geometric optics explained the forming of an optical image by a refracting lens. Using this understanding, the development of telescopes followed, combining two lenses to magnify distant images. These devices had a fundamental influence on the scientific world. Astronomic discoveries, for instance, caused the shift away from the geocentric worldview [7].

Another prominent application for the optical lens is a photographic camera system. The first concept of a photographic camera can be connected to the camera obscura. Initially, such a device used a hole in a wall to project images of the exterior world onto a plate. The first concepts appeared around the 13th century by Roger Bacon or later in the 15th century when Leonardo da Vinci discovered the similarities between the human eye and the camera obscura, for which the advantages of refracting elements like lenses were also discovered [8]. These lenses were able to create more precise and more magnified images.

Concurrently with the development of telescopes, the newest understandings in optical theory were used to study the small details of nature or, in other words, to develop the first microscopes. A *microscope* could be defined as a device that allows a more detailed look into nature than the human eye. While resolving patterns like a black letter on a white background, the human eye retains an angular resolution

of roughly 0.08°. So, for an object of interest at a 10 cm distance, the human eye can resolve structures as small as 0.15 mm [2]. Any optical system allowing the observation of smaller structures would then be a microscope.

Some of the first microscopes appeared during the 16th century in Italy and were further developed during the 17th century. During this time, curious scientists made many fundamental discoveries. A few examples are the law of refraction by Snell or the principle of Fermat describing light propagation in materials. These discoveries were followed by progressively advanced microscopes [9]. For instance, the first constructions of achromatic lenses improved the optical quality by correcting for different colors [10]. However, even though these devices achieved magnifications allowing the observation of objects as large as a few micrometers, they were still limited in their usability, magnification, and optical performance compared to current microscopes.

Optical lenses shaped by countless iterations of design work by optical engineers are available today. The various lens types range from carefully designed microscope objectives to complex and flexible photography objectives with tunable properties. Furthermore, one can customize specific optical components depending on applications like macro photography or oil immersion microscopy. Indeed, it is possible to manufacture microscope objectives that can detect single atoms, which are used in advanced physics research projects like quantum simulation [11, 12].

1.2 Quantum Simulation

For a few decades, a new way of studying the properties of small-scale structures in the physical world has been gaining popularity. Physics is often seen as a science dedicated to taking the mechanisms of the natural world and reducing them to elementary laws. This approach has led to many technological breakthroughs and contributed to the general understanding of the universe. One famous example is the Schrödinger equation, describing the non-relativistic behavior of a quantum mechanical system. For instance, one fascinating system is the atom, the microscopic particle which builds up common materials. The Schrödinger equation describes our everyday world in great detail, yet solving it for a number of particles larger than about ten is impossible for the latest iterations of classical computers [13].

On the other hand, large systems in the many-body limit can be approximated with averaged quantities and simplifying assumptions. Thermodynamics is a well-known example of this. However, the required calculation power surges exponentially for systems in between. Consequently, it makes sense to bridge the gap from describing small systems with few particles to understanding the functionality of more complex and macroscopic many-particle systems like superconductors or proteins. Studying this gap can reveal much about how larger particle ensembles behave and what arrangements they form. Moreover, any discovery might have severe implications for systems on a larger scale.

Here, the concept of quantum simulation enters. Similarly to how aerodynamics can be studied with wind tunnels, quantum simulators allow the study of quantum dynamics [14]. However, since quantum systems with many particles are too demanding for the classical computational method, a quantum simulator takes a more physical approach. Instead of calculating the formulas directly, it simulates these systems using atoms in a controlled environment. A quantum simulator then allows the deterministic preparation of systems with atoms, from a few single to many hundreds [15]. For this, ultracold atoms at temperatures close to absolute zero pose a great platform. In a vacuum, these particles are isolated from their environment and offer many ways to be manipulated. Interparticle interactions, for example, can be tuned with external magnetic fields, and optical laser potentials can manipulate their local confinement [16]. These tools enable the modeling of the quantum properties of particles, which make up real-world systems. A quantum simulator can tackle pressing questions in quantum physics, with many possible applications, such as nitrogen-fixing or the development of new battery materials [14].

The concept of quantum simulation has been around for a few decades. Past experiments have already studied systems with a wide range of complexity and produced exciting results. From a basic demonstration of the wave-particle duality by tunneling single atoms in 1D potentials to the central problem of high-temperature superconductivity [17], quantum simulators have already come a long way. Still, many questions about quantum phenomena like superconductors or superfluidity remain to be answered. To take the knowledge acquired from current quantum experiments and develop the next iteration of the quantum simulator, we present *Heidelberg Quantum Architecture* (HQA).

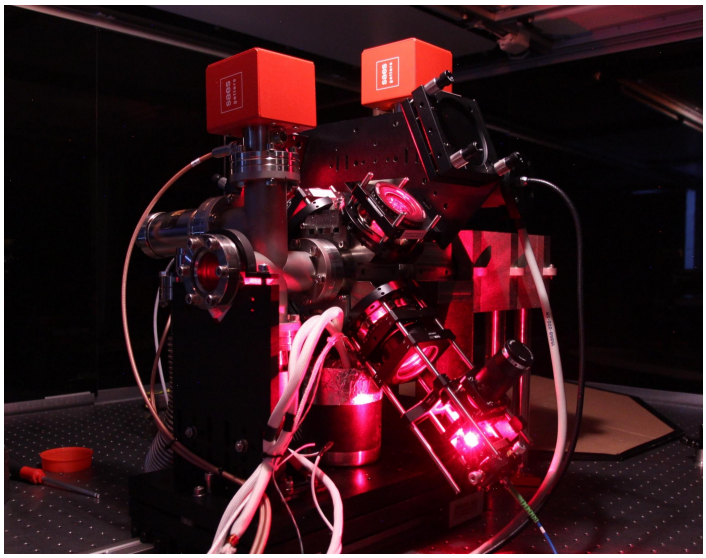

FIGURE 1.1: PICTURE OF HQA, CURRENTLY UNDER CONSTRUCTION. This long exposure picture of HQA was recorded in the lab in May 2022.

2 HQA - Quantum Simulation with Modular Interfacing

This chapter will describe the Heidelberg Quantum Architecture (HQA) quantum simulator in more detail. First, a general overview introduces Lithium-6 as the particles used in the experiment. Additionally, the concept behind the experimental setup and, in more detail, the optical setup will be discussed.

As motivated by the previous chapter, HQA is a quantum simulator designed to study complex quantum systems allowing the assembly of many-body states. As the fundamental building block of these systems, HQA utilizes fermionic atoms. Fermions follow the Fermi-Dirac statistics, which utilizes quantum mechanics to describe systems of many such particles. Moreover, fermions are fundamental building blocks of physical matter. Prominent examples of fermions are, for example, protons and neutrons. Further, any compound particle, e.g., an atom consisting of an odd number of fermions, is itself a fermion. Therefore, HQA uses fermionic atoms to perform simulations of fermionic systems.

Another example of a fermion is the electron. Due to its fermionic nature, its behavior in quantum mechanical systems can be simulated with fermionic atoms. A relevant phenomenon of interest is, for instance, that of superconductivity. In a superconducting material, electrons develop so-called cooper pairs, which are weakly interacting pairs of electrons. Their state can be described by a Bardeen-Cooper-Schrieffer (BCS) state, which describes a superconducting state with cooper pairs [18]. With fermionic atoms, a similar state and pairing of particles can be observed [19]. Consequently, atomic interactions in a quantum simulator are of particular interest.

A convenient atom species featuring such interactions is Lithium-6 (^{6}Li). This fermionic atom is the fundamental building block of quantum systems in HQA. The ^{6}Li isotope consists of three protons, three neutrons, and three electrons, which give the ground state configuration $1s^2 2s^1$ with a single valence electron. Therefore, the total spin is half-integer, and the atoms behave like fermions. Compared to other atoms, ^{6}Li offers many advantages for investigating quantum phenomena.

A valuable property of ^{6}Li are the controllable interactions between the single atoms. With a magnetic field, a Feshbach resonance of ^{6}Li atoms can be addressed [20], which allows continuous tuning of the interactions between the cold atoms

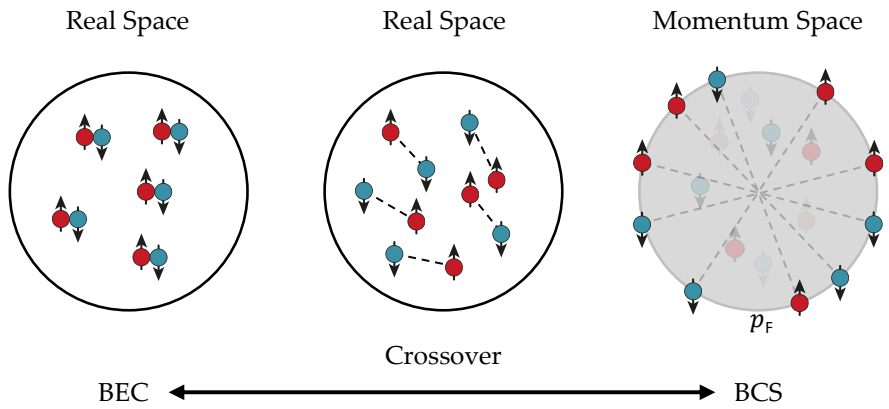

FIGURE 2.1: THE BEC TO BCS PHASE TRANSITION OF A FERMI GAS. In the BEC regime, ^{6}Li molecules behave like Bosons. The binding strength can be tuned smoothly from over the crossover region to the BCS regime. Here, Cooper pairs of atoms with opposite spin can form. These atoms have a momentum $|p_F|$ corresponding to the Fermi energy E_F. The interaction strength can be controlled continuously by a tunable Feshbach resonance.

across a wide range [21, 22]. Figure 2.1 shows the most exciting states with varying interaction strengths. A Bose-Einstein condensate (BEC) state can be realized by tuning the magnetic field so that atoms with opposing spin experience a strong binding force [23]. Here, the interaction between two ^{6}Li atoms with different spin states causes the forming of Feshbach molecules, which behave like bosons. From this state, the binding strength can be gradually lowered until a weakly interacting BCS state is reached. Such a state can also be found with electrons in a superconductor. Therein lies the flexibility of fermionic ^{6}Li. Thanks to the tunable interactions, the atoms can be manipulated to behave like weakly interacting cooper pairs or strongly bound bosons. In contrast, Bosonic particles cannot be tuned to interact like fermions.

Additionally, ^{6}Li atoms are a convenient tool for studying the emergence of quantum effects in the transition from few-particle to many-particle states [24]. The Pauli exclusion principle is a fundamental part of the Fermi-Dirac statistics describing fermions. It prevents fermions from occupying the same quantum state. In contrast, this does not apply to bosons. For example, when bosonic particles are cooled down to ultracold temperatures close to absolute zero, they will collectively occupy the lowest energy state [25]. This behavior is called Bose-Einstein condensation. Ultracold fermions, on the other hand, will fill up the energy states such that only two particles with opposing spin states occupy a single state. This behavior is illustrated to the left in Figure 2.2. This property of fermionic atoms allows the assembly of few-body systems from a state with many fermions.

The *spilling* method can reduce an ultracold fermionic system to a small number of atoms [26]. An illustration of the one-dimensional case is shown in Figure 2.2.

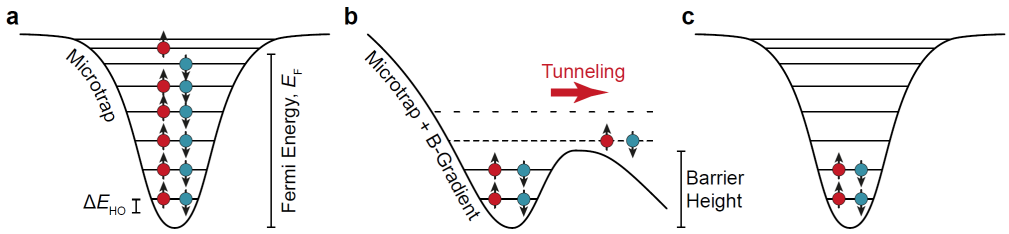

FIGURE 2.2: A FEW-BODY SYSTEM PREPARED WITH ATOM SPLILLING.
A: Fermionic atoms are trapped in a Micro Trap (MT), generated by a laser beam. Due to the Pauli exclusion principle, only two atoms with the opposite spin states are allowed per level.
B: Using a magnetic field gradient, a linear potential is added to the MT, which lowers the potential walls, and thus only a few states with low energy remain in the trap.
C: A few-body state with deterministic particle number has been prepared from many body-state. The illustration is taken from [27].

Consider atoms trapped in a harmonic trap cooled down to the ultracold regime. By applying a magnetic field gradient, the trap walls can be lowered such that higher energy atoms can escape the trap. The slope of this gradient can be increased up until only the lowest energy states remain in the trap. Due to the Pauli exclusion, only a few atoms occupy these states; thus, a few-body system has been prepared.

The fermionic behavior of ^{6}Li enables the simulation of diverse systems, such as few-body states. Additionally, their tunable interactions allow for the simulation of phase transitions like the BEC to BCS crossover. With these tools, ultracold ^{6}Li provides a qualified platform for flexible quantum simulation [28, 29]. The experimental preparation of deterministic atom samples, however, is not trivial. The following section will discuss how HQA prepares ultracold ^{6}Li atoms samples and how this process will be improved compared to current experiments in our group.

2.1 Overview of the Experiment

As discussed, ^{6}Li provides a promising platform for studying quantum systems. To deterministically prepare quantum systems, HQA uses an ultra-high vacuum chamber to isolate the atoms from their environment. This way, unwanted interactions with external particles are reduced to a minimum, and the lifetime of atomic samples is increased. To this end, a vacuum of roughly 2×10^{-11} mbar has been achieved in the HQA, which puts down the required groundwork for quantum simulations. Now, the main task is the preparation of atomic samples.

^{6}Li atoms need to be prepared in a controlled and repeatable way, such that large datasets can be recorded and the improved cycle time of HQA can be utilized (see Chapter 4). The purpose of HQA is to make this preparation as simplified and fast as possible. With the help of the currently running experiments in the group, HQA

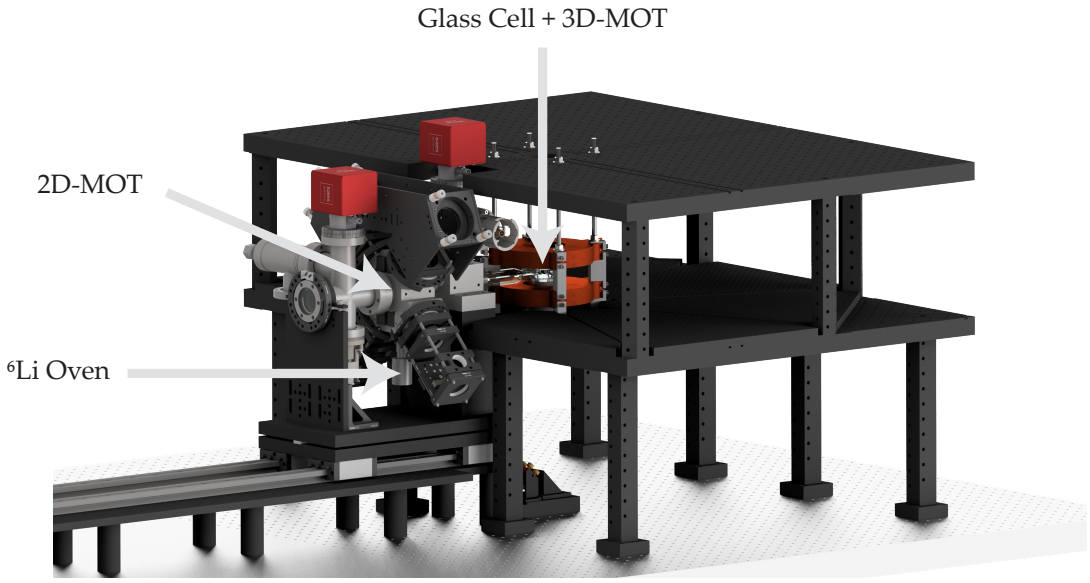

FIGURE 2.3: RENDERING OF THE HQA APPARATUS INCL. BREADBOARDS. The apparatus is mounted on two rails allowing a translation to the left side. The oven, the bowtie-shaped 2D-MOT, and the glass cell science chamber are marked by arrows. Two ion pumps (red) on top of the vacuum chamber maintain the vacuum pressure. Below the breadboards, the optical setup for the objective beams will be added soon (see Figure 5.1).

uses the available knowledge and applies what has been learned so far. This includes the move away from a Zeeman-Slower in the running setups towards a two-dimensional magneto-optical trap (2D-MOT) design.

Figure 2.3 shows a CAD render of the current experimental setup placed on the optical table. The vacuum assembly, including the glass cell, is attached to a rail system on a breadboard mounted to the table. With the rails and a ball bearing the entire apparatus can be translated to the side. In doing so, the glass cell slides through the magnetic field coils and exposes the center of the optical system. This gives direct access to the position between the coils, where optics and coils interact with trapped atoms. Therefore, this space is particularly useful. Moving the entire apparatus enables convenient measurements of the magnetic field and characterizations of the laser beams. In addition, the rail system is designed with a fixed end stop to return the experiment to the operational state. This will locate the apparatus at the same position as before, and quantum simulations can continue.

As shown in Figure 2.3, a small oven, where the ^{6}Li matter is stored, is attached to the bottom of the apparatus. It was filled with roughly 9 g ^{6}Li and 0.1 g ^{7}Li under a protective Argon atmosphere. This precaution prevented the excessive forming of Li_2O and LiOH, contaminating the vacuum. The amount of material in the oven should provide a reservoir of atoms lasting about a decade [30]. A heating wire is wrapped around the oven and connects to a Proportional-Integral-Differential (PID)

controller, which regulates the temperature of the reservoir. This way, the ^{6}Li inside will be heated to around 350 °C, where atoms will dissipate from the oven upwards into the 2D-MOT chamber. A single laser beam enters the vacuum chamber diagonally from the bottom. It is reflected in a bow tie configuration multiple times, such that the beam and its power are recycled. Therefore, an atom in 2D-MOT will experience four laser beams pointed at the center in a cross-like shape. Combined with an arrangement of adjustable permanent magnets around the laser crossing, a 2D-MOT for the lithium vapor is generated. This confinement allows the atoms to only move on a single horizontal axis, aligned to the clear line of sight towards the glass cell science chamber. The 2D-MOT (high vacuum) and the glass cell (ultra-high vacuum) are separated by a differential pumping stage.

As is visible in Figure 2.3, a 2D-MOT features a compact design, and compared to a bulgier Zeeman slower, it features a similar atom flux [31]. A Zeeman slower would also need a direct line of sight from the oven to the glass cell, resulting in more excess atom vapor in the glass cell. This could be solved by heating the viewport in the line of sight. However, this is not desired for the glass cell. A 2D-MOT, therefore, provides a vacuum, which will be less contaminated in the long run. In addition, by utilizing more powerful laser systems and larger beams, the loading rate of ^{6}Li atoms into a trap in the science chamber will be improved [30]. The 2D-MOT design is described in more detail in [30] and [32].

From the 2D-MOT, the atoms are transferred through the differential pumping stage. A laser beam, aligned to the horizontal axis, exerts a pushing force and effectively generates an atomic beam towards the glass cell center. In Figure 2.3, the glass cell is mounted between the magnetic coils to the right of the apparatus. The glass cell features seven side-facing 0.5" and two vertical 1.5" viewports. All viewports were manufactured with a special nanostructure coating on the in- and outside. This coating allows incident angles over 50° while holding reflectivities below 1%. These large angles without significant reflections enable the use of high *NA* optics (see Chapter 3). Further, the broadband characteristic of this coating allows a wide range of wavelengths to be used in the glass cell. The coating supports light from UV light at 200 nm up to IR light above 1.5 µm [30]. With these features, excellent optical access is granted to the atom samples. This access is essential since laser light is not merely the only measuring tool, revealing information about the atomic quantum state, but also a crucial part of trapping the atoms in the glass cell.

The atomic beam generated by the 2D-MOT passes the differential pumping stage right before it enters the glass cell. Here, the atoms are trapped in a 3D-MOT, which utilizes laser beams from all six spatial directions and a magnetic quadrupole field generated by four large copper coils. The 3D-MOT confines the atoms to a few millimeters wide cloud, reaching temperatures typically around 1 mK. This cloud is the starting point for the evaporation process, which cools the ^{6}Li gas to temperatures close to 1 nK.

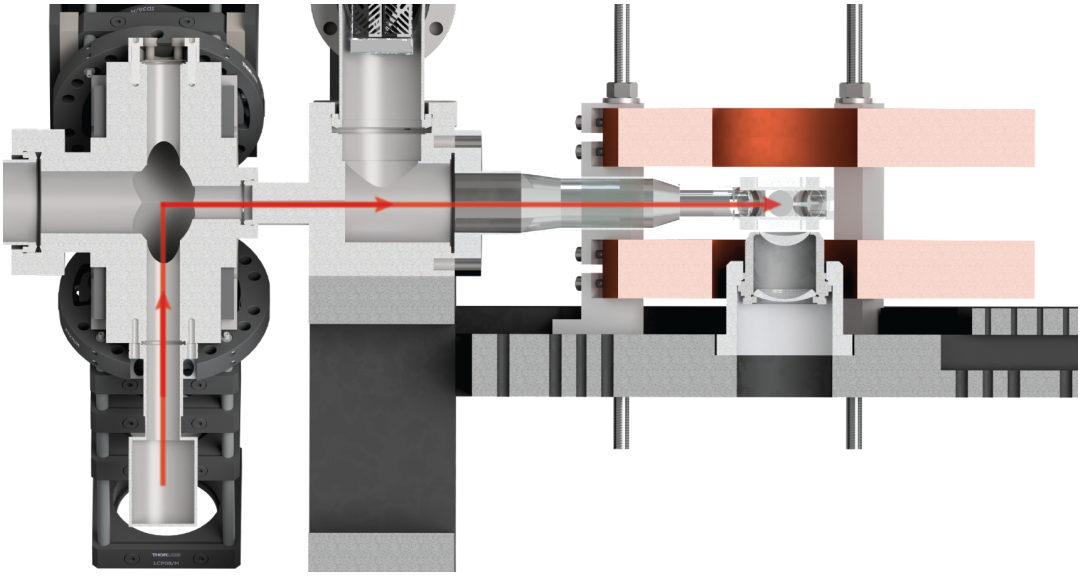

FIGURE 2.4: A CROSS-SECTION ALONG THE ATOM'S PATHWAY. The path of the ^{6}Li atoms is marked in red. The cross-section includes the oven, the 2D-MOT, the glass cell, the magnetic coils, and the objective with its mount on the breadboard. The atomic beam comes from the left through the narrow differential pumping stage and enters the glass cell. Note that the coil's wire management is not depicted.

Figure 2.4 shows a cross-section of the components around the glass cell. The atomic beam passes through the metal block, i.e., the differential pumping stage, on the right and enters the glass cell. The point of interest for quantum simulations is located at the center of the magnetic coil configuration. These coils are a magnetic field source for the 3D-MOT and a tuning instrument for the atomic interactions. This process utilizes the magnetic field dependency of interatomic scattering potentials, a Feshbach resonance. Both applications require different field parameters and different coil settings. Despite this, the identical coils can be used for both applications since both use cases are temporally separated. During the MOT loading, no Feshbach tuning is desired, and after the atoms are transferred into an optical dipole trap, where interactions need to be controlled, the 3D-MOT is no longer needed. So even though they take up a large portion of the valuable space around the glass cell, the magnetic coils are a versatile and essential part of the atom sample preparation.

2.2 Optics around the Science Chamber

As a fundamental component, the glass cell science chamber stands out as the heart of the apparatus. Here, atoms will be trapped by a 3D-MOT with laser beams entering from all six spatial directions and a magnetic field generated by the copper coils arranged in a Helmholtz configuration. For additional state preparation, an optical dipole trap and an evaporative cooling procedure will cool the atoms to ultracold temperatures. All these applications will require an optical interfacing with the atoms. Figure 2.4 shows the cross-section of the components around the glass cell to visualize the limited available space around the atoms.

The magnetic field coils will occupy the largest space due to their size necessary for the desired field strengths. As seen in Figure 2.4, the coil mounting was designed to be as compact and straightforward as possible. Four long threaded rods connect the coils to the lower and upper breadboard. The compact mounting brackets are made from Polyetheretherketone (PEEK) and fix the coil position. In Figure 2.4, such a bracket is visible behind the glass cell tube. The predesigned inserts between the coils fix the vertical coil separation. Each mounting bracket includes four adjustment screws to adjust the horizontal coil position. This solution takes up significantly less space than a larger mechanical flexure mount. Small magnetic blocks will be placed around the coils to fine-tune the magnetic field. Their additional magnetic moment will warp the magnetic field and allow an adjustment of field properties like the position of the magnetic saddle point. Once the best magnetic configuration for the coils is found, four nuts will secure the setup in position.

Not yet displayed in Figure 2.4 are the horizontal optical components like lenses, mirrors, or smaller microscope objectives. Extra care was put into planning the optical mounting so that the space around the small glass cell is used as efficiently as possible. Taking the experience from running experiments, HQA will explore a new mounting method, which will be discussed now.

2.2.1 Modular Approach

As a critical motive behind HQA, working with optical systems should be simple, modular, and flexible. Typically, an experiment uses one or two large optical breadboards to provide a baseplate for mounting any optical components. Multiple smaller setups like a digital micromirror device (DMD) trap [33] or an accordion lattice [34] are then assembled on the same baseplate. However, this is unpractical to easily replace and maintain partial optical setups. Often, much time is saved if one can take a complete setup out of the experiment, analyze it, and return it such that it performs like before. This also applies, for example, if an old box potential setup is no longer desired and should be replaced with a new optical lattice. In other circumstances, one might have to recharacterize a laser beam gone rogue.

Additionally, when an old setup is to be replaced, it can be removed without disassembling the entire experiment. A new setup can then be put in the same place.

This optical modularity allows the simultaneous development of new setups while the experiment is running. Therefore, construction periods are shortened, and the time during which measurements are paused is reduced. For these and more reasons to be discussed, we designed a modular structure, which takes the flexibility of optical breadboards and combines it with a modular approach.

Octagonal Breadboard

Optical breadboards are solid platforms, often made from robust materials like aluminum or stainless steel. They provide an excellent baseplate for assembling optical setups, positioning components, or mounting other smaller breadboards. Generally, they offer a grid of threaded screw-holes, which can be used for mounting components and positional referencing. A laser beam can, for example, be aligned such that it always runs above a row of screw-holes. Optical components must then sit on the underlying screw-hole geometry to be aligned appropriately.

For the mounting around the glass cell, HQA will hold onto the breadboard platform. As shown in Figure 2.5, a solid 30 mm thick eloxated aluminum breadboard will provide a stable base for all optical components. To adjust to the experiment geometry, however, some adjustments are made to the classic breadboard design. While the screw-hole grid is still desirable as a mounting and referencing tool, the breadboard geometry should match the octagonal glass cell. The screw-hole pattern, therefore, consists of seven sections, each aligned to one of the small 0.5 ″ viewports. This pattern is shown in Figure 2.5, where the radial symmetry toward the glass cell can be seen. An additional eighth section is located beneath the glass cell for diagnosis when the apparatus is moved to the side. Since most parts in the proximity of the coils are made from metal, one must consider electric currents induced by the temporally changing magnetic fields. These currents are called *Eddy currents* and can disturb the magnetic field on the atoms [35]. A glass cell is already beneficial instead of a metal chamber between the coils. In addition, the breadboard has been cut below the glass cell, which gives a breakpoint in the aluminum to weaken induced magnetic fields around the glass cell.

Additionally, the breadboard features an approach to increase optical modularity. Seven smaller "slide-in" breadboards will be mounted on each section allowing exchangeable modules for each viewport axis. Rail-like grooves on the main breadboard and end stops right before the center point provide a guiding structure for their positioning. Multiple holes for precision fitting pins further lock the modules in place. These tools ensure a nearly identical placement after taking a module and putting it back in. They even allow the interchangeability of the triangular-shaped modules. These optical modules bring a variety of advantages to the experiment, which will be discussed now.

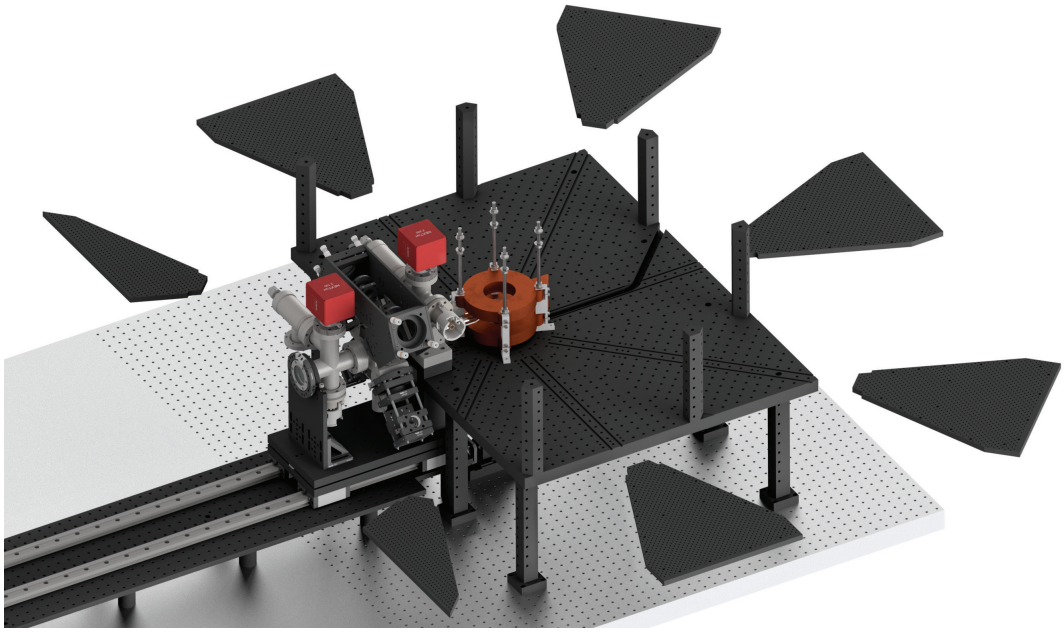

FIGURE 2.5: HQA RENDERING WITH BREADBOARD AND MODULES. The optical breadboard is custom-built from aluminum and is mounted eight feet on the optical table in the lab. The optical modules are octagonally distributed around the magnetic field coils and the glass cell chamber. Above the modules, a second breadboard will be mounted, allowing access to the upper vertical glass cell viewport.

Optical Modules

Three essential concepts inspire the design of the optical breadboard modules. First, it allows the manufacturing of a module to specific needs. For instance, over time, HQA might switch from the classic breadboard M6 screw-holes with a 25 mm spacing to smaller holes and tighter grid spacing. This is easily achievable since both types of breadboards are compatible with the system. Further, one can design a module with pre-machined positions for optics such as lenses or acousto-optical modulators (AOMs). Such modules reduce the assembling time of optical setups and increase the alignment confidence, which has proven convenient, especially in day-to-day use [36]. At the core of this concept ultimately lies the reduction of the degrees of freedom to a bare minimum. This way, trust in the alignment of optics is increased, and more time can be spent on the interesting physical problems instead of the technicalities. In other words, this concept improves the quality of life in the lab by simplifying optics.

Second, reliably removing and reinserting modules in the experiment opens a wide range of characterization possibilities. Before installing a module into the experiment, one can mount it on a test bench, which resembles a copy of the actual breadboard. It features an identical precise positioning design, i.e., the guiding grooves and fitting pins. Consequently, the emulated position of the atom sample can be designated on this test bench. This allows a comprehensive characterization

of the laser light hitting the atoms. Analysis devices like a Beam Profiler or a Shack-Hartmann wavefront sensor can give great insights into the laser beam characteristics, e.g., for beam collimation or aberration correction [37]. With custom-designed mounts, these devices can be positioned directly at the designated atom position. The optical module can then be optimized for the best performance. When the module finally enters the experiment, no extra setup should be necessary except for fine alignment.

Third, the desired task of an optical setup might change in the future, and new requirements for optical performance might arise. The modules provide flexibility, which cannot be found in a traditional setup on a single large breadboard. Thanks to the characterization possibilities, the precise fitting pins, and the slide-in grooves, the module breadboards can be easily mounted on the breadboard. Moreover, when all the above works as intended, optical modules can be freely exchanged between all glass cell viewports, apart from two exceptions. Both sections on the breadboard side facing the vacuum chamber are mechanically limited to a smaller size. Hence, they are only interchangeable by turning them upside down. This modularity will nonetheless simplify the work with optics in the lab.

Furthermore, the entire modular concept allows practical cooperation between similar experiments. Provided the mounting design is implemented similarly, entire setups can be shared. For example, consider an assembly that generates an optical potential with a DMD. If the setup works as designed and has been used successfully in one experiment, the conceptual drawing or the CAD design can easily be shared with another. Even the original module could be wrapped and sent as a Christmas gift to a collaborating group.

Objective Mount

At the heart of the optical arrangement around the glass cell lies the microscope objective (see below the glass cell in Figure 2.4). It will be used for the imaging and trapping of atomic samples. Thus, it serves as the static reference point for all other optical components, especially the optical modules. HQA aims to increase the confidence in the alignment and the long-term stability of the objective. Therefore, a passive objective mount was designed. To reduce magnetically induced Eddy currents, it is made from PEEK. It features a positional referencing shoulder compatible with the objective design discussed in Chapter 3. Mounted directly in the large breadboard, the mount will enable the objective as a stable optical reference for other mounted optical components. All mechanical dimensions of the mount and the breadboard are predetermined. Thus, they can be custom-manufactured, preferably with tolerances of roughly 10 µm, and the optical modules can be designed with the precise position of the objective in mind.

This approach, however, can only be achieved if the optical and mechanical properties of the objective match the specifications. Hence, in-depth characterization is necessary.

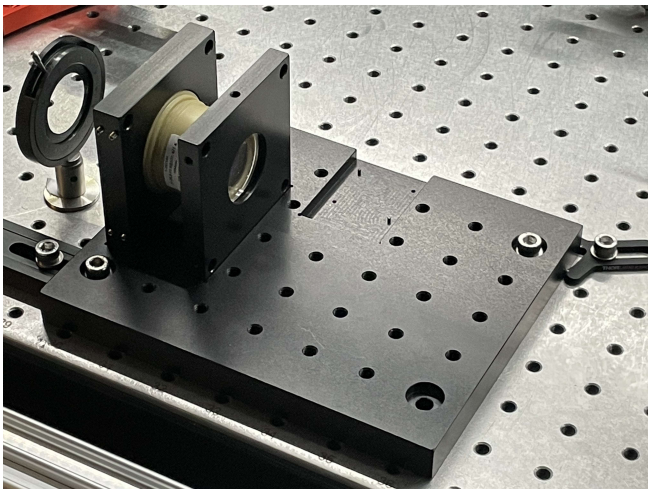

FIGURE 2.6: PICTURE OF THE CHARACTERIZATION TEST BENCH
The objective is mounted in a separate plate, which fits into an inlet on the board, fixing the plate position. The same applies to the second plate holding a copy of the glass cell viewport. For details on the design and the dimensions, see Appendix A.1.

2.2.2 Characterization Test Bench

The first iteration of a test bench was designed to characterize the most crucial optical component in HQA. As discussed in Chapter 3, the main microscope objective plays a crucial role in manipulating and studying quantum states. Thorough characterization and repeatable measurements are required to ensure trust in its specified properties over time. The previously described mounting concept can be realized only if its optical and mechanical properties are well studied.

To both characterize this objective and collect experience in designing a custom test bench, the small breadboard in Figure 2.6 was designed. Four M6 screws mount the breadboard onto an optical table in the lab. Additionally, the design features predefined inlets for two mounting plates holding the objective and a glass window resembling the vertical viewports of the glass cell. For a microscope objective, the alignment is particularly sensitive (see Chapter 3). Fixing its position and rotation to the optical table ensures confidence in the alignment to other optical components. Compared to setups where every component needs to be mounted in free space, the advantages of a reduced parameter space, i.e., having fewer degrees of freedom, were immediately observed. The mounted objective is directly aligned to the hole pattern on the optical table, and its optical axis lies at 50 mm beam height. The following chapter will discuss how the characterization test bench will be used with the objective in a meaningful way for HQA.

3 High-Resolution Imaging and Characterization

As discussed in the previous chapters, the HQA will study various ensembles of ^{6}Li atoms in the HQA. Some of these will be few-particle systems trapped in a tight tweezer or more advanced systems like double-well potentials and 2D lattices. How the atoms in these microscopic systems behave and interact with each other is especially interesting for understanding emerging quantum phenomena.

To gain as much insight into the behavior of the quantum state in these systems as possible, extra focus should be put on the imaging of single atoms. To image such small particles, the optical setup needs to be capable of producing highly detailed images. For this task, a high-performance microscope objective has proven necessary [38]. Unfortunately, with a size below one nanometer, an atom is smaller than the optical resolution of such an objective. Still, using fluorescence imaging, enough photons can be collected from a single atom such that an intensity distribution of a few micrometers can be recorded on a camera.

However, achieving such a performance is not trivial. Not only is a well-thought-out design for the objective important, but the confirmation of its designed capabilities by an experimental characterization as well. This chapter describes designing and testing the high-resolution optics for the HQA in three parts. First, the single atom imaging scheme in our current experiments will be described. Then, the requirements and design decisions for the microscope objective are introduced. The last section then discusses ways to characterize this objective and presents the results of these tests.

3.1 Single Atom Imaging

Ultracold ^{6}Li atoms in the ground state emit no light, which a camera could capture. Thus, our running experiments detect single atoms with fluorescence imaging. For this, pulsed laser light resonant to the σ_- transition excites the trapped atoms into a higher energy state. The excited atoms spontaneously decay into the ground state and emit fluorescence photons. A microscope objective is placed close to the atoms to record an atom image, and a camera detects their signal with few-photon sensitivity. Previous work has shown that using a low-noise camera, like an *electron-multiplying charge-coupled device* (EMCCD), requires an average number of

20 detected photons per atom to produce a signal above the noise level [39]. However, collecting more photons per atom provides many advantages, such as using other camera types. For example, a *scientific complementary metal-oxide-semiconductor* (sCMOS) camera features a lower quantum efficiency but does not require on-chip gain and hence does not suffer from gain noise. Therefore, it allows a more precise measurement of the photon number than an EMCCD, where a large gain produces a large intensity distribution. An sCMOS can make comprehensive measurements of fluorescence intensities possible. Therefore, optimizing the system to collect as many scattered photons as possible makes sense.

The simplest way is an increase in exposure time, which is currently in the regime of $T = 15\,\mu s$ [27]. This exposure time, however, leads to a degraded atom signal on the camera. The atoms are exposed to the pulsed imaging laser during the exposure time. When an atom absorbs a photon from the resonant laser pulses and spontaneously emits a fluorescence photon, it also experiences a kick by the scattered photon. The direction of this kick depends on the radiation pattern of the spontaneously decaying photons. For the decay transition, it takes the form of the dipole radiation pattern

$$\frac{I(\theta)}{I_0} = \frac{3}{8\pi}\frac{(1+\cos^2(\theta))}{2}, \tag{3.1}$$

with the angle to the dipole axis θ and a normalization factor $\frac{3}{8\pi}$ such that the integral over the entire solid angle is unity [39]. The collected fraction of scattered photons S is then the integral

$$S = \int_0^{\theta}\int_0^{2\pi}\frac{I(\theta)}{I_0}\sin\theta d\theta d\phi = \frac{1}{8}(4 - 3\cos(\theta) - \cos^3(\theta)). \tag{3.2}$$

The alignment of this pattern depends on the direction of the magnetic field around the atoms. In HQA, the dipole axis corresponds to the vertical axis, which leads to a uniformly horizontal distribution of scattered photons.

Hence, multiple scattering events lead to a random horizontal motion of the atom, described by the Brownian motion. A longer exposure time will therefore increase the area from which photons are emitted during flashing. During imaging, this motion increases the spatial distribution of the atoms on the camera, and the image of an atom will be blurred. To mitigate this, one could, for example, pin the atoms during the imaging procedure with an optical dipole trap. While this would prevent the Brownian motion, it is not always desirable. For instance, scenarios such as momentum space mapping require the atoms to move freely during imaging. Consequently, the exposure time is kept small, and the optical system is improved to capture more photons.

As described in Equation 3.1, the scattering of fluorescence photons follows a dipole

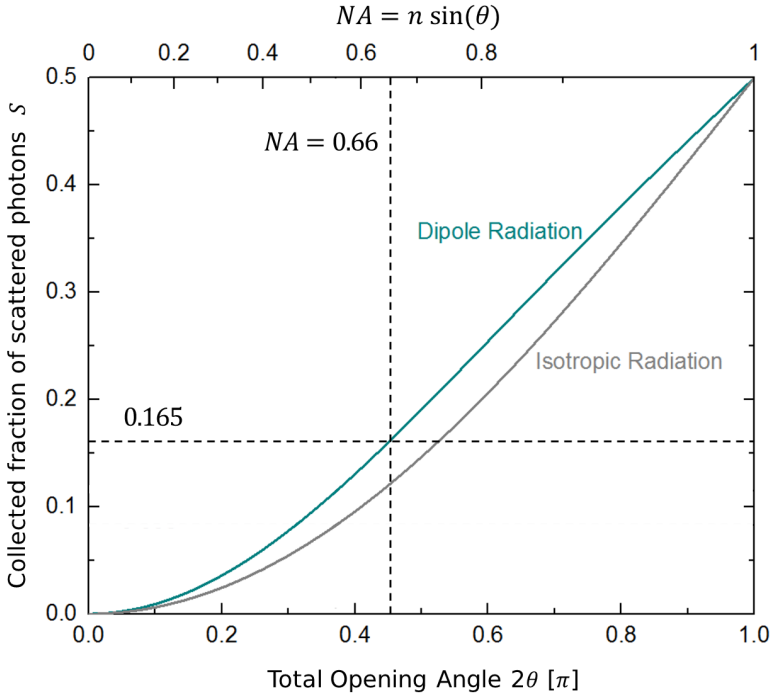

FIGURE 3.1: FRACTION OF COLLECTED PHOTONS DEPENDING ON NA. For the HQA objective's $NA = 0.66$, the optimal fraction of collected fluorescence photons amounts to 0.165. Losses like the camera quantum efficiency are not accounted for yet. Adapted from [39].

radiation pattern with enhanced intensity in the vertical direction. Therefore, mounting the microscope objective on this vertical axis already leads to a more significant fraction of collected photons than mounting it on the horizontal axis. However, since every photon improves the single-atom detection fidelity and reduces exposure times, a larger captured solid angle of the dipole radiation pattern is beneficial. A microscope objective can achieve this with a large collecting angle. This angle can also be described by the *numerical aperture NA*, which is defined by

$$NA = n \sin(\theta), \tag{3.3}$$

with the refractive index n of the medium, in which the photons travel towards the objective ($n = 1$ for air) and θ, the semi-angle of light that can enter the objective.

Figure 3.1 shows the collected fraction of scattered photons depending on the numerical aperture of the microscope objective. The actual number of detected photons will be smaller than this theoretical prediction. This is because the optical elements and the CCD camera will introduce some losses. For example, consider the numbers from previous work with an $NA = 0.55$ objective [38]. Here, an optical path transmission of 90% and a camera quantum efficiency of $\eta = 0.85$ lead to a fraction of collected photons of around 9%. However, an enhanced NA of the HQA objective improves this predicted fraction to around 13%.

A well-designed microscope objective consequently improves the ability to resolve single atoms. A higher NA increases the number of collected photons, enabling a shorter exposure time t. Therefore, the Brownian motion will be reduced, leading to a smaller atomic signal spread on the camera. The width of this spread on the camera is given by

$$\sigma(t) = \sqrt{\frac{R\alpha}{3}} v_{\mathrm{rec}} t^{3/2}, \tag{3.4}$$

including the scattering rate R, the recoil velocity v_{rec}, and a dipole emission correction factor α [38]. The proportionality $\sigma(t) \propto t^{3/2}$ shows that a smaller spread can be achieved with a smaller exposure time. Thus, a shorter exposure time improves the single atom resolution of the recorded images in each experimental cycle.

As the experiment's fundamental optical component, the objective will provide the imaging capabilities required for a detailed analysis of the prepared quantum states. Its optical performance will determine the quality of tight optical dipole traps and recorded atom images. A high numerical aperture will benefit single-atom detection and optical resolution, which will be discussed in Section 3.3.1. Therefore, much care should be put into designing and balancing required parameters with external restrictions. It will be discussed now how this was done for HQA.

3.2 Objective Design

Using the results from the previous section and optimizing the design parameters, a custom microscope objective (see Figure 3.2) was developed in cooperation with the company *Special Optics* [40]. As concluded in the previous section, HQA requires an objective with the highest numerical aperture possible while adhering to external restrictions. Now, the specific properties of a common microscope objective will be introduced. Additionally, it will be discussed how these are balanced with the requirements.

A lens's effective *focal length* f determines the convergence or divergence gained by light rays passing the optical assembly. For incoming light rays parallel to the optical axis, a negative focal length indicates diverging rays, while a positive one specifies converging light. Another way to characterize the divergence of light is the curvature of the *wavefront*. The wavefront of a light beam is the surface, where components of the light field have a constant phase. If a lens transforms a collimated beam with a negative focal length, the output beam is diverging. The off-axis phase is then delayed, and the wavefront becomes spherical with a radius $R > 0$. On the other hand, a lens with a positive focal length creates a converging beam with a wavefront radius $R < 0$.

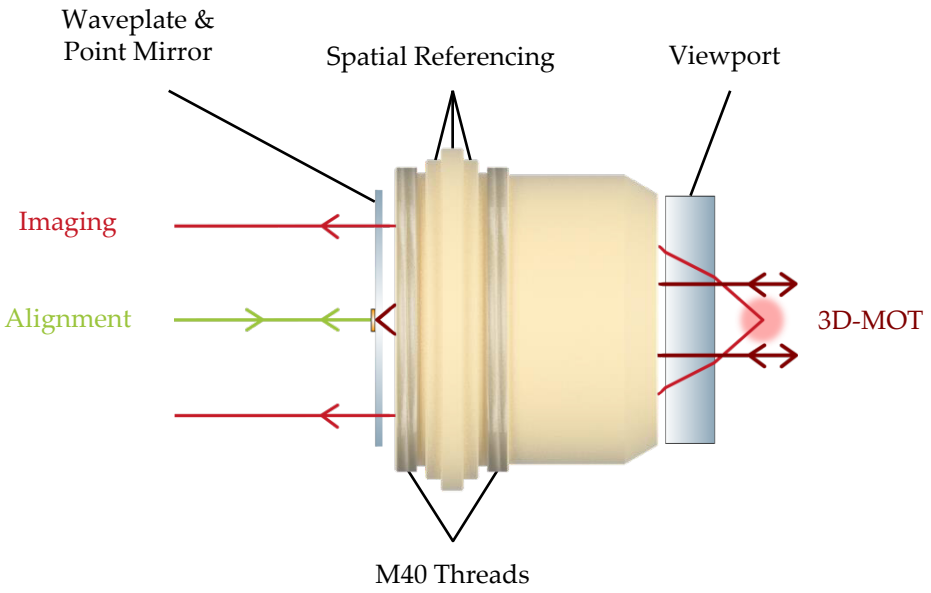

FIGURE 3.2: DRAWING OF THE OBJECTIVE WITH ITS APPLICATIONS. On paper, the objective is depicted on a 1:1 scale. A $\lambda/4$ waveplate with a small mirror in the center is drawn to the left. The rectangular shape on the right depicts the vacuum viewport of the glass cell.

Microscope objectives collect light from a small sample; thus, the focal length needs to be positive. The light rays are on a converging path, as seen from the objective. The maximum angle of these rays increases with a smaller focal length (keeping a constant lens diameter). This means that high-NA microscope objectives typically have smaller focal lengths than, for instance, objectives used in landscape photography, where light rays from far away enter the objective with a shallow angle. For the HQA objective, the designed focal length is $f_{\text{objective}} = 18.8\,\text{mm}$.

The *aperture stop* D of a lens or an objective is the smallest opening through which light can pass. For HQA, the aperture is given by the objective size and is mechanically limited by the viewport diameter and the magnetic field coils around the glass cell. Additionally, the general optics should be small to avoid bulky optics as much as possible. In a compromise with all other required features, the aperture stop of the custom objective settled at $D = 24.8\,\text{mm}$.

Further, the aperture also determines a maximum angle for collected rays, which is visible in the approximation of the numerical aperture via

$$NA = n \sin(\theta) \approx \frac{D}{2f} . \tag{3.5}$$

With this estimation, the numerical aperture is $NA = 0.66$. In the development process, we also explored other possible objective designs with a larger numerical

aperture, e.g., $NA = 0.8$. While this would improve the optical resolution and the single atom imaging capabilities, it would have ruled out other essential features like the external back focal plane, which will be discussed later.

Alternatively, one can simulate the geometric ray propagation with a ray-tracing program like *Zemax*. The maximum angle θ at which rays can pass the objective unhindered yields the numerical aperture. Analyzing the *Zemax* file provided by the manufacturing company gives a maximum semi-angle of $\theta = 41.1°$, confirming the numerical aperture from above.

Nowadays, microscope objectives are mostly *infinity corrected*. These objectives transform light from an observed sample in the focal plane into a collimated parallel beam, which allows for high flexibility and interchangeability of optical elements after the objective. For example, a straightforward imaging setup including an infinity-corrected objective would add another focusing lens, which transforms the collimated beam from the objective into a focused image. This image could then be recorded with a camera sensor.

The *magnification* M of such an imaging setup depends on the focal lengths of both lenses and describes the ratio of the image size x_{image} and the sample size x_{sample}. It is given by

$$M = \frac{x_{\text{image}}}{x_{\text{sample}}} = \frac{f_{\text{achr}}}{f_{\text{objective}}}, \tag{3.6}$$

with the focusing lens f_{achr} and the microscope objective $f_{\text{objective}}$. The magnification can be tuned with the focusing lens for a given objective focal length.

For multiple reasons, the magnification of the high-NA optics in the HQA will be roughly $M = 20$. On the one hand, for single atom imaging, the current experiments use a magnification of up to 8. This provides an atom signal above the camera noise. In contrast, however, HQA's higher NA provides more captured photons per atom, which allows for a larger magnification of the atom image since the required photons per camera pixel stay the same. On the other hand, geometric restrictions by other optics on the optical table will limit the focal length of the second lens.

The *working distance WD* specifies the normal distance from the final objective lens surface to the focal plane. While a single thin lens has a working distance roughly the same as the focal length, this changes for compound lens systems. An example of a compound lens is a microscope objective, which consists of multiple lens elements to achieve a performance with few optical errors while keeping a compact form factor. The effective focal length of the combined lenses, which determines the magnification of the objective, is rarely equal to the distance between the last lens and the focal plane. Therefore, for a compound lens, the working distance differs from the effective focal length.

Microscope objectives with a large numerical aperture generally have a working distance in the regime of a few millimeters, which allows the collection of rays with

large angles while keeping the lens diameters reasonably small. In addition, some microscopes achieve large *NA*s by increasing the refractive index of the medium before the objective, for example, with oil immersion. Atoms in the vacuum are separated from the environment by the glass cell viewports, which limit the working distance of the optics around the glass cell. Combining the distance from the center of the glass cell to the viewport, the viewport thickness, and a tolerance gap of 1 mm between the viewport and the objective, the working distance becomes $WD = 6.35\,\text{mm} + 6.35\,\text{mm} + 1\,\text{mm} = 13.7\,\text{mm}$.

The *back focal plane* is defined by the point at which the rays converge, which enter the objective parallel to the optical axis from the atom side. In other words, if one sends a collimated beam through the back side of the objective, this light will be focused to a point in the back focal plane. This plane lies in the objective assembly itself for many microscope objectives, making it inaccessible. Collimated light from the front side will be scattered and absorbed inside the objective or exits the objective highly divergent.

For this objective design, an effort was made to shift the external focal plane outside the objective housing. This feature makes it possible to obtain direct access to the Fourier plane, enabling the Fourier filtering of specific frequency modes of the light field. The details of this method are discussed in Section 3.3.2.

Additionally, the external back focus allows the mounting of a reflecting mirror in this back focal plane. This mirror is visible on the left of Figure 3.2, where a $\lambda/4$ waveplate with a sputtered point-like mirror is placed in the back focal plane. This mirror will be able to retroreflect collimated light - in the figure from the right side - back into itself. With a diameter of 1 mm, the mirror will only cover 0.16 % of the aperture area and, therefore, will not diminish the imaging performance significantly.

This mirror can be utilized for different applications. One primary purpose is the retroreflection of a collimated 3D-MOT beam. Since the objective is mounted from the bottom, it sits directly on the axis of the vertical 3D-MOT beam, which enters the objective from the atom side. Due to its collimation, the beam converges to a point in the objective back focal plane. For complete three-dimensional trapping, however, the 3D-MOT also needs a collimated beam from the bottom. Due to the high *NA*, such a beam would have to enter the objective, highly diverging from its point of origin in the back focal plane. A light source at this point would require an overly complicated optical setup, like mounting a laser fiber tip vertically beneath the objective. The point-like mirror is used as an alternative to retroreflect the beam from the top. The waveplate adjusts the polarization such that the 3D-MOT beams have the correct circular polarization. Other applications for the point-like mirror are, e.g., an alignment beam for the optics behind the objective or the reflection of a lattice beam, where a laser beam interferes with its reflection and generates a lattice pattern on the atoms.

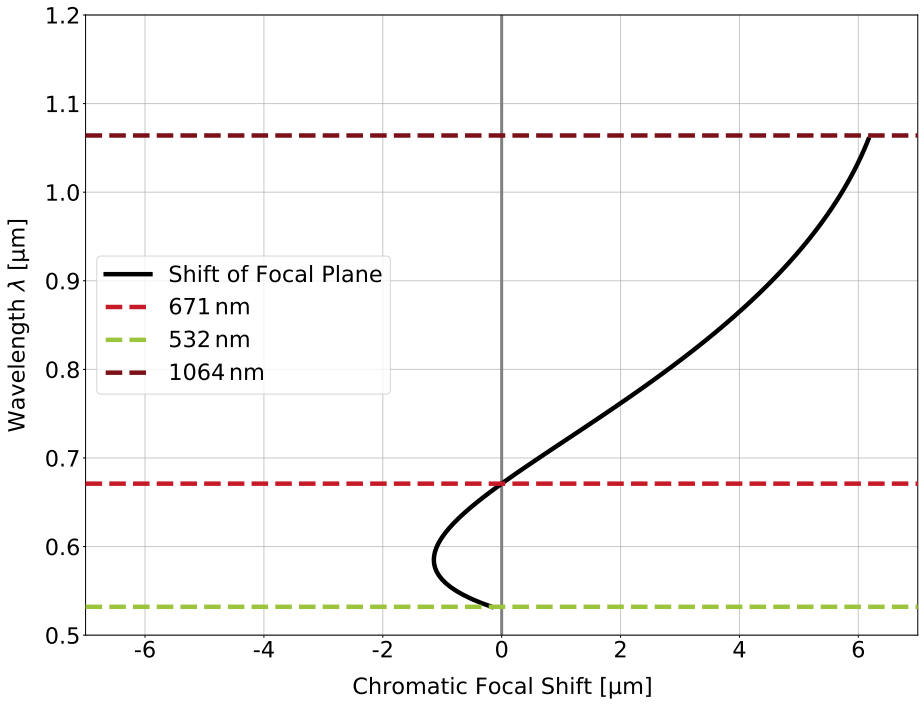

FIGURE 3.3: *Zemax* SIMULATED CHROMATIC SHIFT OF THE FOCAL PLANE ALONG THE OPTICAL AXIS.
The data stems from the center of the field of view and covers our experiments' three most used wavelengths, marked by the horizontal dashed lines.

The *chromatic focal shift* describes the change of focal length and working distance depending on the wavelength. Lenses often have different properties for different wavelengths since effects like refraction change with the wavelength. Light with different wavelengths then propagates on different paths through a lens. A simple spherical lens then introduces chromatic aberrations like a different focal plane for each wavelength. Using multiple lenses with changing refractive index in series allows a correction of this chromatic error. The *Special Optics* objective features an *apochromatic* lens [41], which allows the correction of the chromatic focal plane shift for the three most used wavelengths in our experiments. The simulated optimized chromatic shift is displayed in Figure 3.3. Light with $\lambda = 671\,\text{nm}$ will be used for imaging, where the position of the focal plane is crucial. However, the slight deviation in the range of a few µm for light with $\lambda > 671\,\text{nm}$ might be relevant for optical dipole traps. Their focal plane position can be compensated to some extent with a small input beam convergence of 0.4 mrad. This angle was determined by the Zemax simulation. This broadband optimization enables the objective for multiple applications simultaneously. For example, the recording of a fluorescence image

might use $\lambda = 671\,\text{nm}$ light, while at the same time, a blue- or red-detuned trap with 532 nm or 1064 nm respectively is engaged. The small chromatic focal shift enables the imaging of these different wavelengths onto the same atom plane.

The smallest possible *waist* ω of a focused beam is crucial for very tight tweezer traps. The diameter of a focused tweezer beam determines the required power for a certain trap depth, given by the laser intensity. The intensity is given in units $[\text{W}/\text{m}^2]$. The smaller the beam, the less laser power is needed to achieve the same intensity in the trap area. The diameter of a Gaussian beam is twice the beam waist and is given by the wavelength λ, the focal length $f_{\text{objective}}$, and the aperture D [42]. For such a beam focused down by the objective, the smallest achievable diameters are

$$2\omega_0 = \frac{4}{\pi}\lambda\frac{f_{\text{objective}}}{D} = \begin{cases} 0.51\,\mu\text{m} & \text{for } \lambda = 532\,\text{nm} \\ 0.65\,\mu\text{m} & \text{for } \lambda = 671\,\text{nm} \\ 1.02\,\mu\text{m} & \text{for } \lambda = 1064\,\text{nm} \end{cases}, \tag{3.7}$$

with the values for the most used wavelengths in our experiments.

The *Rayleigh Range* z_R is the distance along the optical axis for which the waist ω is smaller than $\sqrt{2}\omega_0$ [42]. It is given by

$$2z_R = \frac{2\pi\omega_0^2}{\lambda} = \begin{cases} 0.77\,\mu\text{m} & \text{for } \lambda = 532\,\text{nm} \\ 0.98\,\mu\text{m} & \text{for } \lambda = 671\,\text{nm} \\ 1.55\,\mu\text{m} & \text{for } \lambda = 1064\,\text{nm} \end{cases}, \tag{3.8}$$

for a maximally focused beam with the minimal waist ω_0. A beam with a smaller minimal waist could be used if a larger Rayleigh Range is desired. With Equation 3.7 such a beam can be achieved by utilizing a smaller input aperture D. Additionally, the Rayleigh Range can be used as a tolerance for the axial positioning of components in the focus of a Gaussian beam.

3.3 Objective Characterization

So far, this thesis has discussed the properties and the conceptual design of the microscope objective. This section will now examine the real-world performance of the objective, both in a theoretical and experimental approach.

First, the most common evaluation criteria will be introduced to assess the optical performance. Then, a simulation will provide more details on the light propagation through the objective and an expectation value for the achievable resolution.

Finally, the last sections will discuss the experimental implementation of the objective characterization. The main focus will be probing the field of view using a sub-resolution nanopore device.

Many ways to characterize optics present themselves with the wide range of optical tools available today. From simple transmission measurements to expensive laser interferometers, measurements with varying complexity are possible. This thesis investigates the properties essential for planning and manufacturing the mounting structure around the glass cell, and properties that will most likely play a significant role during experimental runs. For instance, this includes the best angle at which the objective should be operated or the imaging of small features like single atoms.

While this will give a good insight into the objective's performance, it should be mentioned that other ways to characterize the objective might be interesting in the future. One example is the characterization of a tight tweezer beam produced by the objective. However, a lens with a better resolution and, therefore, higher numerical aperture than the examined one would be required to resolve such a small beam. For example, a microscope objective with a small working distance and a NA of 0.8 would accomplish this task. Since the HQA features a rail-mounted chamber and allows access to the atom plane, this characterization could even be performed with the objective mounted in the experiment.

As explained in Chapter 2, the in-depth characterization of the objective is essential for the passively mounted referencing structure and the concept of interchangeable modules. The focus point of the microscope objective determines the best performing location for tight tweezer trap beams and high-resolution imaging, so it acts as the center point of the optical coordinate system. All other optics interfacing with the atoms, for example, from the side, will be aligned to this focus.

Since one wants to interchange and pre-characterize the optical modules around the glass cell, this point needs to be as stable as possible. For that reason, a simple objective mount was designed with no degrees of freedom, mounting the objective passively in the experiment. This passive mount requires precise knowledge about the optical properties of the objective. If, for example, the lenses are not perfectly aligned in the objective mechanical housing such that transmitted light acquires an

unexpected angle, this should be considered during the planning and manufacturing of the mount. Only then the objective focus can be trusted as a stable reference point.

The following section identifies the parameters describing the objective's performance. It would be beneficial if these parameters could be simulated beforehand to contextualize the experimental data. These simulations will use a self-scripted algorithm and the commonly used optical design software *Zemax OpticStudio*.

3.3.1 Optical Performance Parameters

In this section, the lens performance discussion will lay the groundwork for the experimental analysis. Then, it will be discussed how the resolution can be a figure of merit for the objective's performance. Finally, a Fourier simulation of light propagation will help to understand the point emitter characterization test, discussed afterward.

Diffraction-Limited Performance

The optical systems in quantum simulators play a crucial role, and their optical components must be of high quality to provide the best performance possible. This ensures, for example, the smallest possible double-well separations, the tightest tweezer traps, or the highest image resolution. Such a performance requires optical components that imprint as few errors as possible onto the light wavefronts. For this, the imperfections in the lenses, mirrors, and similar optics need to be minimized. Thus, one should choose components that are manufactured with high precision. However, aberrations in optical systems depend on the quality of optical components and can also stem from misaligned optics. One example of that is the vacuum window in front of the objective. A slight tilt of 1 mrad here already decreases the optical performance of the objective notably. Generally, a system is desired, not limited by imperfect optics but rather by the unavoidable physical effects of diffraction. Hence, the term *diffraction-limited* is widely used to describe a system as good as physics allows it to be.

To define diffraction-limited performance, the following section examines light wavefronts and their deformations, also called *aberrations*. An ideal wavefront is described by a perfect plane or a spherical shape. Consider the deviation from an ideal wavefront in units of the wavelength λ, i.e., the wavefront error W. The largest difference then defines the peak-to-valley (PV) deviation W_{PV}. This value describes the maximal wavefront distortion and is an example of a measure of optical performance. However, the PV deviation is susceptible to single points of wavefront errors. A less conservative approach is usually more reasonable. The Root-Mean-Square (RMS) deviation W_{RMS} describes the mean quadratic deviation from the perfect spherical wavefront

$$W_{\mathrm{RMS}} = \sqrt{\langle W^2 \rangle - \langle W \rangle^2}, \tag{3.9}$$

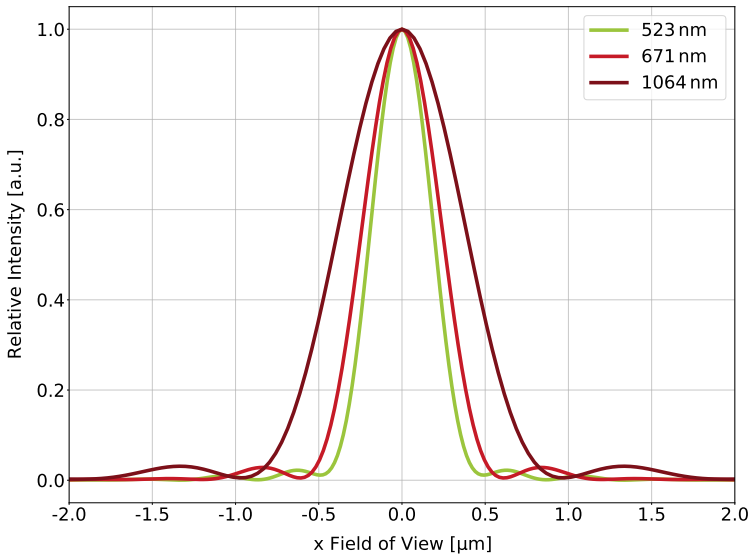

FIGURE 3.4: ZEMAX SIMULATION OF THE DIFFRACTION-LIMITED PSF. In the simulation, an ideal plane wavefront enters the objective parallel to the optical axis and is focused on the focal point. The displayed data stems from the center of the focal plane and covers our experiments' three most used wavelengths.

and yields such a balanced approach, which is not as strongly affected by a single error compared to W_{PV}. The RMS error thus provides a more robust measure for the overall image quality.

Besides the wavefront error, another figure of merit for optical performance is the *Point Spread Function* (PSF). As a visualization, consider the simulated PSF for the microscope objective in Figure 3.4. If a lens transforms a plane wavefront into a converging spherical wave, the converging rays will merge in the focal point. Since every lens has a finite size, one inevitably encounters diffraction effects at the lens aperture. Thus, the intensity distribution at the focal point, the PSF, is not perfectly sharp. Any lens imperfections imprinted on the converging wavefront will result in a smeared-out converging point and, therefore, an aberrated PSF, deforming its shape and decreasing the central peak intensity. To quantify this, one can use the *Strehl Ratio* D_S, defined as the ratio between the aberrated and the ideal PSF peak intensity.

To finally determine whether an optical system is diffraction-limited, one needs a criterion to quantify the wavefront aberrations introduced by imperfections in the optical system. Table 3.1 presents an overview of the most commonly used performance criteria. Experience in this field has shown that these criteria give a reliable measure for wavefront aberrations and their influence on image quality.

TABLE 3.1: OVERVIEW OF COMMON PERFORMANCE CRITERIA FOR MONOCHROMATIC LIGHT [43, 44]

Diffraction-Limited Imaging		
Criterion	Definition	Notes
RMS (Maréchal)	$W_{\mathrm{RMS}} < \lambda/14$	Most valuable for the overall performance
PV (Rayleigh)	$W_{\mathrm{PV}} < \lambda/4$	Sensitive, also depends on aberration type
Strehl Ratio	$D_S > 0.8$	Difficult to measure
Spatial Resolution Limits (Separation of two Point Sources)		
Limit	Definition	Notes
Rayleigh	$r_R = 0.61\,\lambda/NA$	PSF_1 maximum lies on PSF_2 minimum
Sparrow	$r_S = 0.47\,\lambda/NA$	The summed intensity becomes flat

Resolution

Since an essential purpose of the high-*NA* objective is to image single atoms, this chapter prioritizes the ability to resolve small details, i.e., the *resolution*. The resolution of any optical system's objective is defined by the distance r at which two points, imaged by the objective, can still be distinguished as single components. While talking about optical resolutions, a smaller distance r is often related to a "higher" or "increased" resolution, though the meaning is quite evident in the context.

To determine the distance r, consider the image of two overlapping point sources. The PSF distribution gives the image of a single point source, and the overlap of two such distributions is then given by the summed intensity of two PSF distributions. The *Rayleigh Limit* commonly describes the minimal overlap at which the two PSFs in this sum can still be extinguished. However, other definitions like the *Sparrow Limit* exist [45]. Rayleigh defines this overlap as the central maximum of one PSF coinciding with the second PSF's first minimum. Assuming the same shape for both PSFs, the Rayleigh Limit r_R can be defined as the distance between the central maximum and the first minimum of a single PSF. For the HQA objective and the wavelength $\lambda = 671\,\mathrm{nm}$ the Rayleigh Limit is $r_R = 624\,\mathrm{nm}$, compare the first minimum in Figure 3.4.

The resolution depends on the PSF's shape and size, which is incorporated in the Rayleigh Limit in two ways. First, Figure 3.4 shows that the size of the PSF depends on the wavelength. With decreasing λ, the PSF diameter decreases, and the resolution improves. For example, this fact can be applied in optical lattices, where smaller wavelengths, e.g., 532 nm, are used to achieve small lattice features [46].

Secondly, as illustrated later, the PSF depends on the objective's numerical aperture, as defined by Equation 3.5. Larger angles at which light can be collected enable the imaging of more minor details and narrow the PSF. Therefore, the resolution improves with a larger numerical aperture. Optical microscopes with high resolution, for example, commonly have a minimal working distance to keep the objective sizes

reasonable. Another way to increase the numerical aperture is to change the material's refractive index in front of the objective. For instance, immersion microscopes make use of the fact that fluids like oil have a refractive index $n > 1$ and can reach numerical apertures larger than unity [47].

Concerning the spatial resolution limits, it is essential to mention the type of light used in their definition. Since they rely on the intensity sum of two neighboring PSFs, the coherence of the light plays a significant role. For example, the Rayleigh and Sparrow Limits are only valid for incoherent and coherent light with a phase shift of $\phi = \pi/2$ between the two point sources. For more significant phase shifts up to $\phi = \pi$, the interference effects improve the PSF separation, while more minor phase shifts down to $\phi = 0$ result in a more substantial overlap. Therefore, the resolution for coherent light sources depends on the wavelength, the numerical aperture, and the respective phase.

For example, consider the two common imaging approaches in quantum simulators. During the absorption imaging of atoms, the recorded light stems from a laser source and is intrinsically coherent. Therefore, the non-existent phase shift diminishes resolution compared to incoherent light. During the fluorescence imaging of atoms, however, the recorded signal stems from scattered laser photons, which are, on average, not coherent anymore. The resolution of fluorescence images is therefore enhanced [48].

Field of View

The *field of view* (FOV) of a diffraction-limited microscope objective specifies the area in the focal plane where the optical performance behaves as specified. The objective introduces so few aberrations to the transmitted wavefront in this area that the RMS Maréchal criterion $W_{\mathrm{RMS}} < \lambda/14$ is fulfilled. While light from outside the FOV can still pass the objective, the wavefronts here will be distorted, and the resolution will decline with the distance from the FOV. We can simulate the RMS wavefront error W_{RMS} depending on the distance from the center optical axis with the software *Zemax*. The results are visible in Figure 3.5.

Each wavelength and the corresponding FOV belongs to a maximal angle θ_{max}, which depends on the objective focal length $f_{\mathrm{Objective}}$. Light rays, originating from a focal plane point, exit the objective as collimated light. If this point lies on the optical axis, the collimated light will be parallel to the optical axis. However, light rays collected from the FOV off-axis leave the objective with an angle. Each point in the FOV can be mapped to an output angle, depending on the point's radial distance to the optical axis. The angle θ_{max} describes the maximal angle between the optical axis and the collimated light coming from the edge of the FOV. Multiplying this angle by two gives the entire angular distribution of the collimated light exiting the objective. Table 3.2 presents the specified FOV diameters and the corresponding semi-angles.

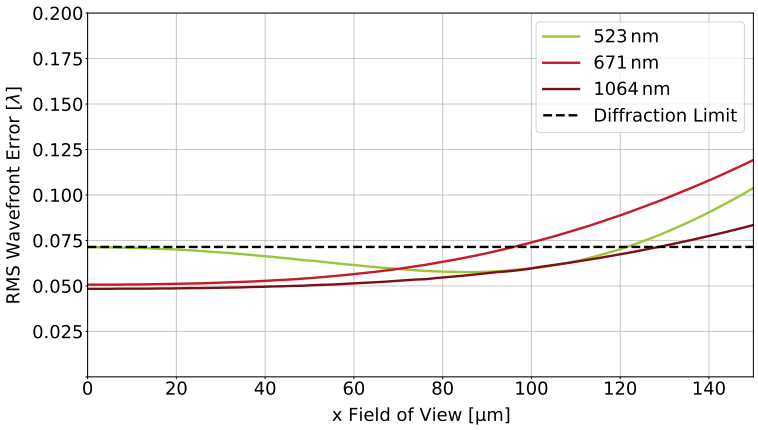

FIGURE 3.5: *Zemax* SIMULATION OF THE OBJECTIVE'S PERFORMANCE ACROSS ITS FIELD OF VIEW IN RADIAL DIRECTION.
The RMS wavefront error is displayed for three different wavelengths depending on the position in the field of view.
The dashed line marks the limit for the RMS diffraction-limited performance at $\lambda/14$.

TABLE 3.2: SPECIFIED FIELD OF VIEW DERIVED FROM FIGURE 3.5 AND CORRESPONDING MAXIMAL SEMI-ANGLES.
The angle θ_{max} describes the maximal angle between the optical axis and the light collected from the FOV exiting the objective.

Wavelength	FOV	Output Semi-Angle θ_{max}
532 nm	± 120 µm	6.4 mrad
671 nm	± 100 µm	5.3 mrad
1064 nm	± 130 µm	6.9 mrad

3.3.2 2D Fourier Simulation

As discussed above, the resolution and the PSF are essential for evaluating the performance of the microscope objective. Therefore, to determine the resolution, or in other words, the smallest structure the objective can still resolve, a sub-resolution light source is used in the experimental setup.

However, every point-like source will still have a finite physical size, ultimately blurring its image and increasing the recorded PSF size. To simulate this effect and understand the system's image propagation, the principles of Fourier optics can be applied to the 4f imaging setup.

Theory

The following formulas are loosely based on [42]. Fourier optics studies the propagation of light based on harmonic analysis. This procedure mathematically describes linear systems with an arbitrarily complex function $f(x, y)$ by the weighted superposition of basic harmonic wavefunctions, which are given by

$$F(\nu_x, \nu_y)\, e^{-j2\pi(\nu_x x + \nu_y y)}, \tag{3.10}$$

with the angular frequencies $\omega_{x,y} = 2\pi\nu_{x,y}$. This definition uses the spatial coordinates x and y and the spatial frequencies ν_x and ν_y, which are given in units of cycles per unit length with the respective x and y directions. The amplitude $F(\nu_x, \nu_y)$ assigns a weight to the harmonic functions, representing a two-dimensional plane wave. The function $f(x, y)$ can then be decomposed into single harmonic functions and is described by the superposition integral,

$$f(x, y) = \frac{1}{\sqrt{2\pi}} \int_{-\infty}^{\infty} \int_{-\infty}^{\infty} F(\nu_x, \nu_y)\, e^{-j2\pi(\nu_x x + \nu_y y)} d\nu_x\, d\nu_y, \tag{3.11}$$

where $F(\nu_x, \nu_y)$ is the Fourier transform of $f(x, y)$

$$F(\nu_x, \nu_y) = \frac{1}{\sqrt{2\pi}} \int_{-\infty}^{\infty} \int_{-\infty}^{\infty} f(x, y)\, e^{j2\pi(\nu_x x + \nu_y y)} dx\, dy. \tag{3.12}$$

This mathematical Fourier transformation has a physical representation in optical physics, with light being transformed by a single spherical lens. For example, consider a light wave with plane wavefronts and a spherical lens with a focal length of f_1. If the plane wave enters this lens at the angles θ_x and θ_y, the lens transforms this wave into a paraboloidal wave, centered at the point $(\theta_x f_1, \theta_y f_1)$. So, plane waves with different angles will be focused on a different point in the focal plane behind the lens. Generally, a light beam consists of many plane waves with different angles θ_x and θ_y. If such a light beam travels through the lens, all these plane wave contributions will be separated in the focal plane of the lens.

The function $f(x, y)$ is assumed as a light amplitude field in the plane $z = 0$, where z is the coordinate along the optical axis, and the light travels from this plane towards the lens. As described in Equation 3.11, this field can be decomposed into plane waves traveling at the angles $\theta_x = \lambda\nu_x$ and $\theta_y = \lambda\nu_y$. The lens focuses such a wave onto the point (x', y') in the focal plane, where the spatial coordinates depend on the angles via

$$x' = \theta_x f_1 \quad \text{and} \quad y' = \theta_y f_1. \tag{3.13}$$

The complex amplitude $f'(x', y')$ in the focal plane is therefore given by the Fourier transform of $f(x, y)$

$$f'(x', y') = h_l \cdot F(\nu_x, \nu_y) = h_l \cdot F\left(\frac{x}{\lambda f_1}, \frac{y}{\lambda f_1}\right), \tag{3.14}$$

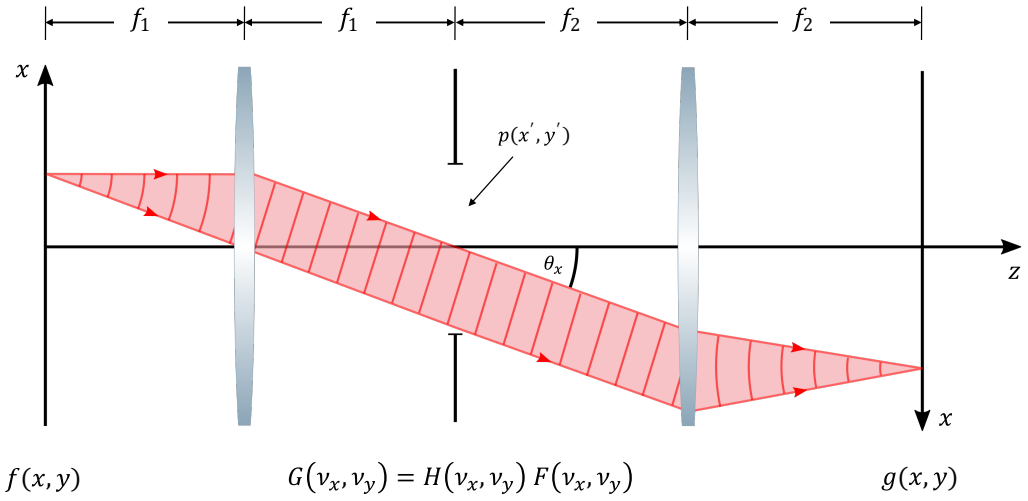

FIGURE 3.6: A DRAWING OF THE MAGNIFYING 4F IMAGING SETUP. The lens f_1 represents the objective, while f_2 will be the focusing lens in the experimental imaging setup. Each lens represents a Fourier transformation. The drawing is adapted from [42].

with the wavelength λ and a phase factor h_l. This phase factor becomes simple for a *2f-setup*, where the input function $f(x, y)$ lies in the front focal plane. In other words, the z-distance of $f(x, y)$ to the lens equals the focal length of the lens.

To conclude, a single lens is a physical representation of the mathematical Fourier transform. By describing light as a superposition of wavefunctions with a spatial frequency ν, Fourier optics can be used to explain light propagation through optical elements, like a thin lens. The complex amplitude of light in the back focal plane of such a lens is then simply the Fourier transform of the amplitude in the front focal plane, and vice versa. This theory will now be used in a more advanced setup.

The last section introduced the Fourier transforming property of a single lens. Now this concept will be carried toward a two-lens imaging setup, a so-called *4f setup*, depicted in Figure 3.6. The microscope objective will collect light from a point-like source for the resolution characterization in the next section. This source sits in the objective focal plane and emits Huygens-like spherical wavefronts, which are diffracted at a small aperture, travel through the objective, and exit as a plane wave. The objective acts like a single lens with a well-defined focal length and aperture for this light propagation. Then, the process is described by a 2f setup.

These planar wavefronts must be focused again to form a magnified image of the point-like source. For this, a second lens f_2 is introduced in the setup. To obtain a magnified image, the focal length f_2 is larger than the objective focal length f_1. This lens captures the collimated light and creates an image that a CCD camera can record. The magnification of this image is given by Equation 3.6. If the focal planes of both lenses coincide in the same plane between the lenses, this system can be labeled *4f setup*. Another advantage of a 4f setup is not only the re-imaging of a light source and its spherical wavefronts but also the propagation of plane wavefronts. A plane input wavefront is focused onto a spot by the first lens. Since this spot also lies in the focus of the second lens, the output wavefronts will be plane again. This would not be the case for a distance between both lenses, which is unequal to the sum of both focal lengths.

The light propagation in this setup will be again described with Fourier transformations. Both lenses combined perform a series of Fourier transformations. The first lens transforms the input field $f(x, y)$ into its Fourier transform $F(\nu_x, \nu_y)$, and the second lens performs an inverse Fourier transformation, resulting in the output field $g(x, y)$. Assuming a perfect imaging system, the output field $g(x, y)$ will be a perfect magnified replication of the input object $f(x, y)$. The plane in-between with the distances f_1 and f_2 from the respective lenses is called the *Fourier plane*. Here, the Fourier components with the spatial frequencies (ν_x, ν_y) are located at the spatial coordinates

$$x' = \lambda f \nu_x \text{ and } y' = \lambda f \nu_y. \tag{3.15}$$

Smaller frequency components will lie at the center of the Fourier plane, while higher frequencies are located further away.

In this plane, spatial filtering can be performed. In the Fourier plane, specific Fourier components are blocked by placing a mask, for example, a circular aperture. The inverse Fourier transformation will result in an aberrated replication $g(x, y)$ of the input field $f(x, y)$. Depending on the components blocked, the recorded image on the camera will have reduced quality compared to the input object. In the case of a circular aperture mask, higher frequencies will be blocked while lower ones pass freely through the center of the mask. The system then behaves as a low-pass filter, and the recorded image will be blurred. The filtering in the Fourier plane is given by the transfer function $H(\nu_x, \nu_y)$

$$G(\nu_x, \nu_y) = H(\nu_x, \nu_y) F(\nu_x, \nu_y), \tag{3.16}$$

with $G(\nu_x, \nu_y)$ as the Fourier transform of $g(x, y)$. It connects to the amplitude transmittance function $p(x', y')$ via

$$H(\nu_x, \nu_y) = p(\lambda f \nu_x, \lambda f \nu_y). \tag{3.17}$$

Assuming perfect lenses, the available Fourier components in the Fourier plane limit

the image quality of the *4f setup*. For no added mask, these components are determined by the system's smallest aperture stop, which, in our case, is the objective output aperture of $D = 24.8\,\text{mm}$. The distance of the objective to its back focal plane and thus the Fourier plane is about 1.8 mm. Thus, it will be assumed that the output aperture D of the objective acts as a circular mask in the Fourier plane of the system. With the cut-off frequency ν_{cut} and the edge of the aperture mask at $D/2 = \lambda f \nu_{\text{cut}}$, the transfer function is then given by

$$H(\nu_x, \nu_y) = p(\lambda f \nu_x, \lambda f \nu_y) = \begin{cases} 1 & \text{if } \sqrt{\nu_x^2 + \nu_y^2} < \frac{D}{2\lambda f} \\ 0 & \text{otherwise} \end{cases} \tag{3.18}$$

The objective's aperture essentially acts as a low-pass filter and introduces a blur on the recorded camera image.

Simulation

The light propagation through the 4f imaging setup will be simulated using digitally created images. The formulas above show that a series of simple Fourier transformations describe the spatial filtering of the objective in a simple mathematical way. Using *Python*, these transformations can easily be performed on 2D digital images represented by 2D arrays. The source image $f(x, y)$ resembles the nanopores used in the experimental setup. For now, their shape is assumed as a uniformly illuminated circular aperture, a top-hat function, which should be a good first approximation for the nanopores. However, since the simulation works with 2D arrays of pixels, any shape could be used.

The simulation takes the source image $f(x, y)$ and performs the first lens transformation. If $f(x, y)$ is a simple circle, then the amplitude of the Fourier transformation is given by the zero-order Bessel function of the first kind J_1

$$FT(f(x,y)) = F(\nu_x, \nu_y) = A_0 \left[\frac{2J_1(\pi D r/\lambda z)}{\pi D r/\lambda D} \right], \quad r = \sqrt{x'^2 + y'^2}, \tag{3.19}$$

with the radius r from the optical axis and the distance z along the optical axis [49]. The coordinates x' and y' in the Fourier plane can be converted into the frequency components ν_x and ν_y with Equation 3.15. $F(\nu_x, \nu_y)$ describes the light distribution in the Fourier plane behind the objective for coherent light. However, for a circular aperture illuminated by incoherent light, one needs to take the square $(FT(f(x,y)))^2$, which yields the Fraunhofer diffraction pattern of a circular aperture. This pattern is the well-known *Airy Disk* pattern. In this case, however, the radiation used is coherent laser light. Thus, the incoherent Airy Disk would be slightly inaccurate in the Fourier plane due to interference effects. The correct function for coherent light propagation is the non-squared $F(\nu_x, \nu_y)$, which also contains negative values. A phase mask in the Fourier plane will transmit slightly different frequency parts for incoherent and coherent light.

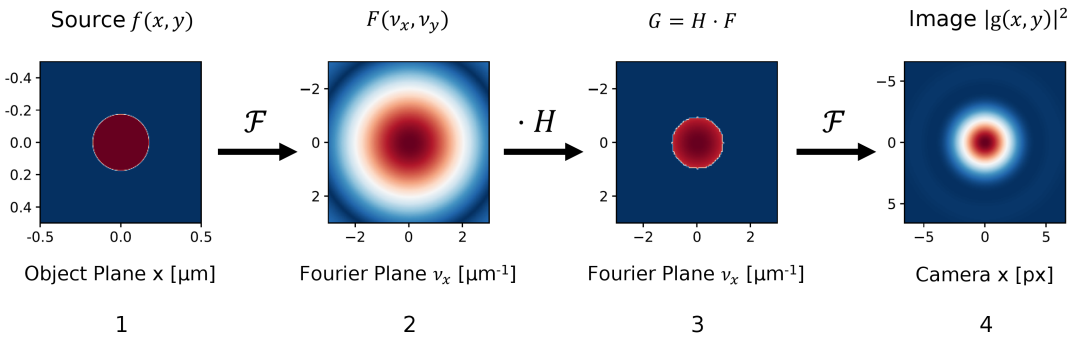

FIGURE 3.7: THE NUMERICAL FOURIER SIMULATION OF THE 4F SETUP.
1: Image of the object plane. The sampling of the image is 20000 px per axis. A top-hat function generates a single nanopore with a diameter of 350 nm.
2: The object plane is Fourier transformed, and the Airy Disk distribution is the result.
3: The Fourier plane is truncated by a pupil with transfer function H. The real space aperture is $D = 24.8\,\text{mm}$, corresponding to $|\nu_{\text{cut}}| = 1\,\mu\text{m}^{-1}$ in the reciprocal space. The resulting amplitude distribution is similar to a top-hat again.
4: The truncated Fourier plane is transformed back, and due to the top-hat-like shape, a second Airy Disk is produced after the 4f setup, i.e., on the camera. The coordinates are determined by the magnification of $M = 16$ and a pixel size of $d_{\text{pixel}} = 2.4\,\mu\text{m}$.

In the next step, the image in the Fourier plane is truncated by the objective aperture. A circle with radius ν_{cut} gives the mask $H(\nu_x, \nu_y)$, marked by the white circle in Figure 3.7. Since the mask is significantly smaller than the central peak of the Fourier transformation, the effective image before the second lens is very similar to a circular aperture. Therefore, the inverse Fourier transformation resembles the coherent Airy Disk distribution. The complex amplitude $g(x, y)$ needs to be squared to arrive at the intensity of the simulated camera image. This changes the image slightly, as seen in the last image in Figure 3.7. For a more detailed analysis, Figure 3.8 shows the cross-sections of the coherent $g(x, y)$ and the incoherent Airy Disk $|g(x, y)|^2$. Both figures show a reduction of the secondary maximum due to the squaring of the amplitude.

To get the correct camera image size, the magnification M also needs to be considered. Hence, the image $FT(G(\nu_x, \nu_y))$ is scaled by M and the pixel size $d_{\text{pixel}} = 2.4\,\mu\text{m}$, taken from the *FLIR Blackfly* CCD camera [50] used in the experimental setup later. The correct scaling for the axes in the last image in Figure 3.7 is obtained.

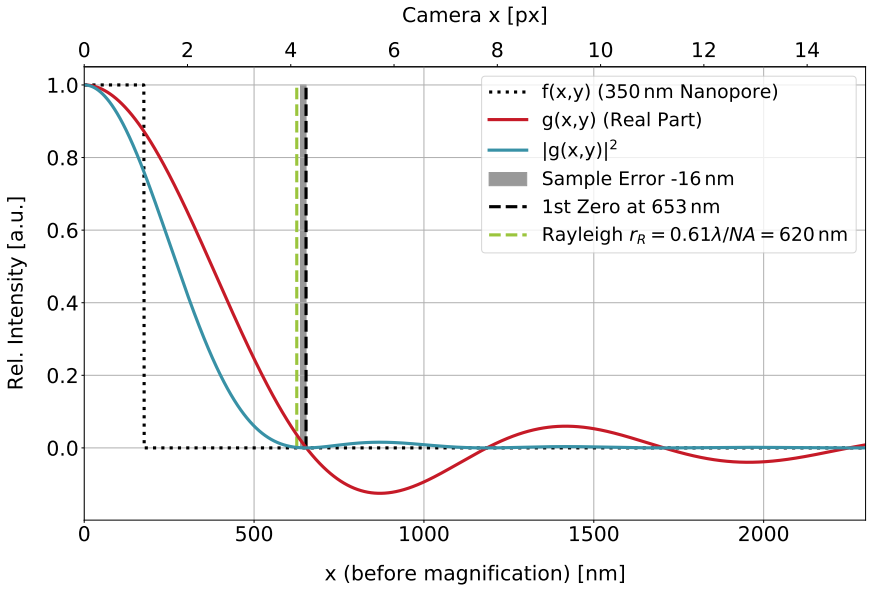

FIGURE 3.8: SIMULATED CROSS-SECTIONS OF THE IMAGED NANOPORE. The simulated nanopore has a diameter of 350 nm, plotted to give an intuition of the image blurring. The red and blue curves show the light field after the second Fourier transformation. The blue curve is the squared amplitude and thus represents the camera image. The lower x-axis does not include the magnification of the 4f setup yet. However, the axis on top in units of camera pixel does. The sample size is maximized for the given computational limits to obtain the smallest error.

Figure 3.8 shows the cross-sections of the intensities before and after the 4f setup. The blurring of the rectangular input intensity of the nanopore with a diameter of 350 nm is shown by the curve $|g(x,y)|^2$. It depicts the expected image for the experimental nanopore recording. The first minimum of the recorded PSF should be located at $M \cdot 653\,\text{nm}$, with the magnification M of the 4f setup. The distance from the center to the first minimum is the *radius* of the Airy disk. This radius can be compared to the Rayleigh Resolution Limit in Table 3.1. Between the first zero of $g(x,y)$ and the Rayleigh Limit lies a slight deviation of $653\,\text{nm} - 620\,\text{nm} = 33\,\text{nm}$, which must be corrected for the sampling error. Then, the deviation becomes $637\,\text{nm} - 620\,\text{nm} = 17\,\text{nm}$. Therefore, the finite hole diameter causes only an insignificant larger radius $M \cdot r_{\text{theo}} = M \cdot 637\,\text{nm}$ of of the nanopore image recorded by the camera.

In this simulation, the absolute amplitude in the images has been ignored. Since the radius to the first minimum is independent of the PSF amplitude, only the relative intensities within the images are required. Thus, the images in Figure 3.7 and the curves in 3.8 are normalized to their respective maximum.

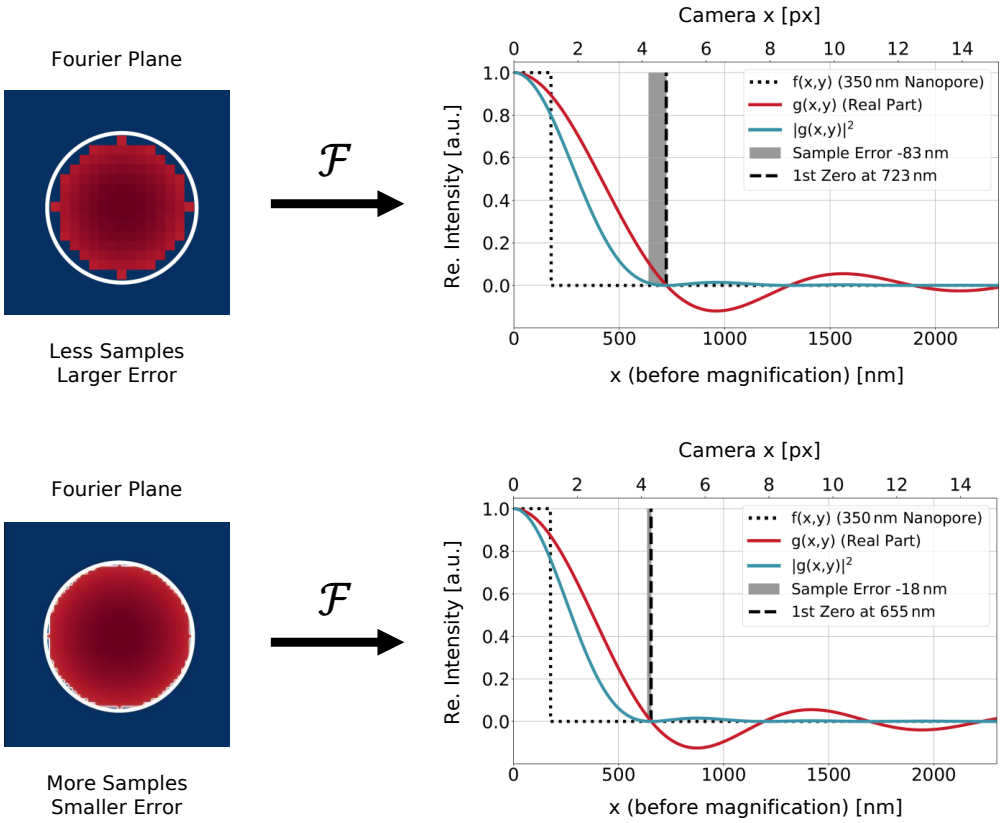

FIGURE 3.9: SAMPLE SIZE IMPACT ON THE SIMULATED RESOLUTION. The 2D simulation is performed on digital images of a finite sample size. The resolution in the Fourier plane is given by the total sample size, which is limited by the available computer memory. Due to the numerical approximation of the circular truncation, a deviation from a perfect ring occurs. Thus, the final Airy distribution deviates from the correct reverse transformation. This deviation is calculated via 3.24 and is shown by the grey shift of the first Airy minimum above.

Simulation Error

The limited sampling of the mask in the Fourier plane results in a smaller effective aperture than given by $|\nu_{\text{cut}}|$. Therefore, more frequency components will be truncated, the resulting distribution $g(x,y)$ will be broader, and the radius of the Airy disk will be larger. Figure 3.9 illustrates this behavior.

This Airy radius depending on the mask aperture D in the Fourier plane, is given by the Rayleigh Limit

$$r_{\text{R}} = 0.61\frac{\lambda}{NA} = 0.61\frac{\lambda 2f}{D} = 0.61\frac{1}{|\nu_{\text{cut}}|}. \tag{3.20}$$

with the largest transmitted frequency component $|\nu_{\text{cut}}| = D\lambda f/2$. The digital sampling of this mask will lead to an effective aperture D_{eff} and, therefore, an effective

radius

$$r_{\mathrm{R,\,eff}} = 0.61\frac{\lambda 2f}{D_{\mathrm{eff}}} = 0.61\frac{1}{|\nu_{\mathrm{eff}}|}. \tag{3.21}$$

The effective radius of the sampled mask can be calculated with

$$|\nu_{\mathrm{eff}}| = \sqrt{\frac{A_{\mathrm{eff}}}{\pi}}, \tag{3.22}$$

including the area A_{eff}, which is the area covered by all samples in the Fourier plane with an amplitude > 0. The sum over all single samples gives this area

$$A_{\mathrm{eff}} = \sum A_{\mathrm{sample}} = \sum \left(\frac{1}{n_{\mathrm{samples}}}\right)^2. \tag{3.23}$$

Here, the total sample size n_{samples} is the number of pixels chosen for a simulated image. The digital sampling error Δr_{sim} of the simulated resolution then becomes

$$\Delta r_{\mathrm{sim}} = r_{\mathrm{R,\,eff}} - r_{\mathrm{R}} = 0.61\,\lambda\,2\,f\left(\frac{1}{D_{\mathrm{eff}}} - \frac{1}{D}\right) = 0.61\left(\frac{1}{|\nu_{\mathrm{eff}}|} - \frac{1}{|\nu_{\mathrm{cut}}|}\right), \tag{3.24}$$

which arises due to a deviation on the mask H in the Fourier plane. However, the finite hole diameter can still influence the truncated distribution and, therefore, the camera image.

3.3.3 Sub-Resolution FOV Probing

As discussed before, the resolution derived from the PSF poses a valuable figure of merit in characterizing a high-*NA* objective. The detailed analysis of the PSF can provide a great insight into the objective's performance. Especially scanning the PSF across the entire FOV allows multiple conclusions.

First, it delivers a detailed picture of the FOV itself. Scanning the image of a point emitter across the FOV gives the achievable resolution depending on the position in the imaged plane. In HQA, this will be the plane of the atoms. Due to the radial symmetry of the objective lenses, one also expects a radial symmetry in the resolution distribution.

Secondly, this distribution allows a measurement of the optical axis alignment. If a laser beam enters the objective from the back side, it will hit the nanopore frame, and the scattered light will be visible as a point on the nanopore image. If this beam is perfectly centered and orthogonal with respect to the objective housing, the imaged point will indicate the *mechanical axis*. The position of this point can be compared with the scanned FOV and its center, which represents the *optical axis*. Figure 3.10 illustrates both axes. The angle between these axes corresponds to the output angle of the collimated imaging light coming from the center of the real FOV. Therefore, the light captured from this location will deliver the best imaging resolution. Further, a tweezer beam, for which the best optical performance is desired, must be aimed at this FOV center and therefore needs the input angle α.

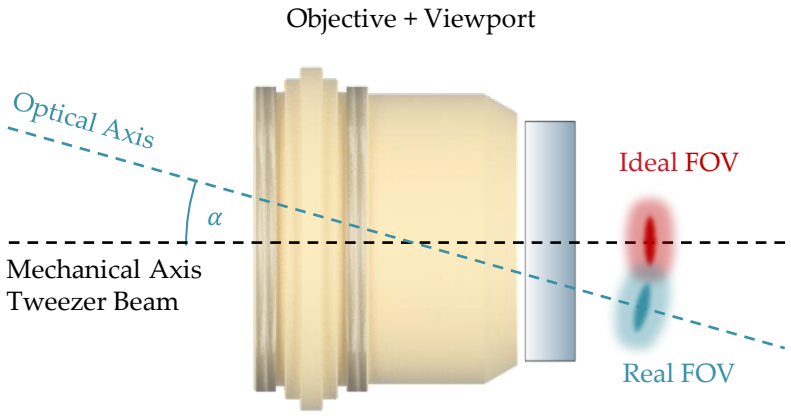

FIGURE 3.10: ILLUSTRATION OF THE MECHANICAL AND OPTICAL AXIS. The ideal FOV lies on the axis normal to the objective mechanical housing. This axis will be measured by a tweezer beam coming from the left. The scattered light on the nanopore membrane will define the position of the ideal FOV. On the other hand, the real FOV is defined by the center of the area with the best resolution, which will be measured with the nanopores and the recorded PSF. For a passively mounted objective, the angle α has to be considered for the objective mount. Note that the angle between the axes is not to scale. The objective scale on paper is 1:1.

Thirdly, the shape of the PSF provides information about eventual aberrations in the optical system. These could be, for example, *Coma* or *Astigmatism*, which can occur due to misaligned optics. More details on PSF aberrations can be found in [51, 52].

Nanopores and the Optical Setup

Designed with this task in mind, the characterization breadboard introduced in Section 2.2.2 operates as the foundation for the FOV probing. It offers predefined mounting positions for the optical and mechanical components, visible in Figure 3.11. Two inlets for the mounting cage plates fix the position of the objective and the glass window. The piezo stages are screwed down, so their travel range covers the theoretical objective FOV. The designed optical axis of the objective and the glass window mounted on this breadboard lies at the standard 50 mm beam height above the lab table, which ensures compatibility with the optomechanics in our lab. A slightly wider cage plate inlet was incorporated into the breadboard to investigate the effect of a tilted glass window on the PSF. This way, a tilt around the vertical axis of ca. (7.7 ± 0.7) mrad is achievable. The tilt around the horizontal axis can be realized with a screw putting mechanical pressure on the mounted cage plate. It allows for a tilt range of roughly 0.8 mrad. The tilt angles were determined using a caliper to measure the four corner distances of both the objective and glass window cage plates. The caliper scale, therefore, gives the uncertainty on the angle.

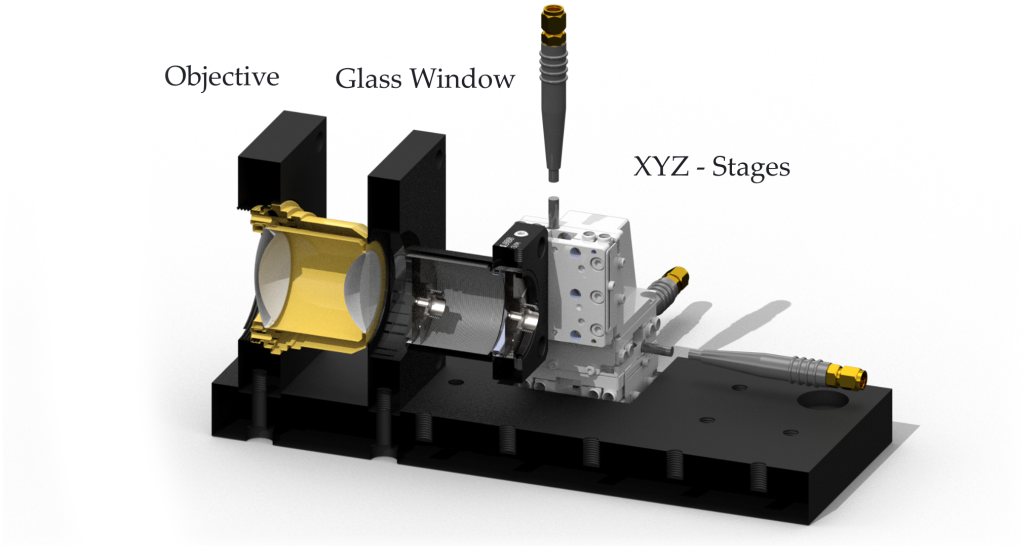

FIGURE 3.11: CROSS-SECTION OF THE CHARACTERIZATION TEST BENCH. All mechanical and optical components except the laser fiber are depicted. The 30 mm cage plate was switched for a smaller lens mount in the experimental setup to reduce stage load.

As a point emitter, sub-resolution nanopores manufactured by *Norcada* [53] were used. This product consists of a 5 mm x 5 mm silicon frame, which contains a 0.30 mm x 0.10 mm Silicon Nitride membrane with a thickness of 50 nm. A coating with 5 nm chromium and 50 nm gold is also applied on both sides. Inside the membrane lie two nanopores with a pitch of 7 µm and a diameter of 350 nm each, as specified in the device's datasheet.

A *Thorlabs SM1FCA2* fiber adapter has been chosen to mount the nanopore frame in the optical setup. The frame is carefully glued onto the opening hole of this threaded adapter, which is then easily screwed into a lens tube. To illuminate the nanopores, a laser fiber is attached to the other side of the tube. A *Toptica* laser produces a fiber-coupled beam with a wavelength of 671 nm. Two different laser powers will be used. A greater light intensity, which illuminates the membrane around the nanopores, helps to locate the device in the camera view. A rough manual positioning is performed to achieve this, followed by a more precise translation by linear translation stages. When the membrane is visible and the nanopores are focused on the camera, the power is reduced such that the PSF image is below CCD saturation.

To scan the PSF across the entire objective FOV, the nanopores must be moved in small steps over a wide range. Many data points with different nanopore positions will allow for a comprehensive scan. For this, electrical linear translation stages will be used since they allow a small step size and digital control. The *Thorlabs ORIC* piezo stages, mounted in a three-axis XYZ setup, translate the nanopores inside the objective focal plane. Their steps are specified with a typical size of 1 µm and a range

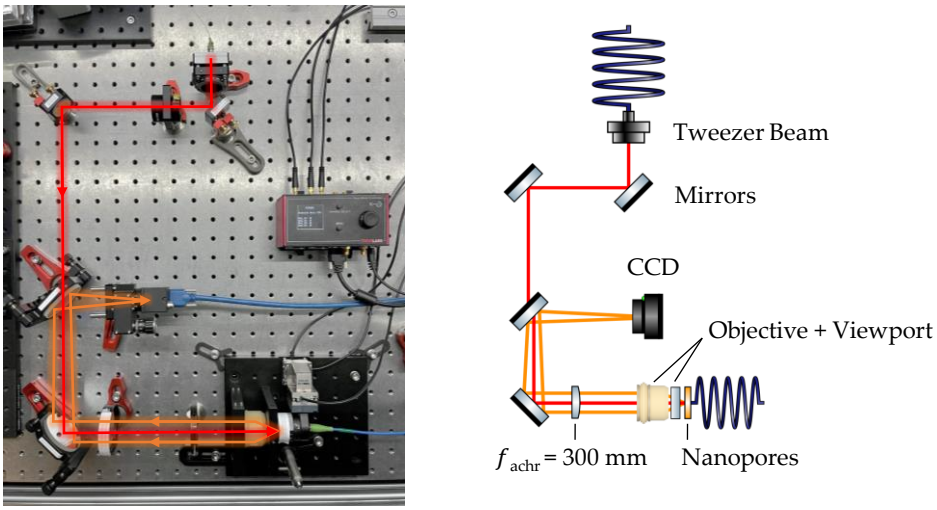

FIGURE 3.12: OVERVIEW OF THE EXPERIMENTAL NANOPORE SETUP. Components are not precisely at the 4f positions, which becomes relevant for the later measurement of the Fourier plane truncation.
Since the actual Fourier plane of the objective lies too close to the last lens, the iris is placed a few millimeters further along the collimated beam path. For these measurements, however, only an on-axis nanopore image was recorded. The light exiting the objective is, therefore, parallel to the optical axis, and the misplacement of the iris becomes negligible.

of 20 mm [54]. Since these stages are open-loop, no feedback system is implemented, and the stepsize depends on the workload. If the stage must exert a large force, its stepsize will be smaller. To determine the stepsize for a loaded stage, one must calibrate it by measuring the traveled distance per step. The calibration depends on external parameters like the load distribution or the flatness of the surface the stages are mounted on. While these parameters can be optimized and a rough calibration is achievable, a closed-loop stage is generally preferred.

The *optical setup* is inspired by the 4f setup, already discussed with Figure 3.6. The experimental setup on the table is presented in Figure 3.12. The imaging light leaves the objective collimated and reaches the second lens f_{achr}, chosen such that the objective FOV fits on the CCD chip while the PSF is still large enough. A focal length of $f_{\text{achr}} = 300\,\text{mm}$ [55] strikes the optimal balance and results in a magnification of $M = 16$. For this measurement, it is crucial that no other optical component but the objective limits the imaging performance. So an *Achromat* is used instead of a spherical lens. This lens type introduces fewer aberrations and therefore offers a higher quality focus [55].

Two 2" mirrors guide the collimated beam towards the CCD camera, which sits at the distance f_{achr} from the second lens. The beam path behind the second lens and the camera's position was aligned with a collimated guiding beam from a fiber.

The *mechanical axis* of the objective will be the reference for the center of the measured FOV. It is determined by a tightly collimated laser beam, which will be called *tweezer beam*. To leave the imaging path as untouched as possible, this beam is injected through the back of the dielectric mirror in front of the camera (see Figure 3.12). The position of this beam is aligned to the center of the beam aperture using a Thorlabs cage alignment tool. The angle of this beam with respect to the objective is sensitive since it determines the tweezer beam position in the objective focal plane and on the camera image. This beam is aligned with a pinhole aperture and a mirror pressed against the objective mount. The tweezer beam passes two tiltable mirrors before entering the imaging path. While observing the overlap of this beam with its reflection on the mirror on the objective, the tweezer beam is aligned using the two tiltable mirrors. At a 35 cm distance from the objective, this overlap is achieved with an estimated accuracy of $\Delta s_{\text{overlap}} = 0.5\,\text{mm}$, which produces an uncertainty of $\Delta s_{\text{tweezer}} = 27\,\mu\text{m}$ for the tweezer beam position in the focal plane. This error will determine the precision by which the angle between the mechanical and optical axis can be evaluated in the data analysis below.

Finally, the automatic recording of the data points is performed. The piezo translation stages move the nanopores across the objective FOV. The automated scan of the PSF will be performed by a python program, controlling the *FLIR Blackfly* CCD camera and the translation stages. The program starts with a dark image recording, which can be used to minimize the background noise of the recorded images. The program then continues with the iterative scan of the FOV. With a stepsize of ca. 13 µm, the translation stages automatically move the nanopores in an array-like fashion across the FOV. After each step, the camera takes an image, and the program stores it on the hard drive.

Since the translation stages are open-loop, the step parameters must be monitored carefully. If the step size is too large or too small, the nanopores will be moved out of the camera FOV. For example, consider the number of steps specifying the distance traveled for each column. The summed-up distance needs to match the reset travel to reach the start of the column. Any miscalibration in the reset distance will result in a sequential shift of the column's vertical position and, ultimately, a tilted scan.

Analysis

When the FOV scan is finished, the program opens each image, locates the PSF, and performs a Least-Squares-Fit. An ideal PSF image would be perfectly round. Aberrations, however, can distort this image. For example, to the edge of the FOV, the PSF will be elongated in the radial direction. To include these aberrations in the analysis, a 2D Gaussian is used as the fitting model across the FOV. Thus, the fit works even for a PSF deviating from the Airy function. The resulting fit parameters produce the Gaussian $\sigma_{x,y}$ along the major and the minor axes of the fitted ellipse

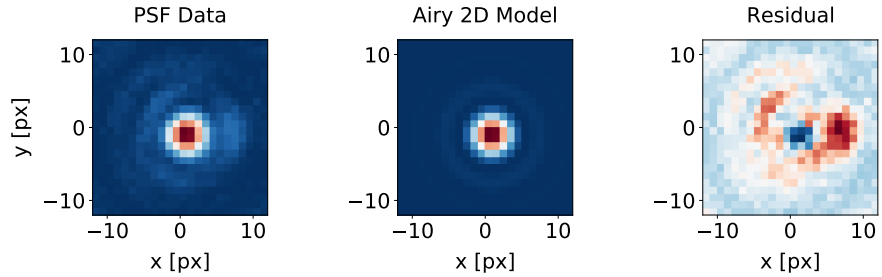

FIGURE 3.13: THE 2D AIRY DISK MODEL FITTED TO THE BEST PSF IMAGE. The laser power is chosen such that no pixel is saturated. Intensities are normalized. The best PSF gives the data, determined by the minimal resolution r_{min}.

and the rotation angle θ_{rot} for each recorded PSF image. The σ can be converted from units of camera pixels into units of the atom plane

$$\sigma_{x,y}^{\text{atom}} = \sigma_{x,y} \cdot \frac{d_{\text{pixel}}}{M}, \tag{3.25}$$

with the pixel size d_{pixel} and the magnification M.

The first minimum generally determines the radius r of a PSF in the Airy Disk function (see Figure 3.8). To convert the σ-value of the 2D Gaussian fit into the correct radius, an additional Airy Disk function was fitted on the best-recorded PSF image. This image and the fit are visible in Figures 3.13 and 3.14. Comparing the σ-value of the Gaussian fit with the Airy Disk radius r_{Airy} yields a conversion factor $g_{\text{gaussian}} = \sigma / r_{\text{Airy}} = 2.66$.

To obtain a single resolution value, even for a distorted PSF, the radius r for a single PSF is averaged between both ellipse axes

$$r = \frac{r_x + r_y}{2} \cdot g_{\text{gaussian}}, \tag{3.26}$$

and the deviation from each of the axes becomes the error

$$\delta r_{\text{ell}} = \frac{|r_x - r| + |r_y - r|}{2}. \tag{3.27}$$

Two additional error sources must be considered in the total resolution error Δr. The covariance error of the fit function yields δr_{fit}, while the misplacement of the nanopore on the optical axis yields δr_{M}, which is based on the limited step size <3 µm, of the translation stages used for focusing. If the position of the nanopore on the optical axis has the uncertainty $\Delta g = 1\,\mu\text{m}$, it will result in an error in the magnification. The magnification can be expressed as the ratio of the object g and the image b distance

$$M = \frac{b}{g} = \frac{f_{\text{tot}}}{g - f_{\text{tot}}}. \tag{3.28}$$

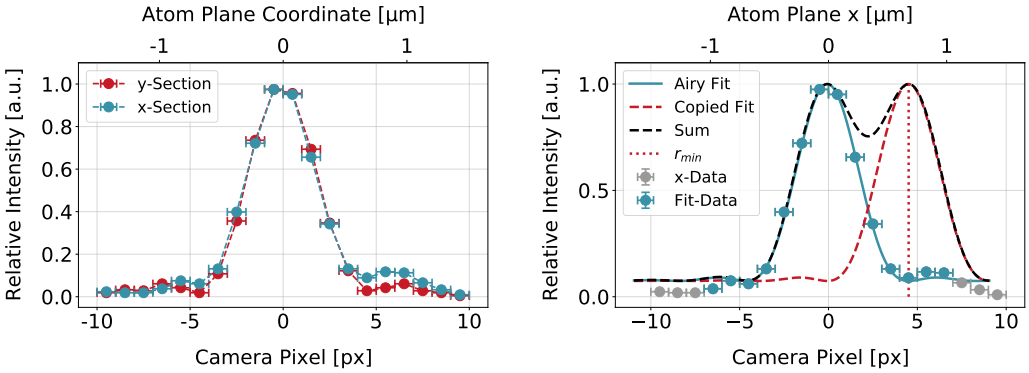

FIGURE 3.14: CROSS-SECTIONS OF THE BEST PSF IMAGE INCLUDING FIT. A single camera pixel integrates the light intensity impinging on its total area. Therefore, the exact position of the measured intensity in both planes has an uncertainty of $d_{\text{pixel}}/2$.
LEFT: The x and y cross-sections of the recorded nanopore PSF in Figure 3.13.
RIGHT: The y cross-sections of the data and the fitted model. Additionally, a copy of the model is placed at the fitted resolution distance $r_{\text{min}} = (704 \pm 31)$ nm from the PSF center. The dashed black curve gives the incoherent intensity sum of two point sources separated by the resolution limit r_{min}. This sum could, for example, be two atoms in a pinning lattice.

Here, the lens equation [56] with the total focal length f_{tot} of the system has been used

$$\frac{1}{f_{\text{tot}}} = \frac{1}{b} + \frac{1}{g} = \frac{1}{f_{\text{obj}}} + \frac{1}{f_{\text{achr}}}. \tag{3.29}$$

The errors of the specified focal lengths are assumed to be negligible. The impact of the magnification error ΔM on the resolution is then

$$\delta r_{\text{M}} = \left|\Delta M \frac{r}{M}\right| = \left|\frac{f_{\text{tot}}}{(g - f_{\text{tot}})^2} \Delta g \frac{r}{M}\right| \tag{3.30}$$

and the largest estimate of the resolution error becomes the sum of all errors above

$$\Delta r = \delta r_{\text{ell}} + \delta r_{\text{fit}} + \delta r_{\text{M}}. \tag{3.31}$$

This error calculation does not include slight aberrations introduced by the mirrors and the achromatic lens. Additionally, the tilt of the CCD camera with respect to the optical axis is ignored and assumed to be negligible. However, these factors still need to be considered during the assembly of an optical setup like this.

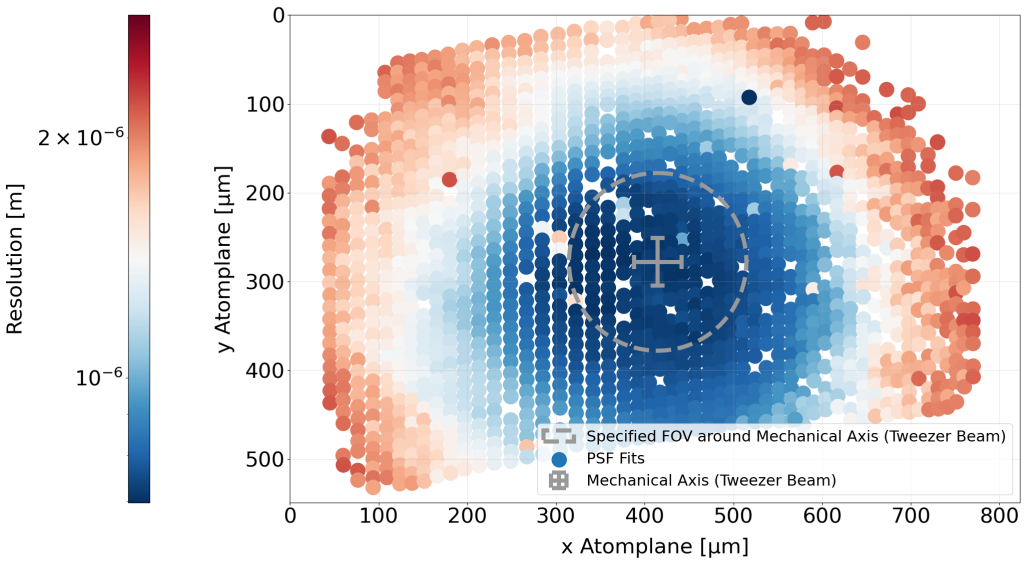

FIGURE 3.15: RECORDED DATA POINTS ACROSS THE WHOLE CCD CHIP. The markers have a constant size, and their color depicts the resolution. To improve the readability of the resolution across FOV, the color scale is chosen as logarithmic. The radius of the FOV is the specified 100 µm. A slight miscalibration of the translation stages causes the scan's skew, visible at the bottom of the figure.

Resolution Results

The measured PSF radius r will be called *resolution*. In Figure 3.15 the resolution is plotted across the whole camera field of view. The x- and y-units are converted from camera pixels into the corresponding atom plane lengths, analog to Equation 3.25.

A two-dimensional third-degree polynomial is fitted on the resolution values across the FOV. The resulting 2D function is displayed in Figure 3.16 with two cross-sections located at its minimum. The area around this minimum, where the resolution is $r < 110\,\% r_{\mathrm{min}}$, somewhat arbitrarily defines the measured FOV. The first black circle in Figure 3.16 depicts this area, while the additional contour lines continue outwards in 0.2 µm steps. The mean resolution in this FOV is calculated to $\bar{r} = (757 \pm 5)$ nm. The minimal measured resolution is $r_{\mathrm{min}} = (704 \pm 31)$ nm, located in the same FOV. For comparison, the theoretical value obtained by the Fourier Simulation $r_{\mathrm{theo}} = 637$ nm lies within the 3σ-range of r_{min}.

Alignment of the Optical Axis

In the subsequent analysis step, the angle between the objective's optical and mechanical axis is determined by their respective positions in the focal plane. The position of the mechanical axis is measured with a tweezer beam, which is centered orthogonally on the objective, as described in Section 3.3.3. The tweezer beam is

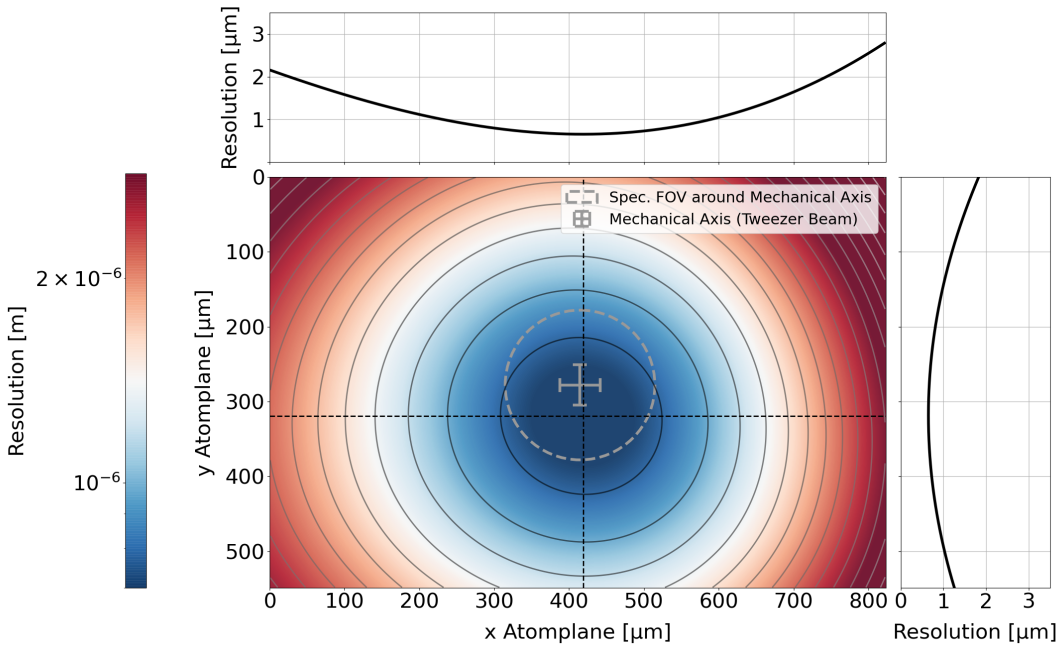

FIGURE 3.16: POLYNOMIAL FIT TO THE NANOPORE DATA POINTS. To improve readability, the resolution color scale is logarithmic. The contour lines start at $r = 110\,\% \, r_{\text{min}}$ and are equidistantly depicting a change in resolution of 0.2 µm. Two cross-sections at the polynomial minimum are plotted. The distance between the fitted minimum and the tweezer beam is $s_{\text{axes}} = (42 \pm 30)$ µm, which yields the angle between the mechanical and optical axis $\alpha = (2.2 \pm 1.6)$ mrad.

scattered on the nanopore frame and recorded on the camera. The signal on the recorded image is fitted with a 2D Gaussian. Its position and alignment uncertainty $\Delta s_{\text{tweezer}}$ are illustrated by the grey cross in Figures 3.15 and 3.16. The dashed circle depicts the specified FOV of ±100 µm.

Next, the position of the optical axis in the focal plane is required. It will be given by the minimum of the measured FOV, which is determined by the two-dimensional polynomial. Comparing the FOV minimum and the tweezer position yields the distance between the mechanical and optical axis in the focal plane $s_{\text{axes}} = (42 \pm 30)$ µm. The angle can be calculated by

$$\alpha = \tan^{-1}(s_{\text{axes}} / f_{\text{objective}}) \, . \tag{3.32}$$

With the focal length of the objective $f_{\text{objective}} = 18.8$ mm, finally the angle between the optical axis and the mechanical axis is obtained

$$\alpha = (2.2 \pm 1.6) \text{ mrad}. \tag{3.33}$$

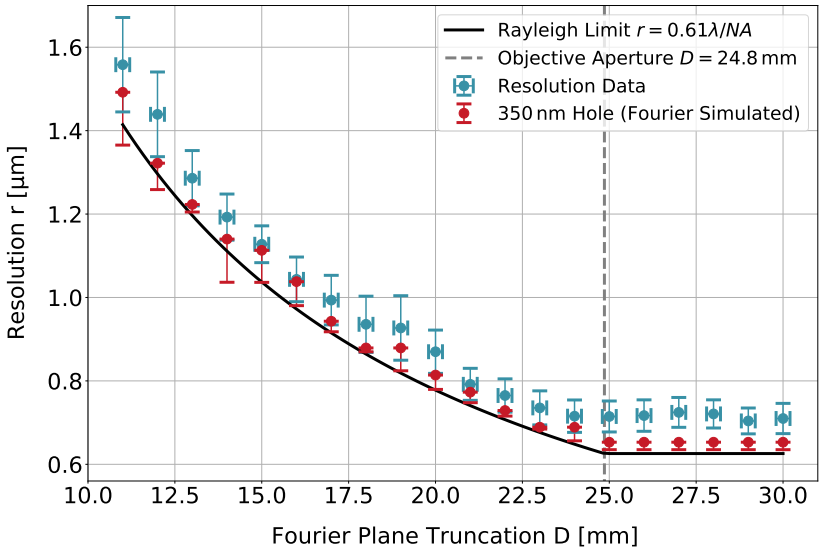

FIGURE 3.17: RESOLUTION LOSS DUE TO FOURIER PLANE CLIPPING. The upper limit of the Fourier simulated aperture is the objective aperture $D = 24.8\,\mathrm{mm}$. The error of the simulated red data points stems from the limited sample size in the Fourier plane, which is discussed above.
As a result, all optics in the collimated beam path after the objective should be large enough not to clip the roughly 1 ″ large beam while considering the angles from 3.2. Otherwise, the objective will not be utilized to its full potential.

Fourier Plane Truncation

The study of the PSF across the objective FOV has already delivered promising results for the objective. However, the PSF is also affected by components in the collimated beam path after the objective. As the first step in this direction, a tunable aperture was placed in the Fourier plane of the objective. This allows a variable truncation of the collimated beam in the Fourier plane. A smaller free aperture will stop higher frequency components from contributing to the camera image. Thus, a clipping by the aperture will increase the PSF's size and diminish the resolution. This is confirmed by a measurement of the PSF resolution performed on a single on-axis image in the same way as above. The data is shown by the blue data points in Figure 3.17. Their resolution error is given by Equation 3.31, and the truncation error stems from the uncertainty of the caliper measurement of the iris diameter.

The simulation from Section 3.3.2 features a tunable Fourier plane truncation and thus allows a simulation of the measured resolution. In Figure 3.17, the data points from the simulated PSF are displayed in red. The upper aperture of the simulation is limited at the objective aperture D. Hence, the red points converge to a horizontal line. The irregularities of these points occur due to the computational limits of the Fourier simulation.

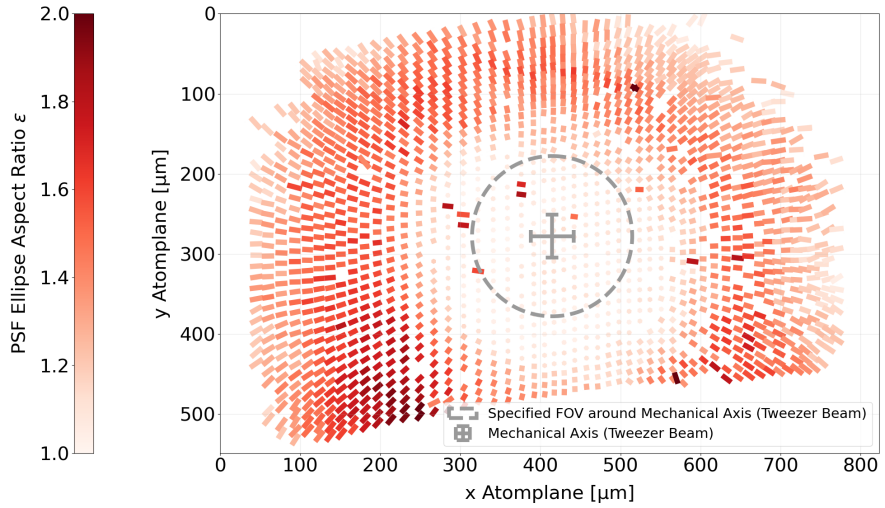

FIGURE 3.18: THE RECORDED PSF ELLIPSE ACROSS THE OBJECTIVE FOV. Each datapoint's orientation and length represent the PSF ellipse's major axis. The ellipse aspect ratio gives the color scale, which increases for more elongated PSFs.
In the FOV, the PSF is essentially round, while aberrations stretch the PSF outside the FOV. Outside the FOV, spherical aberration stretches the PSF in the radial direction, which is expected behavior for microscope objectives, and apart from that, no significant aberrations are apparent. The length of each data point is not to scale.

The black curve displays the Rayleigh limit for an ideal point source

$$r_{\text{Rayleigh}} = 0.61\frac{\lambda}{NA} = 0.61\frac{\lambda 2f}{D}. \tag{3.34}$$

For a point source significantly smaller than the wavelength, e.g., an atom, the resolution is expected to approach this ideal limit.

A slight systematic deviation between the measurement and the simulated data is apparent at all apertures. A possible explanation could be a systematic error due to plasmonic effects, which produce a light field around the sub-wavelength nanopore [57]. These plasmons could make the light distribution, transmitted by the nanopore and its membrane, appear more prominent than the specified diameter. Furthermore, the combination of multiple minor aberrations, e.g., introduced by the two mirrors or the viewport, could distort the PSF on such small scales.

3.3.4 Aberrations

Spherical aberrations outside the FOV will result in a distortion of the PSF. To analyze this property of the PSF ellipse, the 2D Gaussian fit of the PSF ellipse yields the rotation angle θ and the aspect ratio ϵ of the major and minor ellipse axes. Figure 3.18 displays these properties across the FOV. The median aspect ratio in the FOV

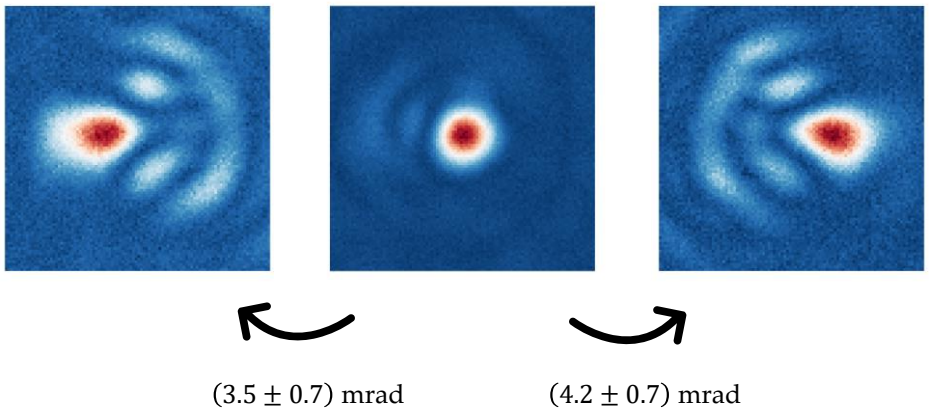

FIGURE 3.19: IMPACT OF THE TILT BETWEEN THE OBJECTIVE AND THE VACUUM VIEWPORT.
Coma aberrations are introduced by a slight tilt between the vacuum window and the objective. The tilt angles are recorded by caliper measurements. For the impact of other aberrations on a PSF, see [51, 52].

is $\bar{\epsilon}_{\mathrm{FOV}} = 1.06$, while the PSF is elongated radially outside of the FOV. Keeping this in mind, one could even operate the objective in this area if the focus quality is not the top priority. Apart from the expected spherical aberration outside the FOV, no significant aberrations were detected. However, this changes for misaligned optics in the imaging path.

It was observed that components in the beam path of highly converging or diverging beams are the most critical. In this setup, the alignment of the high-*NA* objective and the vacuum window is the most sensitive. A slight tilt of the window or the objective will diminish the PSF and the resolution. The small wiggle room of the window mounting plate allows one to get familiar with the alignment. First, the alignment is optimized for the best PSF, and the window is rotated by a slight angle around the vertical axis. Then, using a caliper, the corner distances between the objective and window plates are measured. The variations compared to the "best" position allow the angle calculation for both tilted PSFs. The smallest increment of the caliper is 0.05 mm. Thus, an error of ± 0.025 mm enters the angle calculation. The tilted angles and the corresponding aberrations introduced by the window tilt are displayed in Figure 3.19. Here, the challenges of high-*NA* optics become clear. Already small angles of 3.5 mrad significantly depreciate the PSF of the optical system. Therefore, much care should be put into the alignment of the glass cell and the objective.

In conclusion, it was demonstrated that the nanopore device could be a versatile tool for characterizing a high-*NA* objective. Imaging the nanopores onto a CCD camera gives the PSF of the system. It allows the observation of aberrations, which, for

example, can stem from the misalignment of the glass window. The size of the observed PSF is slightly larger than the ideal Rayleigh limit. However, this deviation stems not from a faulty objective but from combined aberrations in the optical system or additional plasmonic light interaction effects with the material around the sub-wavelength nanopores [57]. There are two reasons for this assumption. First, the characterizations the manufacturer Special Optics performed show a diffraction-limited performance, especially at the center of the FOV (see Appendix A.2). Secondly, in the last weeks, other groups also observed a larger than expected PSF with this nanopore device, hinting at a non-ideal light field.

In summary, Table 3.3 presents the experimentally measured and the specified objective parameters in a condensed form. Ultimately, these results show that the objective is not deformed in a significant way, and HQA can go forward with the passive alignment approach.

TABLE 3.3: RESULTS OF THE OBJECTIVE CHARACTERIZATION. The measured focal length is determined by the 7 µm separation of the two nanopores on the membrane. The FOV, resolution, and angle measurements stem from the analysis in Section 3.3.3.
The parameters specified by the manufacturer are stated for completeness. The calculated values from above are included as well. For more details on the RMS and PV values, see Appendix A.2.

Experimental Results		
Feature	Result	Expected
Focal length f	(19.0 ± 0.3) mm	18.8 mm
Resolution r_{min}	(704 ± 31) nm	637 nm
FOV, where $r < 110\,\% \, r_{\text{min}}$	± 104 µm	± 100 µm
Mean resolution $\bar{r}$ across the FOV	(757 ± 5) nm	637 nm
Angle α between mechanical and optical axis	(2.2 ± 1.6) mrad	0 mrad

Specified and Calculated Parameters	
Feature	Specification
Numerical Aperture *NA*	0.655
Output Aperture *D*	24.8 mm
Working Distance *WD*	13.73 mm
Back Focal Plane *WD*	1.9 mm
FOV 532 nm	± 110 µm
FOV 671 nm	± 100 µm
FOV 1094 nm	± 130 µm
Min. Tweezer Waist $2\omega_0$, $\lambda = [532, 671, 1064]$ nm	[0.51, 0.65, 1.02] µm
Min. Rayleigh Range $2z_R$, $\lambda = [532, 671, 1064]$ nm	[0.77, 0.98, 1.55] µm
On Axis RMS	$0.048\,\lambda$
On Axis PV	$0.360\,\lambda$
Average Transmission T for $\lambda \in (532, 1064)$ nm	$> 80\,\%$

4 Towards High Experimental Cycle Rates

This chapter is about the trapping and cooling of ^{6}Li atoms in an improved and accelerated way. First, an increased experimental cycle rate will be motivated. Then, the optical dipole trapping of neutral atoms will be theoretically introduced. A typical experimental cycle is described, and a new proposal for an accelerated transfer into a microtrap using a blue-detuned ring trap to compress trapped atoms is discussed. Thereby, the thermal scattering rate will be increased, which could be used to increase the cycle rate significantly. A numerical simulation of the idea follows this, and finally, two possibilities of implementing the ring beam in an optical setup are explored.

Quantum simulation is performed not with isolated experimental cycles but with many combined experimental ones. A single experimental cycle or simulation run can be considered a single realization and measurement of a complex quantum mechanical state, e.g., a ^{6}Li few-particle system. Such a system is studied by preparing an atomic sample and the subsequent quantum state readout. This incorporates recording an image, either by fluorescence or absorption imaging. Both imaging schemes are destructive methods, so the quantum state is destroyed during the readout process [27]. Thus, a new sample state must be assembled after the quantum state readout. The time it takes for an atomic sample to be prepared, manipulated, and imaged, such that a new sample can undergo the same procedure, is then the experimental cycle time.

Generally, multiple cycles will be needed to measure the physical properties of few-atom states. For example, consider a system consisting of six atoms. Compared to a system with many thousand atoms, averaging over many recordings is required to observe inherent properties such as the density distribution.

4.1 Motivation

This chapter motivates an increased experimental cycle rate with three examples. First, consider the measurement of the dynamic properties of an atom sample. Since a single image of such an atom sample is only a snapshot in time, it gives no significant insight into the dynamic behavior of the atoms. For example, multiple snapshots must be taken to measure the parameter space of an oscillating sample in a

harmonic trap at different times. The interaction of the measurement process with the quantum state, e.g., by the imaging laser, and the subsequent quantum state destruction make additional sample preparations and measurements necessary. A repeatable experimental cycle consequently enables scientific research in general but also the study of the dynamics of quantum systems, which has been achieved in current experiments, and compelling results have been produced [58, 59].

In the future, HQA will aim for further research in this direction, for example, towards higher-order effects like pair-pair correlations. However, the number of required datasets for such higher-order correlation functions grows exponentially [27]. This directly increases the required number of experimental runs. The time to obtain significant results scales strongly with the time of a single experimental run. A higher cycle rate consequently increases the gain in knowledge in a fixed period. Additionally, it enables the recording of larger datasets, which is not yet achieved due to technical limitations like the long-term stability of optics. A crucial goal of the HQA experiment is faster loading and preparation of fermionic samples.

Secondly, an increased cycle rate also improves the everyday work with the experiment in the lab. Most of the time, optimal experimental parameters are only achieved through iterative testing and gradually approaching the desired performances. Finding the correct settings for laser frequencies or aligning optics by adjusting mirror mounts by hand are just a few examples. The atom samples are often the best indicator to discern whether adjustments are working. Measuring the effects of changes directly on the atoms can provide insightful feedback. A more frequent quantum state readout will enable a faster way to find the optimal experiment parameters. For example, take the frame rate of a digital magnifier, which is used for soldering a circuit board. Imagine the difficulty of seeing the tip of the soldering iron only once every few seconds.

Thirdly, one could skip this human feedback loop and utilize this for an automated control system. Many important experimental parameters can already be controlled digitally. Thus, one could supply a program with this limited parameter space and perform algorithms inspired by machine learning routines. They could then carefully optimize values like laser frequencies or beam powers for the best results, such as the atom number in the 3D-MOT. Approaches like this have already demonstrated a significant improvement compared to conventional methods [60]. A higher cycle and feedback rate will undoubtedly increase the viability of such algorithms, as they will benefit significantly from faster measurements.

To increase the cycle rate of HQA, an improved atom sample preparation in the glass cell will be required. This preparation is mainly achieved by manipulating atomic states with laser beams. Consequently, it is essential to understand how the interactions between electromagnetic radiation and the neutral ^{6}Li atoms works.

4.2 Atom-Light Interaction

Chapter 2 introduced the various advantages the fermionic ^{6}Li isotope yields for a quantum simulator. Studying its quantum behavior is the primary goal of the HQA experiment and requires precise knowledge of its physical properties. Particularly the interaction with electromagnetic radiation is of great influence since the atoms will mostly be trapped and manipulated by laser beams.

4.2.1 ^{6}Li MOT Transitions

Figure 4.1 shows the atomic level scheme of ^{6}Li, including the significant electronic transitions used in the experiment and the hyperfine structure of the ground and excited states. The ground state $2\,^2S_{1/2}$ is shown with the electronic transitions to the excited states $2\,^2P_{1/2}$ and $2\,^2P_{3/2}$. Together, they form the well-known D1- and D2-line pair, respectively. In the 2D- and 3D-MOT, the D2-line traps the atoms and cools them to low temperatures. The laser used for this cooling is tuned to the $F = 3/2$ hyperfine splitting of the ground state. However, since the hyperfine splitting of the excited state cannot be resolved, the transition to the $F = 1/2$ ground state is allowed. Thus, the excited ^{6}Li atoms can decay with a finite probability into the $F = 1/2$ hyperfine state. However, these atoms are not visible for the cooler beam since the laser linewidth is much smaller than the hyperfine splitting of the ground state [61]. Therefore, a second beam with a smaller wavelength is required to cool these atoms efficiently. This laser light is named *Repumper*.

4.2.2 Semiclassical Dipole Interaction

The following section provides intuition on how ^{6}Li atoms are trapped with off-resonant laser light. The derivation of the fundamental theory is based on [63] and [64]. The goal is to calculate the potential energy and the interaction force that lithium atoms experience when they interact with laser light, which is far-detuned from the D-lines of lithium. For a small detuning, interactions with the D1 and D2 transitions enter the interaction potential with weighting factors. Due to the large detuning from both D-lines, U_{dip} can be approximated with a single weighting factor of unity for either transition.

The lithium atoms will be assumed as quantum mechanical two-level atoms with a ground state $2\,^2S_{1/2}$ and excited state $2\,^2P_{3/2}$. Furthermore, the electric field is assumed to be a classical field inducing an atomic dipole moment $\vec{d}$, which describes the average non-localized position $\vec{x}$ of an elastically bound electron with charge e. With the classical electric field $\vec{E}(\vec{r})$ at position $\vec{r}$

$$\vec{E}(\vec{r}) = \hat{\varepsilon} E_0(\vec{r}) e^{-i\omega t} + c.c. \tag{4.1}$$

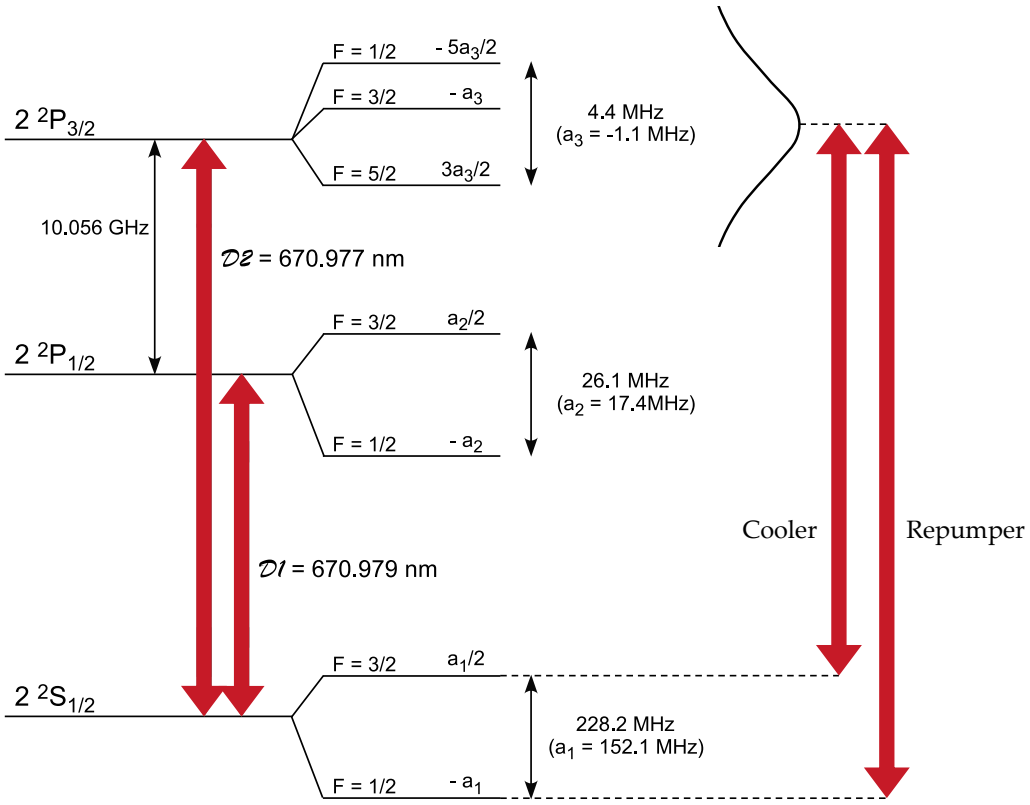

FIGURE 4.1: ^{6}LI LEVEL SCHEME WITH MOT COOLER AND REPUMPER. At the maximum, the separation between the $2\,^2P_{3/2}$ hyperfine states is only 4.4 MHz, which is smaller than the linewidth of the laser-driven transitions. Therefore, all three states will be occupied. Note that the given energies are not to scale. The figure is adapted from [62].

and the unit polarization vector $\hat{\varepsilon}$, the dipole moment can also be expressed in terms of the complex polarizability $\alpha(\omega)$

$$\vec{d} = -e\vec{x} = \alpha(\omega)\vec{E}. \tag{4.2}$$

The intensity of the electric field at $\vec{r}$ is given by

$$I(\vec{r}) = 2\epsilon_0 c|\vec{E}(\vec{r})|^2, \tag{4.3}$$

which allows the formulation of the interaction potential U_{dip} between the induced dipole and driving electrical field

$$U_{\text{dip}} = -\frac{1}{2}\langle\vec{d}\vec{E}\rangle = -\frac{1}{2\epsilon_0 c}\text{Re}(\alpha)I(\vec{r}). \tag{4.4}$$

It depends on the electric field intensity $I(\vec{r})$, which can be derived from the laser

beam intensity in the optical trap. The time average $\langle\cdot\rangle$ eliminates the rapidly oscillating terms.

The force acting on the atom can be derived from the potential energy via the gradient

$$\vec{F}_{\text{dip}} = -\nabla U_{\text{dip}}. \tag{4.5}$$

As the electrical field induces a periodic valence electron motion, the system behaves like a driven and damped harmonic oscillator. This atom model is named the *Lorentz model*. The equation of motion is then simply

$$\ddot{\vec{x}} + \Gamma_\omega \dot{\vec{x}} + \omega_0^2 \vec{x} = -\hat{\epsilon} e E_0 e^{-i\omega t}. \tag{4.6}$$

The damping of the oscillator is given by the classical damping rate Γ_ω due to radiative energy loss, which describes the dipole radiation emitted by the oscillating electron. Larmor's formula for the radiated power yields the damping rate

$$\Gamma_\omega = \frac{e^2\omega^2}{6\pi\epsilon_0 m_e c^3}. \tag{4.7}$$

This classical approach is a well-working approximation for the D-line transition of ^{6}Li with frequency ω_0. A more precise solution, however, would be the damping rate determined by the dipole matrix element of the two-level transition.

To incorporate the detuning dependency, Γ_ω is replaced with the on-resonance damping rate $\Gamma = (\omega_0/\omega)^2\,\Gamma_\omega$. With this, the equation of motion 4.6 can be solved with an assumed solution of the form $\vec{x}(t) = x_0 e^{-i\omega t}$. Plugging the obtained solution into Eqn. 4.2 yields the polarizability $\alpha(\omega)$, which describes how easily the electric field drives the atom harmonic oscillator,

$$\alpha(\omega) = \frac{e^2/m_e}{\omega_0^2 - \omega^2 - i\omega\Gamma_\omega} = 6\pi\epsilon_0 c^3 \frac{\Gamma/\omega_0^2}{\omega_0^2 - \omega^2 - i(\omega^3/\omega_0^2)\Gamma}\,. \tag{4.8}$$

Taking the real part of this polarizability and putting it into 4.4 finally results in the interaction potential between the atom and the electric field

$$U_{\text{dip}}(\vec{r}) = -\frac{3\pi c^2}{2\omega_0^3}\left(\frac{\Gamma}{\omega_0-\omega} + \frac{\Gamma}{\omega_0+\omega}\right) I(\vec{r}) \approx -\frac{3\pi c^2}{2\omega_0^3}\frac{\Gamma}{\Delta} I(\vec{r}) \tag{4.9}$$

and the photon scattering rate for photon absorption and successive spontaneous reemission events

$$\Gamma_{\text{sc}} = \frac{3\pi c^2}{2\hbar\omega_0^3}\left(\frac{\omega}{\omega_0}\right)^3\left(\frac{\Gamma}{\omega_0-\omega} + \frac{\Gamma}{\omega_0+\omega}\right)^2 I(\vec{r}) \approx \frac{3\pi c^2}{2\hbar\omega_0^3}\left(\frac{\Gamma}{\Delta}\right)^2 I(\vec{r}) \tag{4.10}$$

in the case of a large detuning $\Delta = \omega_0 - \omega$ between the laser ω and the atomic transition ω_0.

Concluding from these final equations, the force by a laser beam onto a ^{6}Li atom can be increased by either choosing a smaller detuning Δ to the lithium D-lines or

using a laser beam with a higher power, resulting in a higher local intensity $I(\vec{r})$. On the other hand, the photon scattering rate Γ_{sc} depends on the detuning with Δ^{-2} and decreases more strongly with the detuning than the interaction potential. Consequently, if the photon scattering rate leads to unwanted atom losses, the detuning of the laser light can be increased. The trapping strength then must be compensated with larger power. For instance, to mitigate off-resonant scattering losses in a tight tweezer, the existing experiments use far-detuned 1064 nm light with a large laser power of 1 W [27].

The results from the derivation above are essential to keep in mind for the following sections. As an improved transfer of atoms from the 3D-MOT into a tight micro trap is explored, the laser power and wavelength are essential parameters influencing the choice of procedure.

4.3 The Experiment Cycle

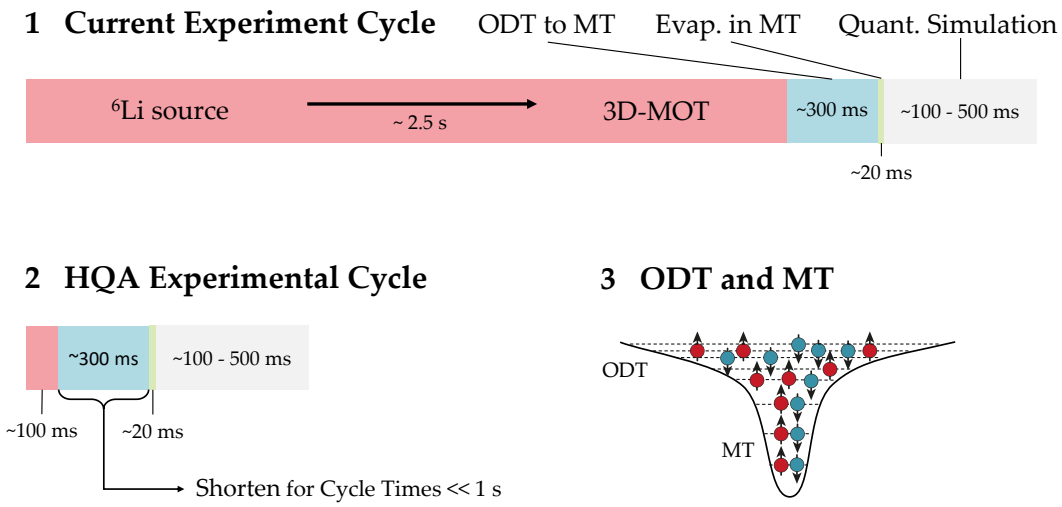

FIGURE 4.2: ILLUSTRATION OF THE EXPERIMENTAL CYCLE IMPROVEMENT.
1: An illustration of the experimental cycle in the current experiments in our group. After the atoms are trapped using a 3D-MOT, an optical dipole trap (ODT) is switched on, and a first evaporation step cools the atoms to a temperature at which they can thermalize into a micro trap (MT). The MT is activated after the ODT. This 300 ms process is colored in blue.
2: The planned experimental cycle of HQA is significantly reduced compared to the current cycle. The 3D-MOT loading is colored red and will be improved by larger laser beams and more laser power. The transfer from the ODT into the MT is marked blue and remains the longest part of the cycle. HQA aims to further increase cycle rates by shortening this transfer.
3: An illustration of the optical dipole trap and the micro trap, in which few-particle systems are prepared.

Figure 4.2 illustrates the experiment cycle for the experiments in our group and the expected cycle for the HQA. For now, the final atom sample after the preparation is assumed to be the same for both. In both cycles, the atoms are transferred from an oven reservoir to the 3D-MOT confinement. To put the atoms in an environment allowing evaporative cooling, an ODT is switched on. Such a trap could, for example, be a crossed-beam ODT [27]. Lowering the optical potential depth at this point allows the evaporation of the hottest atoms. With a consequent rethermalization, a cold sample is obtained, which, subsequently, can be transferred into an ultra-tight tweezer, the micro trap (MT). This process currently takes about 300 ms.

A final evaporation step in the MT takes roughly 20 ms and leads to an ultracold degenerate atom sample. After reaching the desired quantum state for a given sequence, the actual quantum simulation takes place. An imaging procedure concludes the cycle.

The beginning of this chapter motivated fast experimental cycles. To this end, HQA already took a big step in this direction. The current experiments in our group use a Zeeman slower, which slows the atoms from an oven so that they can be captured in a 3D-MOT. In HQA, however, the 2D-MOT takes the role of pre-cooling the atoms. Large beams and a Toptica TA-SHG Pro laser with high power (1 W at 671 nm) distributed among the 2D-MOT and 3D-MOT beams will enable a loading rate of 10^9 Hz. For a 3D-MOT, which provides enough atoms for evaporative cooling and mesoscopic atomic samples, a number of 10^8 atoms is needed [27]. Therefore, a MOT loading time of roughly 100 ms will be needed.

The transfer of atoms from the oven reservoir to a 3D-MOT accelerated the experimental time significantly, as shown in Figure 4.2. However, HQA aims to increase the cycle rate even further. The most significant remaining point for improvement in the cycle is the transfer from an ODT into the MT.

Transfer into the Micro Trap

A combination of two laser traps currently performs the transfer of atoms from the 3D-MOT cloud into an ultracold regime (see to the bottom right in Figure 4.2). However, the atoms from the 3D-MOT are too hot to stay in the MT and must be cooled down. To this end, an intermediate ODT is switched on, and its optical potential is lowered gradually, which causes evaporation. Thus, the temperature decreases enough that atoms can thermalize into the MT, located within the ODT, and switched on when the required temperature is reached. This transfer takes roughly 300 ms and will be the point of interest for the following proposal of a new transfer. However, first, some theoretical background on evaporative cooling is needed.

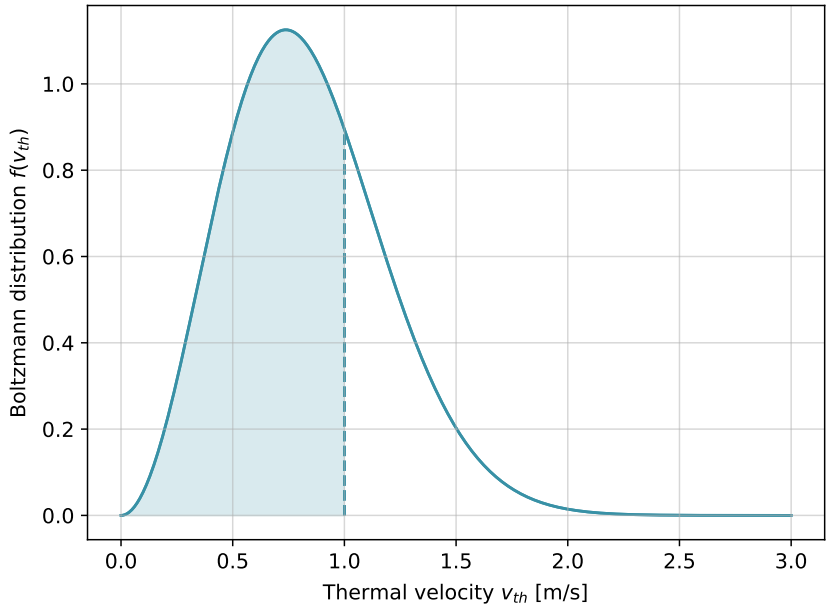

FIGURE 4.3: EXAMPLE OF A TRUNCATED BOLTZMANN DISTRIBUTION The distribution is plotted at a temperature of $T = 0.2\,\mathrm{mK}$. It depicts the evaporation of trapped atoms with the thermal velocity $v_{\mathrm{th}} > v_{\mathrm{cut}} = 1\,\mathrm{m/s} = \sqrt{2kT_{\mathrm{cut}}/m}$. The cut-off energy is $U_{\mathrm{dip}} = mv_{\mathrm{cut}}^2/2 = 5 \times 10^{-27}\,\mathrm{J}$, which corresponds to 0.36 mK.

Evaporative Cooling

Evaporative cooling is the last cooling stage enabling ultracold atom experiments to reach temperatures as low as a few nanokelvins [65]. The concept behind evaporative cooling can be pictured with a hot cup of coffee located in the open air. The highest energy molecules in the liquid leave the cup as warm steam. Their energy is higher than the coffee's average molecule temperature, and the remaining liquid's total average temperature is reduced.

In a quantum simulator, however, the evaporation is realized with atoms in an optical dipole trap, which has a trap depth U_{dip} determined by the "height" of its potential walls. Only atoms with a thermal energy E larger than the optical potential can escape the trap. The evaporation procedure then gradually lowers the potential walls such that the atoms with the highest energy leave the system. Provided interatomic interactions are allowed, and atoms can thermalize, the remaining ensemble of atoms reaches a lower average temperature T. The following section utilizes the well-known Boltzmann distribution for a mathematical description of the evaporation process. It describes the distribution of thermal energy across an atomic sample in equilibrium. An example is plotted in Figure 4.3.

The following calculations are based on [66]. The thermal kinetic energy of a single atom is given by $E = \frac{1}{2}mv_{\mathrm{th}}$, with the atom mass m and its thermal velocity v_{th}. The Boltzmann distribution with the temperature T gives the probability of a

state with certain E to be occupied

$$f(E,T) = 2\sqrt{\frac{E}{\pi}}\left(\frac{1}{kT}\right)^{3/2} \cdot e^{-E/kT}, \tag{4.11}$$

which is depicted as an example in Figure 4.3. The integral over all energies is unity, and multiplying it with the number of atoms gives the number of atoms occupying the states considered by the integral limits. An integral from 0 to ∞, therefore, gives the initial number N_0 again

$$N_0 \int_0^\infty f(E,T_0)dE = N_0. \tag{4.12}$$

The optical interaction potential $U_{\mathrm{dip}}(I)$ between the atom and the electric field depends on the laser intensity I. It sets the limit for the energy of atoms that can pass the trap potential walls. This cut-off energy is given by 4.9 and can also be expressed as temperature via

$$T_{\mathrm{cut}} = U_{\mathrm{dip}}(I)/k. \tag{4.13}$$

The truncation of the integral yields a new distribution in non-equilibrium. Then, rethermalization occurs, the energy is redistributed, and high energy states are repopulated. The remaining atom number N_1 in terms of the initial number and the cut-off energy U_{dip} is

$$N_1 = N_0 \int_0^{U_{\mathrm{dip}}} f(E,T_0)dE = N_1 \int_0^\infty f(E,T_1)dE. \tag{4.14}$$

During this, the mean temperature decreases since the evaporated atoms carry energy higher than the initial mean thermal energy.

The new temperature after rethermalization T_1 can be expressed as a function of the cut-off energy 4.13 and the initial temperature T_0,

$$T_1 = \frac{2}{3k}\frac{\int_0^{U_{\mathrm{dip}}} E^{3/2}e^{-E/kT_0}dE}{\int_0^{U_{\mathrm{dip}}} E^{1/2}e^{-E/kT_0}dE}. \tag{4.15}$$

By solving the integrals T_1 becomes

$$T_1 = \frac{T_0}{3}\left\{\frac{3\sqrt{\pi}\,\mathrm{erf}(\sqrt{T_c/T_0}) - [6\sqrt{T_c/T_0} + 4(T_c/T_0)^{3/2}]e^{-T_c/T_0}}{\sqrt{\pi}\,\mathrm{erf}(\sqrt{T_c/T_0}) - 2\sqrt{T_c/T_0}e^{-T_c/T_0}}\right\}. \tag{4.16}$$

When no external energy is added to the system, the new temperature is lower than before evaporation $T_1 < T_0$. Since the new MT transfer proposal includes evaporative cooling, these formulas will become practical in the numerical simulation later.

4.3.1 The Push Broom Proposal

A reduced experimental cycle time can be achieved by accelerating the transfer of the atoms from the 3D-MOT into a small micro trap (MT). Then, evaporative cooling can cool the atoms into the ultracold degenerate fermi gas regime. The MT is a tight tweezer with a nearly harmonic attractive conservative potential. Atoms from the 3D-MOT reservoir occupy certain energy states, which are given by the Boltzmann distribution, of which the 3D-MOT determines parameters like temperature or density.

The probability of an atom being trapped by the MT depends on the rate of interatomic collisions. On average, the atoms have an energy E corresponding to their thermal velocity $v_{\mathrm{th}} = \sqrt{2kT/m}$. Whenever an atom randomly passes the attractive MT potential valley, it gains some energy while entering and loses the same energy while leaving the MT. Since these two energy changes are equal, the atom is not trapped yet. Only if the atom collides with another atom and transfers its energy is the atom trapped in the potential. This collision is an interatomic *scattering event*, which occurs with the *thermal scattering rate* Γ_{th}. The ^{6}Li atoms will be assumed to behave like an ideal classical gas with elastic collisions during this chapter. However, quantum physics needs to be considered in a real system, e.g., by including that two fermions in the same spin state cannot scatter.

The existing experiments perform the transfer from the 3D-MOT into the MT with an intermediate ODT. Evaporation in this trap lowers the temperature enough such that atoms can thermalize into the MT. Here, the Push Broom proposal comes into play. The MT loading time is roughly 300 ms, mainly limited by a thermal scattering rate of 2.8 kHz at an atom density of 0.1 $\mu\mathrm{m}^{-3}$. After hot atoms are evaporated, the ^{6}Li gas forms a new Boltzmann distribution and goes into thermal equilibrium again. This energy redistribution happens faster if atoms collide with each other more often. For a non-equilibrium system to rethermalize, it takes about 2.7 scattering events [67]. An enhanced thermal scattering rate accelerates the evaporation time needed to reach the low temperature required for MT loading. Additionally, if the thermal scattering rate and the local density are increased, the atoms pass the MT potential more often, and the required scattering events happen more often. Hence, the goal of the Push Broom proposal is a large scattering rate Γ_{th}, which enables an accelerated MT loading and a reduced overall cycle time.

The semiclassical thermalization scattering rate Γ_{th} will be assumed for elastic scattering

$$\Gamma_{\mathrm{th}} = v_{\mathrm{th}} \cdot \sigma_{\mathrm{sc}} \cdot \rho = \sqrt{\frac{2kT}{m}} \cdot 4\pi \left(\frac{h}{\sqrt{2\pi m k T}} \right)^2 \cdot \rho \tag{4.17}$$

with the mean thermal velocity v_{th}, which is the most probable velocity at the peak of the Boltzmann distribution, the scattering cross-section σ_{sc}, and the De Broglie wavelength λ_{db}, given by the temperature T. The interaction between the atoms is assumed such that the cross-section is determined by λ_{db}. This interaction can be realized by tuning the magnetic field and thereby the Feshbach resonance. Specifically,

the contributions to Γ_{th} are

$$v_{\text{th}} = \sqrt{\frac{2kT}{m}}, \quad \sigma_{\text{sc}} = 4\pi\lambda_{\text{db}}^2 \quad \text{and} \quad \lambda_{\text{db}} = \frac{h}{\sqrt{2\pi mkT}}. \tag{4.18}$$

The constant components are the atomic mass m, the Boltzmann constant k, and the Planck constant h. Equation 4.17 yields the following proportionalities

$$\Gamma_{\text{th}} \propto \frac{1}{\sqrt{T}} \text{ and } \Gamma_{\text{th}} \propto \rho\,. \tag{4.19}$$

Thus, the local density needs to be enhanced to obtain an increased scattering rate.

To achieve this, an optical potential is required, which locally compresses the ^{6}Li cloud. The dipole interaction introduced in Section 4.2.2 describes how laser light exerts a force onto the atoms. Therefore, a laser trap can be used to compress the atoms and increase the local density. Since the goal is the thermalization into a tight tweezer, the trap should be radially symmetric such that the compression happens towards a center point, which overlaps with the tweezer. However, the experimental realization of a spherical laser trap is hard to realize. Therefore, this proposal limits the compression to two dimensions. In that case, a ring trap with a tunable radius will compress the atom cloud, the thermal scattering rate should increase, and the transfer into the MT is accelerated. A vertical compression, e.g., by two light sheets, could also be implemented if this proposal should be developed further.

The atoms will interact with the laser light differently depending on the wavelength of this trap. As discussed, photon scattering events described by 4.10 lead to atom losses in the trap. However, this can be minimized using laser light with a frequency far-detuned to the ^{6}Li D-line transitions at 671 nm. Choosing blue-detuned laser light for this with a wavelength $\lambda = 532\,\text{nm}$ has two advantages, in contrast to red-detuned light. First, the dipole interaction with red-detuned light is attractive, while blue-detuned light is repulsive. Thus, inside a blue-detuned ring trap, the atoms see no light. They only experience a repulsive force at the potential walls. Then, light-induced scattering events can only happen at the walls and not inside the trap.

Secondly, compared to a red-detuned trap, this wavelength allows for smaller optical features, as the optical resolution increases with smaller wavelengths, see Section 3.3.1. A smaller laser beam size will allow for a higher field intensity than a larger beam with the same power. Therefore, the energy of the atoms, which can be captured, increases, and fewer atoms will be lost.

While the real space density increases during the compression of a gas, the phase space density will not rise without evaporation. To describe the change of the temperature during compression, the ^{6}Li cloud will be assumed as an ideal monoatomic gas. Therefore, the ring trap compression is simply the adiabatic compression of an

ideal gas. This includes a temperature increase $\Delta T = T_2 - T_1$, which is given by

$$T_2 = T_1 \left(\frac{V_1}{V_2} \right)^{\kappa - 1}, \tag{4.20}$$

with the gas volume before V_1 and after V_2 the compression [68]. For an ideal monoatomic gas, the adiabatic index is $\kappa = 5/3$. The real trap depth, however, is finite, and atoms with high thermal energy will be lost. The evaporation of atoms during the compression is, therefore, not negligible. While the atomic gas temperature T increases during the compression, the ring trap also shrinks in size. It follows that the laser power is distributed over a smaller area. Thus, the trap depth grows, and higher energy atoms can be trapped. Two thermal effects are at counterplay here. While the temperature increases during the compression, it also decreases due to evaporation beyond the ring walls, which depends on the trap depth $U(I)$.

This ring trap could accelerate the transfer from the 3D-MOT. By quickly evaporating the hottest atoms, the evaporation step is combined with an increased thermal scattering rate such that the atoms thermalize quickly into the MT. Next, it is studied how the initial parameters influence this procedure and whether it can work experimentally. To this end, a numerical simulation of the Push Broom compression is performed.

4.4 Adiabatic Simulation

A high scattering rate and high local density accelerate the transfer of ^{6}Li into the ODT. A numerical simulation of the physical quantities during this compression might reveal whether the Push Broom proposal is worth pursuing experimentally. The most important parameters characterizing the procedure are the ring trap radius r, the trap depth U, the gas temperature T, the local density ρ, the number of atoms in the trap N, and the interatomic thermal scattering rate Γ_{th}. Each of these parameters will change with a more strongly compressed ring trap. First, the properties of such a trap will be discussed.

4.4.1 Ring Trap

As mentioned above, a shrinking ring trap will perform the local compression. During this, the simulation assumes constant confinement in the direction normal to the ring area, i.e., the z-direction. The height of this confinement is $h = 10\,\mu\text{m}$, which, for example, could be realized with two blue-detuned or a single, red-detuned light sheet. The compression, therefore, is accomplished by decreasing the radius r of the ring trap. The characteristic properties of this ring are inspired by an experimental realization of such an optical potential [69]. Here, a ring with a thickness of roughly $d = 5\,\mu\text{m}$ was achieved with steep potential walls. As a simplification, the ring in the

simulation is assumed to be at a uniform height, essentially a box potential with infinitely steep walls. However, the height of this wall increases for smaller radii since laser power is distributed across a smaller ring area. An initial radius of $r_0 = 50\,\mu\text{m}$ should include most atoms from the 3D-MOT cloud and a final radius $r_{\text{final}} = 5\,\mu\text{m}$ is in the order of magnitude of a tight MT tweezer.

The laser power P determines the intensity of laser light in the ring. It depends on the inner ring radius r via

$$I(r) = \frac{P}{\pi((r+d)^2 - r^2)}\,, \tag{4.21}$$

with a constant ring thickness d and the ring area in the denominator. This intensity determines the trap depth $U(I)$, which is given by Eq. 4.9. Therefore, the laser power is crucial for the number of atoms captured by the ring trap. The ring potential walls confine only atoms with an energy $E < U(I)$. Since the Boltzmann distribution gives the energy distribution across all atoms in equilibrium, atoms with energy lower and higher than the trap depth exist. Like during the MT's final evaporation, atoms with $E > U(I)$ can pass over the ring potential. They are "evaporated" from the ring. If more power is sent into the ring, the potential walls will be higher, and as $U(I)$ increases, more atoms will be captured.

The order of magnitude for the required power changes with the detuning since $U(I) \propto \Delta^{-1}$. The simulation shows that a blue-detuned trap light $\lambda = 532\,\text{nm}$ requires roughly $3 - 5\,\text{W}$ for a reasonable number of atoms. In comparison, only $200 - 500\,\text{mW}$ are required for a close detuning of 660 nm. For the following analysis, the laser light will be assumed with a wavelength of 532 nm. Higher powers are often conveniently available for this light by frequency-doubling a 1064 nm laser source. Despite this, the simulation and the Push Broom proposal work with far and closely blue-detuned light.

4.4.2 Simulation

First, a set of starting parameters must be determined. An overview of the initial values in the simulation is given in Table 4.1. Inspired by 3D-MOT values of the running experiments, the simulation assumes an initial temperature $T_0 = 1\,\text{mK}$ and atom density $\rho_0 = 0.10\,\mu\text{m}^{-3}$. The spatial distribution of atoms is assumed to be uniform. With the confinement parameters from above, a cylindric sheet with height $h = 10\,\mu\text{m}$ and radius $r_0 = 50\,\mu\text{m}$ is taken from the 3D-MOT distribution with a density $\rho_0 = 0.10\,\mu\text{m}^{-1}$. These assumptions result in an initial atom number of roughly $N_0 = 8000$. As a comparison, current experiments start with roughly 10^6 atoms in the large ODT. Consequently, if more atom numbers should be desired, one must pursue either a larger ring or an additional compression along the z-axis. Note that atom numbers during this simulation should be considered rough approximations. The actual value in the lab will depend on many other experimental parameters, like the oven temperature or the MOT loading rate.

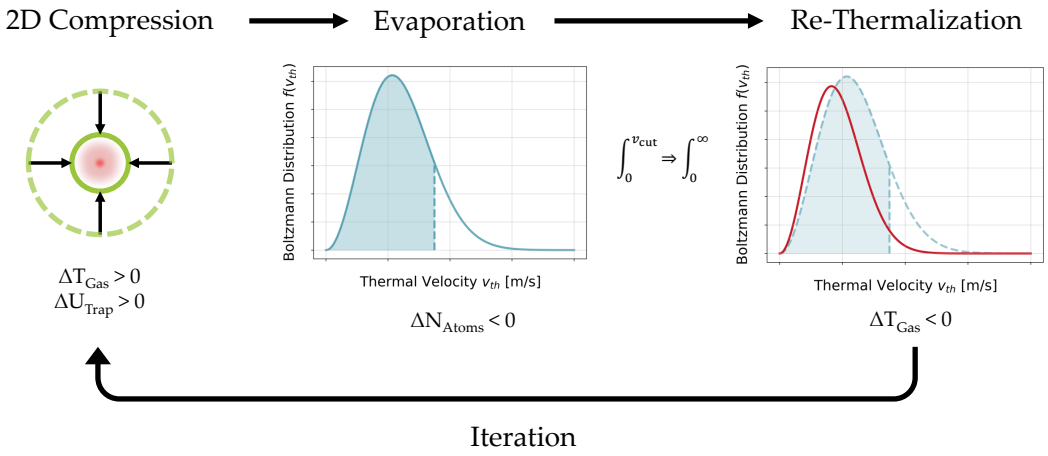

FIGURE 4.4: DEPICTION OF THE SIMULATED STEPS IN EACH ITERATION. In the first step, the ring shrinks and compresses the ideal gas. This leads to a temperature and trap depth increase. The Boltzmann distribution gets truncated in the second step due to high-energy atoms escaping the ring potential walls. At last, a new Boltzmann distribution is formed, and thermalization yields a lower mean thermal velocity and temperature. Determined by the change of radius Δr, the next iteration repeats the steps until the final radius r_{fin} is reached.

Figure 4.4 illustrates the sequence of the simulation. Each iteration consists of the three illustrated steps. Initially, the ring trap is compressed by a change of ring radius Δr per iteration, which is determined by the number of iterations. Reducing the radius from $r_0 = 50\,\mu\text{m}$ to $r_{\text{fin}} = 5\,\mu\text{m}$ and setting 5000 iterations results in $\Delta r = 9\,\text{nm}$. The number of iterations was chosen so that the compression runs adiabatically, simulating slow compression, evaporation, and rethermalization at each iteration. Rethermalization occurs when the new system, missing the evaporated atoms, settles into equilibrium again. In each iteration, a wait time is assumed, such that a new temperature has settled in. This temperature is given by Eqn. 4.16. The wait time depends mostly on the inter-atomic scattering events since thermal collisions lead to a redistribution of thermal velocities. Then, the next iteration continues with a smaller ring.

For the concluding analysis, the total time t_{tot} of the entire compression procedure can be estimated. Each iteration is assumed such that the gas rethermalizes. The rethermalization of trapped atoms during evaporation takes 2.7 scattering events [67]. The wait time t_{it} during this step is then determined by the interatomic scattering events with the thermal scattering rate $\Gamma_{\text{th}}(r)$ depending on the local density, which increases for smaller radii r

$$t_{\text{it}} = \frac{2.7}{\Gamma_{\text{th}}(r)} \,. \tag{4.22}$$

TABLE 4.1: INITIAL PARAMETERS AND THE SIMULATED FINAL RESULTS
Two simulations with a different number of iterations are performed. The adiabatic compression with thermalization at each iteration takes a long 36 s, determined by 2.7 scattering events per iteration. Therefore, the total time t_{tot} decreases with fewer iterations. At 30 iterations, t_{tot} becomes 267 ms. Note that the atom numbers are a numeric approximation of a real world scenario.

Starting Parameters					
Power P	Density ρ_0	T_0	Radius r_0	Iterations	
3 W	0.10 µm^{-3}	1 mK	50 µm	5000, 30	
Results for 5000 Iterations and $\Delta r = 9$ nm (Figures)					
Atoms N_{fin}	Density ρ_{fin}	T_{fin}	Trap Depth U_{fin}	Sc. Rate $\Gamma_{th,\,fin}$	t_{tot}
111	0.14 µm^{-3}	0.08 mK	0.79 mK	5.4 kHz	36 s
Results for 30 Iterations and $\Delta r = 1552$ nm					
Atoms N_{fin}	Density ρ_{fin}	T_{fin}	Trap Depth U_{fin}	Sc. Rate $\Gamma_{th,\,fin}$	t_{tot}
216	0.14 µm^{-3}	0.17 mK	0.79 mK	3.6 kHz	267 ms

The total time of the simulated compression process becomes the sum over all iterations

$$t_{tot} = \sum t_{it} \,. \tag{4.23}$$

Hence, the total time scales strongly with the number of iterations and the thermal scattering rate at each ring radius.

The goal of the Push Broom proposal is the acceleration of the atom transfer, and therefore a short total time t_{tot} is desired. Herein lies the motivation of the compressing ring trap. An increased local density increases the thermal scattering rate and thus allows shorter waiting times t_{it} during each iteration. The waiting time during each iteration allows the rethermalization of the remaining atoms, resulting in lower temperatures. Consequently, the procedure should result in a quick transfer of atoms trapped in the ODT into a cooler state with a high thermal scattering rate allowing a quick thermalization into the MT. The python code of this simulation can be found in [70].

4.4.3 Results

Besides the initial values, Table 4.1 shows the final results of the simulation. Figures 4.5 and 4.6 show the simulated parameters during the compression. The ring radius is reduced from 50 µm to 5 µm, which is depicted by the inverted x-axis. Figure 4.5 shows a massive loss of atoms during the first step. About 98 % of the initial atom number is lost from the ring ODT. The reason for this is the low trap depth of roughly 0.1 mK compared to the gas temperature of 1 mK, shown to the right in Figure 4.5.

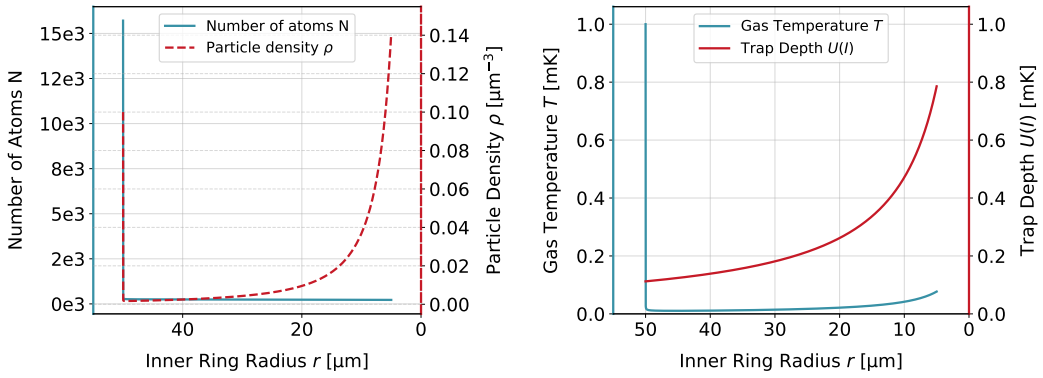

FIGURE 4.5: ATOM NUMBER, PARTICLE DENSITY, TRAP DEPTH, AND GAS TEMPERATURE IN THE SIMULATION (5000 ITERATIONS.)
The compression is illustrated by a decreasing radius from left to right.
LEFT: The blue curve shows the initial particle loss, while the red curve shows the initial density decrease. However, the compressed trap increases particle density at a small ring radius.
RIGHT: Both y-scales show the same scale. The blue curve shows the gas temperature, while the red curve depicts the trap depth. Due to the low trap at the start, many atoms are evaporated, and the temperature decreases. The trap depth increases with radius, and the gas temperature grows slightly due to the compression.

The optical potential of the ring at the start is only high enough to truncate a small tail of the first Boltzmann distribution. This is depicted to the right in Figure 4.6. In the experimental realization, this atom loss might be mitigated by a non-adiabatic ramp-up of the initial compression. This way, there would not be enough time for all atoms to evaporate. Note that the numerical simulation determines the precise number of atoms and is, therefore, only a rough approximation of an application in the lab.

On the other hand, this atom loss also has a positive effect. The atoms, which are evaporated, occupy the highest energy states in the system. After their evaporation, the system forms an equilibrium again. Thus, the remaining atoms rethermalize, form a non-truncated Boltzmann distribution, and the mean temperature of all atoms and the entire system decreases, which results in net cooling during the compression. The final temperature is $T_{\text{fin}} = 80\,\mu\text{K}$, corresponding to a reduction to 8 % of the initial temperature.

In the further course of the compression, only a negligible number of atoms is evaporated. Due to a smaller ring, the laser power is distributed over a smaller area. Thus the trapping potential grows while the temperature increases due to the compression. The trap depth grows more strongly than the temperature increase, which is visible in the right plot of Figure 4.5. At the final radius, the temperature is about 10 % of the trap depth, and only the highest energy states can escape the trap, shown by the red curve to the right in Figure 4.6.

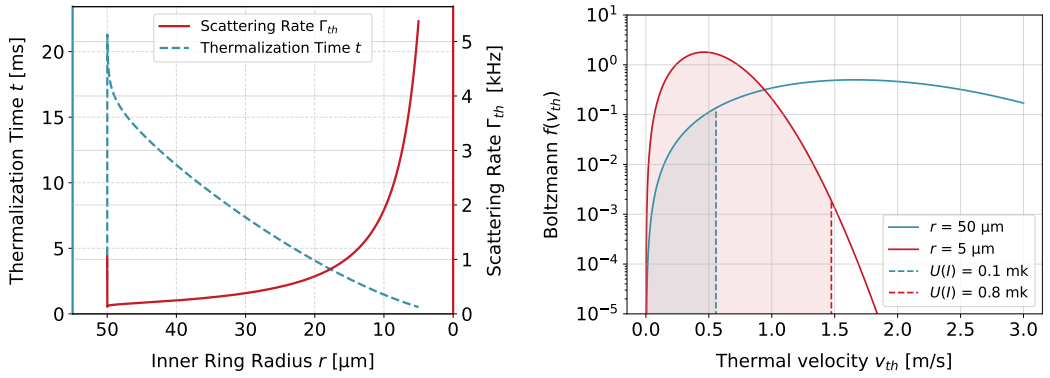

FIGURE 4.6: SCATTERING RATE, THERMALIZATION TIME, AND TRUNCATED BOLTZMANN DISTRIBUTIONS IN THE SIMULATION (5000 ITER.)
LEFT: The compression is illustrated by a decreasing radius from left to right. The red curve shows the thermal scattering rate Γ_{th}. Its inverse, scaled with roughly three scattering events, gives the thermalization time t assumed for each infinitesimal step. This time is shown as the dashed blue curve. The sum of each value in the blue curve yields the total time of the compression process t_{tot}.
RIGHT: Displayed are both the initial and final truncated Boltzmann distributions. The blue curve illustrates the substantial particle loss at the beginning, while the red curve shows a lowered sample temperature with an increased trap depth.

Scattering Rate and Thermalization Time

The left plot in Figure 4.5 also shows the ring trap's atom density. Since roughly 98 % of atoms are lost in the first step, the local density also decreases. However, due to the strong compression at smaller radii, the density grows to a final value of $\rho_{\text{fin}} = 0.14\,\mu\text{m}^{-3}$, which is similar to the initial value of $0.10\,\mu\text{m}^{-1}$ in the 3D-MOT. The temperature also decreases thanks to the evaporation of hot atoms, and with Equation 4.19, the scattering rate increases again. The final value is $\Gamma_{\text{th}} = 5.4\,\text{kHz}$, roughly two times the scattering rate $\Gamma_{\text{exp}} = 2.8\,\text{kHz}$ attained during the ODT evaporation in the existing experiments. Here, a larger scattering rate accelerates the thermalization of atoms into the MT.

However, the largest gain in cycle rate will be achieved during the evaporation process in the ODT. The Push Broom proposal can reduce the experimental cycle rate if these final scattering rates can be accomplished during a quick non-adiabatic compression with a total time $t_{\text{tot}} < 300\,\text{ms}$. Larger instantaneous compression steps can obtain an estimation of this scenario. To this end, the number of iterations must be reduced drastically. As an example, a simulation with 30 iterations was performed. The final values are shown in Table 4.1. In this case, a scattering rate of $\Gamma_{\text{th}} = 3.6\,\text{kHz} \approx 1.3 \cdot \Gamma_{\text{exp}}$ is achieved in a much shorter time $t_{\text{tot}} = 267\,\text{ms}$.

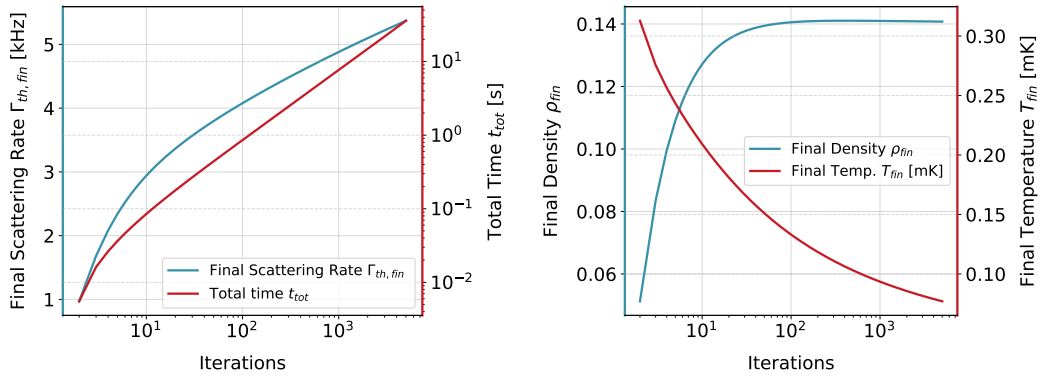

FIGURE 4.7: FINAL SIMULATION RESULTS FOR DIFFERENT ITERATIONS. A smaller number of iterations yields an intuition for fast quenches of the compressing ring trap. Note the logarithmic scaling of the x-axes.
LEFT: The total time decreases linearly with the number of iterations, while the thermal scattering rate falls rapidly for low iterations and, therefore, large compression steps. The right figure can explain this.
RIGHT: At fewer iterations, fewer atoms remain after compression. A smaller Boltzmann tail is truncated for many iterations, and more atoms can remain in the trap. Consequently, more atoms with lower thermal energy are stored in the trap, and the final temperature decreases for more iterations.

Iteration Dependency

The resulting values vary for a different number of iterations. Therefore, the simulation was performed for a different number of iterations to develop an intuition for the effect of a non-adiabatic quench. Figure 4.7 shows the different final scattering rates, temperatures, atom numbers, and total times for each simulation.

In the left plot, the total time decreases nearly linearly with the number of iterations, as the terms in the sum 4.23 decrease directly with the number of iterations. The final scattering rate $\Gamma_{\text{th, fin}}$ scales directly with the final density in the right plot. However, it decreases significantly for few iterations and, therefore, large compression steps, shown in the left half of the logarithmic x-axis.

The reason for this is the decline in the number of atoms and, consequently, the density at few iterations. At a number of iterations smaller than 10, fewer atoms remain after the compression procedure. This occurs due to the truncation of the Boltzmann distributions at smaller energies; thus, fewer atoms can remain in the trap. In contrast, at many iterations, smaller tails will be cut. Consequently, more atoms with lower thermal energy are stored in the trap, and the final temperature decreases for more iterations.

These simulations suggest that a short total time can be achieved, such that a balance between a fast compression and a favorable scattering rate with a reasonable number of atoms is found. The previously performed simulation with 30 iterations is an example of such a compromise. In the non-adiabatic limit, however, further interactions like photon-atom interactions at the laser ring must be considered. Thus,

the simulation can only provide intuition at low iterations and fast quenches. Further simulation development for fast quenches could be valuable if the Push Broom concept is integrated into the experiment. However, a study on an atomic sample would prove even more insightful.

4.5 Experimental Implementation

In the previous section, the viability of the Push Broom proposal has been shown. An enhanced scattering rate and local density can be used to accelerate the experimental cycle time. However, to implement this idea practically, several prerequisites must be met.

Creating a high-quality ring beam is essential for the Push Broom proposal. A trap with radial symmetry allows uniform compression in all spatial directions, focusing the increased density and thermal scattering rate towards the trap's center, optimizing the thermalization into the MT tweezer at this position. Further, efficiently distributing the laser power into a concentrated ring delivers a higher trap depth than a washed-out beam shape.

One way to create such a box potential beam would be a DMD [71]. However, the micromirrors in the off-position will dump most of the power required for trapping hot atoms. A more efficient optical component, albeit less flexible for the shape of the optical potential, is an axicon [72]. The axicon is an element made from glass, which, in contrast to a standard lens, transforms a Gaussian input beam with a radially constant refraction angle. The conical shape of a convex axicon creates a Bessel-like beam in the near-field and a diverging ring in the far-field. This ring beam can be collimated using an additional refractive element. A second axicon, for example, will make the ring beams parallel to the optical axis. Further, a lens focuses the ring wavefronts into a thin ring, enabling a high laser power concentration [73]. Therefore, the best setup for the Push Broom proposal is a lens-axicon combination.

The outer diameter of the ring d_r after the distance L depends on the axicon angle θ_1 and the refractive index of the axicon n via

$$d_\mathrm{r} = 2L \tan\left[(n-1)\,\theta_1\right], \tag{4.24}$$

and the ring thickness t depends on the input beam diameter D with $t = D/2$ [74]. Both parameters are shown in Figure 4.8. The Gaussian spot size then gives the thickness of the focused ring in the intermediate image plane

$$s = \frac{4}{\pi}\lambda\frac{f_1}{t}, \tag{4.25}$$

with the wavelength λ and the focal length f_1. The ring thickness $s_\mathrm{at} = s/M$ and the ring diameter $d_{\mathrm{r,\,at}} = d_\mathrm{r}/M$ in the atom plane only depend on the magnification M of the combination of the high NA objective and the lens after the objective.

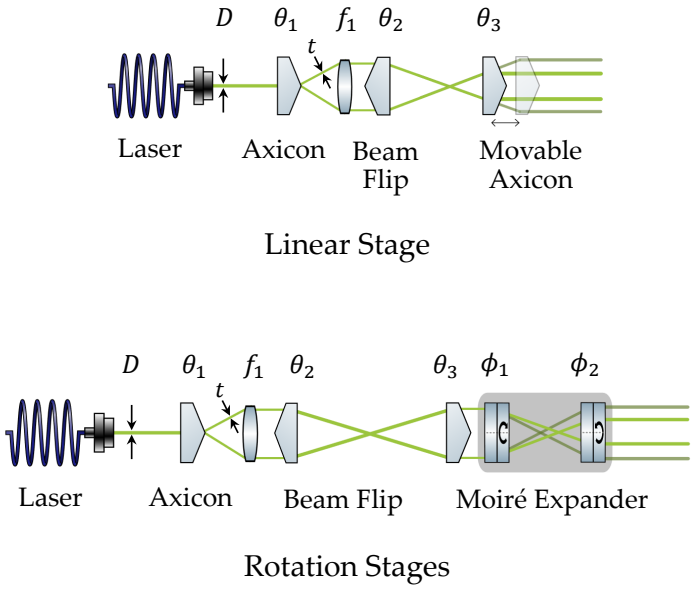

FIGURE 4.8: TWO EXPERIMENTAL SETUPS FOR A TUNABLE RING BEAM. The lens after the first axicon focuses the ring beam onto an intermediate image plane, which can be demagnified onto the atoms. Note that the distances between the optical components are not to scale and depend heavily on the axicon angles and the lens focal length. This ring beam creation is based on [69].
TOP: A linear translation stage moves the last axicon such that the diameter of the transmitted ring beam varies.
BOTTOM: Two mechanical rotation stages ϕ_1, and ϕ_2 are used to rotate two Moiré phase plates relative to each other. Together they form a tunable beam expander, which adjusts the ring beam diameter.

While axicons are commercially available with high precision, they inherently possess imperfections on the axicon tip, which ultimately lead to a softer and noisier inner ring edge and a light spot at the center of the ring [75]. Since this could lead to unwanted photon scattering, especially at the position of the MT, two additional axicons are introduced in the experimental setup. They are placed directly after the lens f_1 in Figure 4.8. Their purpose is to flip the ring beam inside out such that undesired light components inside the ring are avoided. This optical setup is based on [69]. The ring diameter can be determined using the axicon θ_1 and the lens f_1. For the Push Broom proposal, however, the ring radius still must be adjusted dynamically.

Translation Stage

Additionally to the ring beam creation, Figure 4.8 presents two ways to tune a ring beam trap dynamically. The most straightforward way of tuning the ring radius is the position of the third axicon θ_3. Depending on the angle of axicon θ_2, the output diameter changes while moving the third axicon along the optical axis. This movement could be realized using a mechanical translation stage. The mechanical

requirements for this stage, however, are rather demanding. Since the whole purpose of this procedure is to accelerate the cycle times, the mechanical translation must happen in milliseconds. With a travel distance of roughly 1 cm, an optical setup would require a high-acceleration translation stage with long-term stability, durability, and precise repeatability. Moreover, such a stage might introduce unwanted mechanical vibrations on the optical table. Therefore, another solution was examined.

Moiré Lenses

A new kind of optical element has been in development recently [76], a so-called Moiré lens. A single Moiré lens consists of two rotatable phase plates. Depending on their relative rotation, they form a radially symmetric phase profile, which resembles the diffractive pattern of a Fresnel lens with focal length f_M. Other phase patterns, such as a helical beam or a tunable axicon, are also possible [77, 78]. The tunable ring setup, however, will focus on the tunable lens.

The relative rotation ϕ between the phase plates tunes the focal length f_M. The optical power is given by

$$f_M^{-1} = \frac{4\phi\lambda}{Ds\sqrt{4\pi^2+1}}, \tag{4.26}$$

with the lens aperture D, the angle ϕ in radians, and the pixel size s on the phase plates. The Moiré lens delivers a tunable focus, which, for instance, has been used to transport ultracold atoms [79].

Combining two lenses with a tunable focal length allows the assembly of a beam expander with variable magnifying power. Using two Moiré lenses and placing each on a rotation stage would be an example of a design for an electrically tunable beam expander; compare Figure 4.8. The ratio between both Moiré focal lengths determines the beam radius. Compared to the back-and-forth movement of an axicon, the Moiré expander requires only a rotation of the phase plates. A rotation of 90° results in a change of focal length by a factor of 2. For example, a Moiré lens with a diameter of 25.4 mm and a pixel size of 8 µm can tune its focal length from 300 mm to 150 mm with a 90° rotation. Nevertheless, this focal length dependency on the angle can be adjusted with the phase plate pixel size.

Such a lens with a rotation stage could reduce the mechanical vibration on the optical tables during the ring trap compression. At the time of this thesis, Moiré lenses are not yet commercially available. In the future, however, pursuing other possible experimental applications of such devices will be worthwhile as they could simplify the digital control of refractive optics.

5 Epilogue

5.1 Conclusion

The beginning of this thesis introduced how quantum simulation can overcome the limitations of classical physics and model still unfamiliar physical systems with single atoms. Based on this motivation, an overview of the operating principle of a new quantum simulator, i.e., HQA, was given. This experiment will be able to assemble both few and many-body quantum states using ^{6}Li atoms with a focus on simplification and modularity. Furthermore, the idea of optical modules introduced a new approach to working with optical systems. Many advantages of the modular approach include, for example, the transferability between setups or the installation of a pre-characterized module from a test bench directly into the experiment.

A thorough characterization of the components is required for this approach to perform as expected. Since the high *NA* microscope objective and its optical focus is the reference point for all other optics around the glass cell, the third chapter focused on the characterization of said objective. The objective design was motivated based on single atom imaging. After giving the basic properties of a typical objective, the design of the custom microscope objective was introduced.

Different performance parameters, like the RMS wavefront error or the PSF, were discussed during the objective characterization. A closer look into the mathematical basics of Fourier optics delivered the groundwork for a numerical simulation, which uses digital images to simulate the magnified image on a camera. While any arbitrary 2D image can be simulated, this thesis focused on the imaging of a sub-resolution nanopore. It was concluded that the finite pore size has only an insignificant impact of 17 nm on the recorded PSF.

In the experimental part of this thesis, a characterization test bench was used to scan the objective FOV with piezo translation stages and a sub-resolution nanopore with a diameter of 350 nm. Two aspects of the FOV scan were studied. First, the best recorded PSF provided a resolution of $r_{\text{min}} = (704 \pm 31)$ nm with a mean resolution of $\bar{r} = (757 \pm 5)$ nm across the FOV. Second, the angle between the mechanical and optical axis was determined to $\alpha = (2.2 \pm 1.6)$ mrad using a tweezer beam and the FOV minimum. The described methods can be used to characterize the custom objective and any other optical lens. However, it was observed that the calibration of the open-loop stages was not entirely reliable and took a significant amount of time. Therefore, it is recommended to use closed-loop stages with, for example, an optical feedback system. These results gave confidence in the specified optical performance

of the microscope objective. Consequently, the approach of a passively mounted objective as a reference for the optical modules can be pursued further in HQA.

Additionally, the resolution dependency on the truncation of the objective aperture in the Fourier plane was recorded and compared to the simulation, see Figure 3.17. Further, the effect of spherical aberrations outside of FOV and coma aberrations due to a misalignment between objective and viewport was illustrated in Figure 3.19. It was observed that the tilt between the objective and the vacuum viewport is essential for optical performance. Already small angles in the order of $< 3\,\mathrm{mrad}$ significantly distort the PSF of the 4f imaging setup. Therefore, much care should be put into aligning the objective and the glass cell. This will be made possible with precise spacers below the apparatus, tilting the experiment and the glass cell with a precision of 1 mrad [30].

In the fourth chapter, an increased cycle rate of HQA was motivated. The new 3D-MOT loading should already improve the cycle time significantly by improving upon the quantum state preparation time of the standing experiments. Motivated by fundamental theory for optical dipole interactions and thermal evaporation of ultracold ^{6}Li atoms, a new approach was proposed for increasing the experimental cycle rate. By compressing the ^{6}Li gas with a blue-detuned ring trap, the local density of the 3D-MOT atoms can be increased, which leads to a higher scattering rate while simultaneously cooling down the atom sample with evaporation. A numerical simulation was performed to provide insight into a possible experimental realization. First, the adiabatic case was examined, and the simulation showed an increased thermal scattering rate by almost a factor of two compared to the current experiments. This adiabatic case, however, does not resemble a fast transfer from ODT to MT required for an increased cycle rate. The final simulation results were given depending on the compression step size to understand a non-adiabatic compression better. Larger compression steps represent a lower total compression time, determined by evaporation and rethermalization at each iteration. A simulation resembling a fast quench (267 ms) was performed. While keeping a reasonable number of atoms in the trap, the resulting scattering rate was nearly one-third larger than in the current experiments. These simulations provide a numerical approximation and intuition for an experimental realization.

Finally, two experimental setups for a tunable ring trap were introduced using a conical axicon, which is used to generate a ring beam. This ring could be compressed quickly by either an axicon on a translation stage or two rotation stages with two mounted Moiré lenses. This new optical element consists of two phase plates, which are rotated relative to each other and will be an exciting element to introduce in a future experimental setup.

5.2 A Peek into the Future

The current construction work of HQA paves the way for many potential projects in the coming future. Therefore, the fundamental concepts behind the design process were given in this thesis. In addition, the following section will give a short peek into current and future projects.

5.2.1 Objective Characterization

Further characterization measurements could reveal more details about the capabilities of the objective. For instance, the minimal tweezer waist can be measured using a microscope objective with a short working distance and a $NA > 0.6$. This measurement would be the reference for optical tweezers produced by the objective in the future. However, a characterization of the performance while the objective is mounted in the experiment is even more crucial. As Chapter 3 shows, the alignment between the objective and the glass cell significantly impacts imaging performance. This alignment could be optimized in multiple ways. A three-axis inclinometer can measure the tilt of the glass cell and the objective with a precision of 0.1 mrad. Assuming a negligible tilt between both vertical glass cell viewports, the glass cell could be aligned parallel to the breadboard's surface. On the other hand, the alignment could be optimized optically by measuring PSF aberrations during the fluorescence imaging of single atoms.

Besides the imaging performance, the alignment to other optics on the breadboard also needs to be ensured. Here, the ability to slide the apparatus to the side enables excellent access to the objective focal plane. With the glass cell out of the way, the space between the magnetic coils is accessible for extensive characterizations of both the magnetic field and the laser beams. To this end, tools will be developed to characterize the laser beams in situ. For example, an optical module could be installed on the eighth diagnosis port (usually blocked by the glass cell) and provide optical measuring instruments like a beam profiler or a wavefront sensor. In any case, the experience gained during the design of such modules will benefit the planning of all future setups.

5.2.2 More Modules

Like the optical systems around the glass cell, HQA will carry the modular approach to the optics beneath the custom breadboard (see Figure 2.3). The vertically mounted objective is the optical interface for any laser beams requiring a high resolution. Due to the optimization for wavelengths between 532 and 1064 nm, multiple beams like the imaging light or blue and red-detuned potentials can be passed through the objective. Therefore, the 4f imaging setup's light needs to be separated into wavelengths by multiple dichroic components (see Figure 5.1). Each module interfacing with these light "intersections" will feature an intermediate image plane, which lies

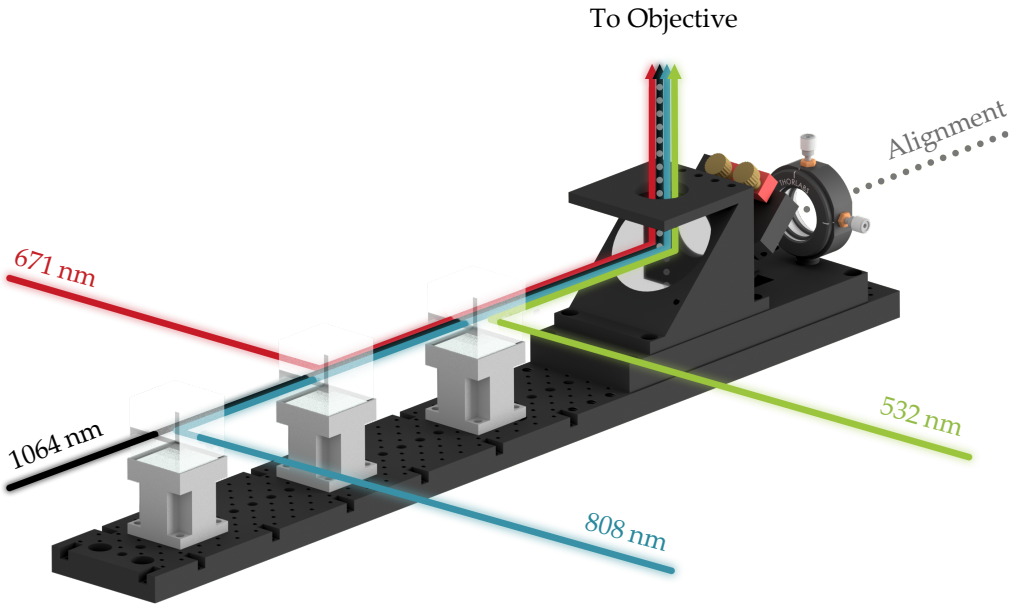

FIGURE 5.1: THE MULTI-WAVELENGTH DISTRIBUTION BREADBOARD. This breadboard will be mounted on the optical table below the objective. Three dichroic cubes split the combined beam into the respective wavelengths. The breadboard features multiple ports for optical modules that interface with the cubes.
An additional alignment beam can be sent through the back of the mirror. At the objective point mirror, this beam will be reflected into the cube setup and can be used as an alignment reference. Note that the lens from the 4f imaging setup will be included shortly before or after the mirror. This focal length of the lens will be chosen so that each port features an intermediate imaging plane.

in the focal plane of the lens before the objective. Therefore, the 4f setup magnifies each of these image planes onto the atoms. Characterizing these intermediate image planes enables an examination of the light fields projected onto the atoms already on the modules. Even the wavefronts of these light beams can be analyzed.

5.2.3 Wavefront Analysis

Wavefront analysis is a fundamental part of laser beam characterization. As discussed in Chapter 3, it allows a precise measurement of the wavefront deformation. Specific aberrations are represented by the *Zernike Polynomials* [80, 81]. If one wants to measure the aberrations of an optical element precisely, an interferometric setup is suited best. A phase unwrapping analysis of the interference pattern then yields the aberrations of the studied component [82]. A more compact tool for measuring wavefront distortions is a wavefront sensor, which allows the diagnosis of laser beams at multiple locations in the experiment. Therefore, extra space will be designated for such tools during the planning of the optical systems in HQA.

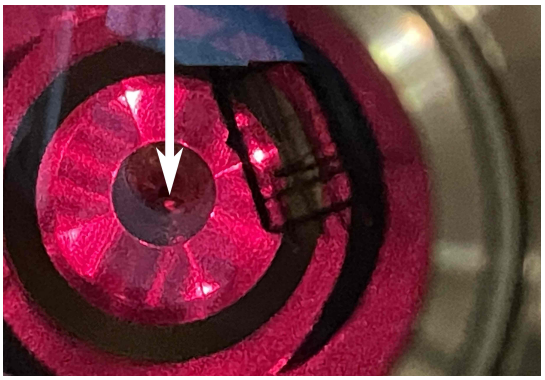

FIGURE 5.2: PICTURE OF THE FIRST ATOM CLOUD IN THE 2D-MOT. This picture was taken through the push beam viewport. The arrow marks the small atom cloud.

5.2.4 2D-MOT

During this thesis, the first 2D-MOT was realized in the experiment. Figure 5.2 shows a picture of the atom cloud taken through the push beam viewport. Shortly, this 2D-MOT will be aligned to the experiment axis toward the glass cell. Additionally, it will be optimized for a large atom number and optimal 3D-MOT loading. The details of the experimental realization of the 2D-MOT and the remaining laser traps will undoubtedly be part of future work.

5.2.5 Light Shift ODT

Currently, a new method for transferring atoms from the 3D-MOT into a micro trap is being explored in the HQA group. The working principle is illustrated in Figure 5.3. First, the atoms enter the 3D-MOT space and are cooled by scattering events with both cooler and repumper MOT transitions forming a closed cycle. However, as discussed in Chapter 4, the atoms are still too hot to load into a tight micro trap efficiently. Thus, in the current experiments, a 1064 nm crossed-beam ODT is used after the 3D-MOT in combination with evaporative cooling to reach the desired ultracold temperatures. However, the idea of the light shift ODT is to use an 808 nm tweezer ODT simultaneously with the 3D-MOT to simplify the few-body state preparation.

When an atom from the 3D-MOT enters the tweezer, its energy levels will be impacted, as described by the dressed-atom picture. The tweezer wavelength of 808 nm is closely detuned to the 813 nm 2p $\rightarrow$ 3s transition, and the 2p and 3s atom levels, therefore, experience significant light shifts, which can be adjusted to hundreds of MHz. Due to the small detuning to the 813 nm transition, the blue-detuned 808 nm light causes a significant anti-trapping potential for atoms in the 2p state (see Equation 4.2.2). Thus, as long as an atom is in the excited 2p state, it will experience a strong repulsive force, slowing the atom entering the tweezer by converting thermal into potential energy.

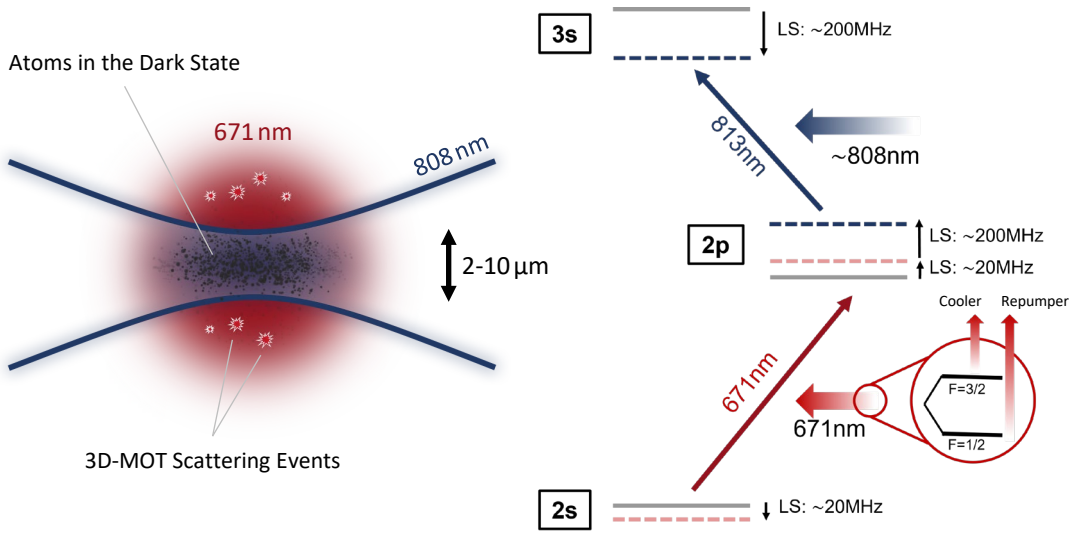

FIGURE 5.3: ILLUSTRATION OF THE 808 nm LIGHT SHIFT ODT. LEFT: The red circle illustrates the ^{6}Li cloud in the 3D-MOT. A tight tweezer (blue lines) with a wavelength of 808 nm and a diameter of 2-10 µm is switched on. Due to the light shift, the trap slows atoms in the 2p state and causes the F=1/2 ground state to become dark. Scattering events in the tweezer allow the atoms to accumulate with an increased density in the dark region.
RIGHT: The ^{6}Li level scheme for atoms in the red-detuned tweezer light. The light shift of the energy levels is depicted for each wavelength by the dashed lines.

Nevertheless, since the tweezer potential is still conservative, hot atoms would regain the lost energy while leaving the tweezer. However, suppose the atoms experience a scattering event with a 3D-MOT photon while the anti-trapping potential slows them down. In that case, they lose additional energy and decay with a finite probability into the F=1/2 ground state. Due to the light shift, cooler and repumper beams are shifted such that only the latter is in resonance with the F=3/2 ground state. Therefore, inside the 808 nm tweezer, the F=1/2 ground state is dark to the 3D-MOT light with an estimated photon scattering rate of 10^4 Hz. An atom in this dark ground state mainly experiences a trapping force by the 808 nm light, which is red-detuned to the D-line transitions. Fewer MOT-light-assisted collisions are caused by resonant light in this dark state, and the achievable densities are significantly larger than in the 3D-MOT.

Preliminary calculations show a required diameter of $2 - 10\,\mu$m for estimated loading rates in the order of magnitude of 10^5 Hz. Thus, the light shift ODT efficiently accumulates atoms, which subsequently can be loaded into a 1064 nm tweezer. Furthermore, thanks to the broadband optimization of the objective, both the 3D-MOT light and a tight red-detuned 808 nm tweezer can be imaged onto the atoms simultaneously. Whether this method can be realized in the experiment will be investigated shortly.

Bibliography

[1] Jamie Enoch et al. "Evaluating Whether Sight Is the Most Valued Sense". *JAMA Ophthalmology* 137.11 (Nov. 2019), pp. 1317–1320.

[2] H. Gross, F. Blechinger, and B. Achtner. *Handbook of Optical Systems, Volume 4: Survey of Optical Instruments*. Wiley, 2008.

[3] L. Webster Fox. "A History of Spectacles" (May 1890), pp. 1–2.

[4] David King. *History of the Telescope*. Feb. 2020.

[5] Kasper Paasch. "The history of optics: From ancient times to the middle ages". *DOPS-NYT* 1999 (Jan. 1999), pp. 5–8.

[6] O. Darrigol. *A History of Optics: From Greek Antiquity to the Nineteenth Century*. OUP Oxford, 2012.

[7] Brian Vohnsen. "A Short History of Optics". *Physica Scripta* 2004 (July 2006), p. 75.

[8] Wolfgang Lefèvre. "Inside the Camera Obscura – Optics and Art under the Spell of the Projected Image" (2007).

[9] W.J. Croft. *Under the Microscope: A Brief History of Microscopy*. Series in popular science. World Scientific, 2006.

[10] Hartmann Römer. *Theoretical Optics: An Introduction*. Feb. 2005.

[11] Chen-Lung Hung and Cheng Chin. "In situ imaging of atomic quantum gases" (2013).

[12] Jacob F. Sherson et al. "Single-atom-resolved fluorescence imaging of an atomic Mott insulator". *Nature* 467.7311 (Aug. 2010), pp. 68–72.

[13] R. B. Laughlin and David Pines. "The Theory of Everything". *Proceedings of the National Academy of Sciences* 97.1 (2000), pp. 28–31.

[14] Andrew J. Daley et al. "Practical quantum advantage in quantum simulation". *Nature* 607.7920 (July 2022), pp. 667–676.

[15] A. N. Wenz et al. "From Few to Many: Observing the Formation of a Fermi Sea One Atom at a Time". *Science* 342.6157 (Oct. 2013), pp. 457–460.

[16] Cheng Chin et al. "Feshbach resonances in ultracold gases". *Reviews of Modern Physics* 82.2 (Apr. 2010), pp. 1225–1286.

[17] Joannis Koepsell et al. "Imaging magnetic polarons in the doped Fermi - Hubbard model". *Nature* 572.7769 (Aug. 2019), pp. 358–362.

[18] J. Bardeen, L. N. Cooper, and J. R. Schrieffer. "Theory of Superconductivity". *Phys. Rev.* 108 (5 Dec. 1957), pp. 1175–1204.

[19] Marvin Holten et al. "Observation of Cooper pairs in a mesoscopic two-dimensional Fermi gas". *Nature* 606.7913 (June 2022), pp. 287–291.

[20] Randall G. Hulet, Jason H. V. Nguyen, and Ruwan Senaratne. "Methods for preparing quantum gases of lithium". *Review of Scientific Instruments* 91.1 (Jan. 2020), p. 011101.

[21] M. Bartenstein et al. "Crossover from a Molecular Bose-Einstein Condensate to a Degenerate Fermi Gas". *Phys. Rev. Lett.* 92 (12 Mar. 2004), p. 120401.

[22] Immanuel Bloch, Jean Dalibard, and Sylvain Nascimbène. "Quantum simulations with ultracold quantum gases". *Nature Physics* 8.4 (Apr. 2012), pp. 267–276.

[23] S. Jochim et al. "Bose-Einstein Condensation of Molecules". *Science* 302.5653 (2003), pp. 2101–2103.

[24] Luca Bayha et al. "Observing the emergence of a quantum phase transition shell by shell". *Nature* 587.7835 (Nov. 2020), pp. 583–587.

[25] M. H. Anderson et al. "Observation of Bose-Einstein Condensation in a Dilute Atomic Vapor". *Science* 269.5221 (1995), pp. 198–201.

[26] F. Serwane et al. "Deterministic Preparation of a Tunable Few-Fermion System". *Science* 332.6027 (Apr. 2011), pp. 336–338.

[27] Marvin Holten. "From Pauli Blocking to Cooper Pairs: Emergence in a Mesoscopic 2D Fermi Gas". PhD thesis. University of Heidelberg, 2022.

[28] Immanuel Bloch, Jean Dalibard, and Wilhelm Zwerger. "Many-body physics with ultracold gases". *Rev. Mod. Phys.* 80 (3 July 2008), pp. 885–964.

[29] Florian Schäfer et al. "Tools for quantum simulation with ultracold atoms in optical lattices". *Nature Reviews Physics* 2.8 (July 2020), pp. 411–425.

[30] Tobias Hammel. "Design and Construction of a New Experiment for Programmable Quantum Simulation using Ultracold 6Li Fermions". Master Thesis. University of Heidelberg, 2021.

[31] E Pedrozo-Peñafiel et al. "Direct comparison between a two-dimensional magneto-optical trap and a Zeeman slower as sources of cold sodium atoms". *Laser Physics Letters* 13.6 (May 2016), p. 065501.

[32] Malaika Göritz. "Characterisation of a 2D-MOT for cooling 6Li". Bachelor Thesis. University of Heidelberg, 2022.

[33] Carl Heintze. "Projection of repulsive potentials in ultracold quantum gases with a Digital Micromirror Device". Master Thesis. University of Heidelberg, 2020.

[34] Sandra Brandstetter. "Towards the Creation of Vortices in a Dipolar Bose-Einstein Condensate". Master Thesis. University of Innsbruck, 2020.

[35] Carlos L. Garrido Alzar et al. *Compensation of eddy-current-induced magnetic field transients in a MOT*. 2007.

[36] Marlene Matzke. "Design of a Compact Double Pass AOM Module". Bachelor Thesis. University of Heidelberg, 2022.

[37] R. Bowman, A. Wright, and M. Padgett. "An SLM-based Shack–Hartmann wavefront sensor for aberration correction in optical tweezers". *Journal of Optics* 12 (Nov. 2010), p. 124004.

[38] Ralf Arne Klemt. "Correlations from Microscopic to Macroscopic Quantum Systems: Interactions vs Indistinguishability". PhD thesis. University of Heidelberg, 2021, pp. 103–106.

[39] Jan Hendrik Willibald Becher. "Towards Spin and Site-Resolved, Single-Atom Imaging of 6Li Atoms in a Multiwell Potential". Master Thesis. University of Heidelberg, 2016.

[40] "Special Optics". URL: `https://specialoptics.com/`.

[41] F. Rost and R. Oldfield. *Photography with a Microscope*. Cambridge University Press, 2000, p. 76.

[42] B. E. A. Saleh and M. C. Teich. *Fundamentals of Photonics (2nd ed.)* 2003.

[43] G.R. Lemaitre. *Astronomical Optics and Elasticity Theory: Active Optics Methods*. Astronomy and Astrophysics Library. Springer Berlin Heidelberg, 2008, pp. 73–75.

[44] A. Mann. *Infrared Optics and Zoom Lenses*. SPIE tutorial texts. Society of Photo Optical, 2009, p. 16.

[45] R. Shannon. *Applied Optics and Optical Engineering V8*. Bd. 8. Elsevier Science, 2012, pp. 213–214.

[46] Ulrich Schneider. "Interacting fermionic atoms in optical lattices - A quantum simulator for condensed matter physics". eng. PhD thesis. Mainz, 2011.

[47] E.M. Slayter and H.S. Slayter. *Light and Electron Microscopy*. Cambridge University Press, 1992, p. 126.

[48] Jan Drewes. "Aufbau eines hochauflösenden optischen Systems zur Untersuchung ultrakalter Quantengase". Master Thesis. University of Hamburg, Nov. 2012, pp. 28–29.

[49] Daniel G. Smith. *Field Guide to Physical Optics*. Field Guides. 2013, p. 72.

[50] "FLIR Blackfly Technical Data". URL: `https://www.flir.de/products/blackfly-s-usb3/?model=BFS-U3-200S6C-C`.

[51] Benjamin C. Coles et al. "Characterisation of the effects of optical aberrations in single molecule techniques". *Biomed. Opt. Express* 7.5 (May 2016), pp. 1755–1767.

[52] Hossein Masalehdan et al. "Modeling of Zernike Optical Aberrations by MTF and PSF". *Biomedical Optics and 3-D Imaging* (2010), JMA98.

[53] "Norcada Nanopore Products". URL: https://www.norcada.com/products/nanopore-products/.

[54] "Thorlabs Oric Linear Translation Stage with Piezoelectric Intertia Drive". URL: https://www.thorlabs.de/newgrouppage9.cfm?objectgroup_id=12991&pn=PD1/M.

[55] "Thorlabs Achromatic Doublets". URL: www.thorlabs.com/newgrouppage9.cfm?objectgroup_id=120.

[56] S. Roth and A. Stahl. *Optik: Experimentalphysik – anschaulich erklärt*. Springer Berlin Heidelberg, 2019.

[57] Daria Kotlarek et al. "Actuated plasmonic nanohole arrays for sensing and optical spectroscopy applications". *Nanoscale* 12 (17 2020), pp. 9756–9768.

[58] Marvin Holten et al. "Observation of Pauli Crystals". *Physical Review Letters* 126.2 (Jan. 2021).

[59] Puneet A. Murthy and Selim Jochim. *Direct imaging of the order parameter of an atomic superfluid using matterwave optics*. 2019.

[60] Zachary Vendeiro et al. *Machine-learning-accelerated Bose-Einstein condensation*. 2022.

[61] Martin Gerhard Ries. "A magneto-optical trap for the preparation of a three-component Fermi gas in an optical lattice". Diploma Thesis. University of Heidelberg, 2010.

[62] Michael Eric Gehm. "Preparation of an optically-trapped degenerate Fermi gas of 6Li: Finding the route to degeneracy". PhD Thesis. Duke University, North Carolina, Jan. 2003.

[63] Rudolf Grimm, Matthias Weidemüller, and Yurii B. Ovchinnikov. "Optical Dipole Traps for Neutral Atoms" (1999), pp. 1–4.

[64] Daniel Adam Steck. *Quantum and Atom Optics*. 2022.

[65] A.E. Leanhardt et al. "Cooling Bose-Einstein Condensates Below 500 Picokelvin". *Science (New York, N.Y.)* 301 (Oct. 2003), pp. 1513–5.

[66] E. A. L. Henn et al. "Evaporation in atomic traps: A simple approach". *American Journal of Physics* 75.10 (2007).

[67] M. Arndt et al. "Observation of a Zero-Energy Resonance in Cs-Cs Collisions". *Phys. Rev. Lett.* 79 (4 July 1997), pp. 625–628.

[68] W. Demtröder. *Mechanics and Thermodynamics*. Undergraduate Lecture Notes in Physics. Springer International Publishing, 2017.

[69] Klaus M. Hueck. "A Homogeneous, Two-Dimensional Fermi Gas". PhD thesis. University of Hamburg, June 2017, pp. 51–61.

[70] "HQA Github". URL: https://github.com/lithium6hd/16-HQA-Public.

[71] G. Gauthier et al. "Direct imaging of a digital-micromirror device for configurable microscopic optical potentials". *Optica* 3.10 (Oct. 2016), p. 1136.

[72] F. M. Dickey. *Laser Beam Shaping: Theory and Techniques, Second Edition*. CRC Press, 2018, p. 442.

[73] Pierre-André Bélanger and Marc Rioux. "Ring pattern of a lens–axicon doublet illuminated by a Gaussian beam". *Appl. Opt.* 17.7 (Apr. 1978), pp. 1080–1088.

[74] "Edmund Optics Inc.: An In-Depth Look at Axicons". URL: https://www.edmundoptics.com/knowledge-center/application-notes/lasers/an-in-depth-look-at-axicons/.

[75] Danyong Zeng, William Pete Latham, and A. Kar. "Characteristic analysis of a refractive axicon system for optical trepanning". *Optical Engineering* 45.9 (2006), p. 094302.

[76] "Diffratec". URL: https://diffratec.at/.

[77] Stefan Bernet and Monika Ritsch-Marte. "Adjustable refractive power from diffractive moiré elements". *Appl. Opt.* 47.21 (July 2008), pp. 3722–3730.

[78] Stefan Bernet, Walter Harm, and Monika Ritsch-Marte. "Demonstration of focus-tunable diffractive Moiré-lenses". *Opt. Express* 21.6 (Mar. 2013), pp. 6955–6966.

[79] G. Unnikrishnan et al. "Long distance optical transport of ultracold atoms: A compact setup using a Moiré lens". *Review of Scientific Instruments* 92.6 (June 2021), p. 063205.

[80] James Wyant and Katherine Creath. "Basic Wavefront Aberration Theory for Optical Metrology". *Appl Optics Optical Eng* 11 (Jan. 1992).

[81] V. Lakshminarayanan and A. Fleck. "Zernike polynomials: A guide". *Journal of Modern Optics - J MOD OPTIC* 58 (Apr. 2011), pp. 1678–1678.

[82] Zixin Zhao et al. "2D phase unwrapping algorithm for interferometric applications based on derivative Zernike polynomial fitting technique". *Measurement Science and Technology* 26.1 (Dec. 2014), p. 017001.

A Appendix

A.1 Technical Drawings

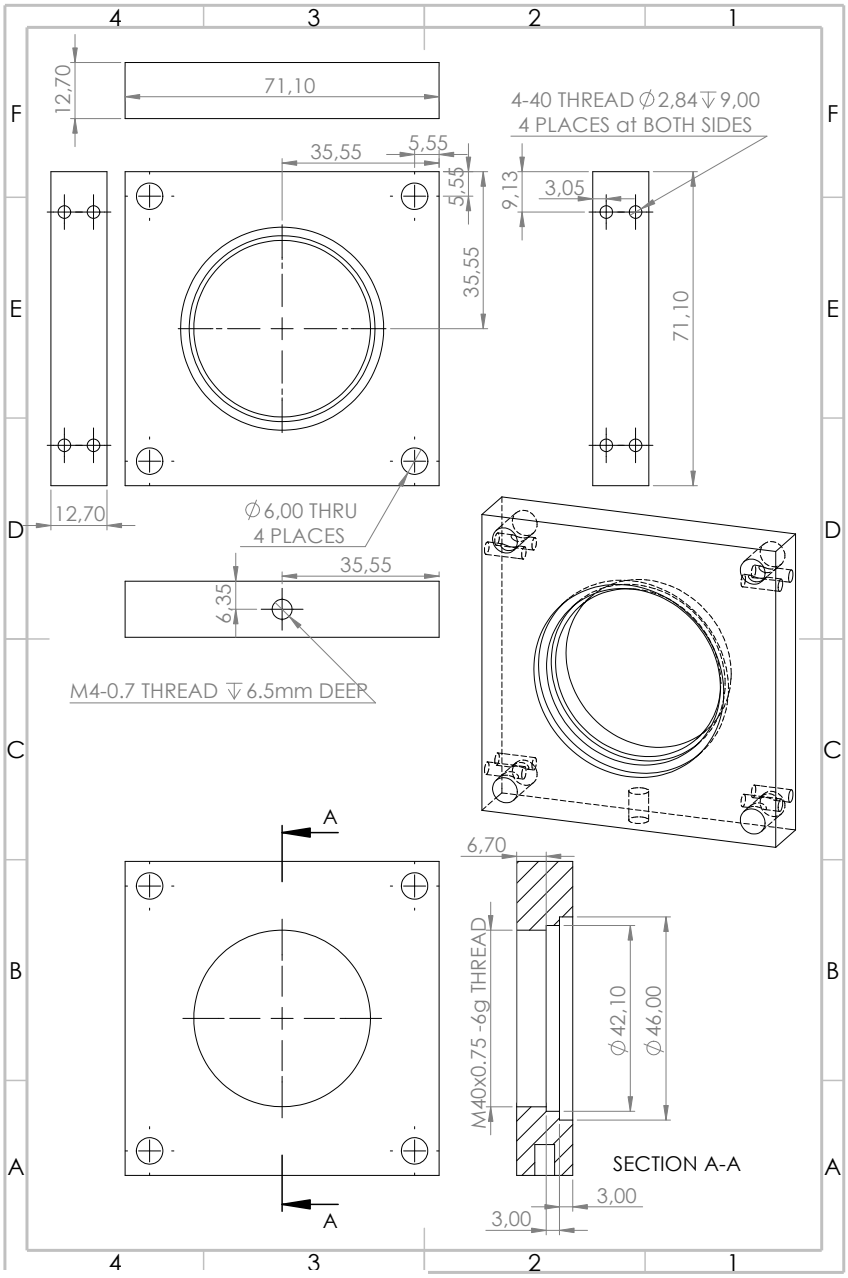

FIGURE A.1: DRAWING OF THE OBJECTIVE MOUNTING CAGE PLATE
Inside the plate are the positional and rotational referencing stops.

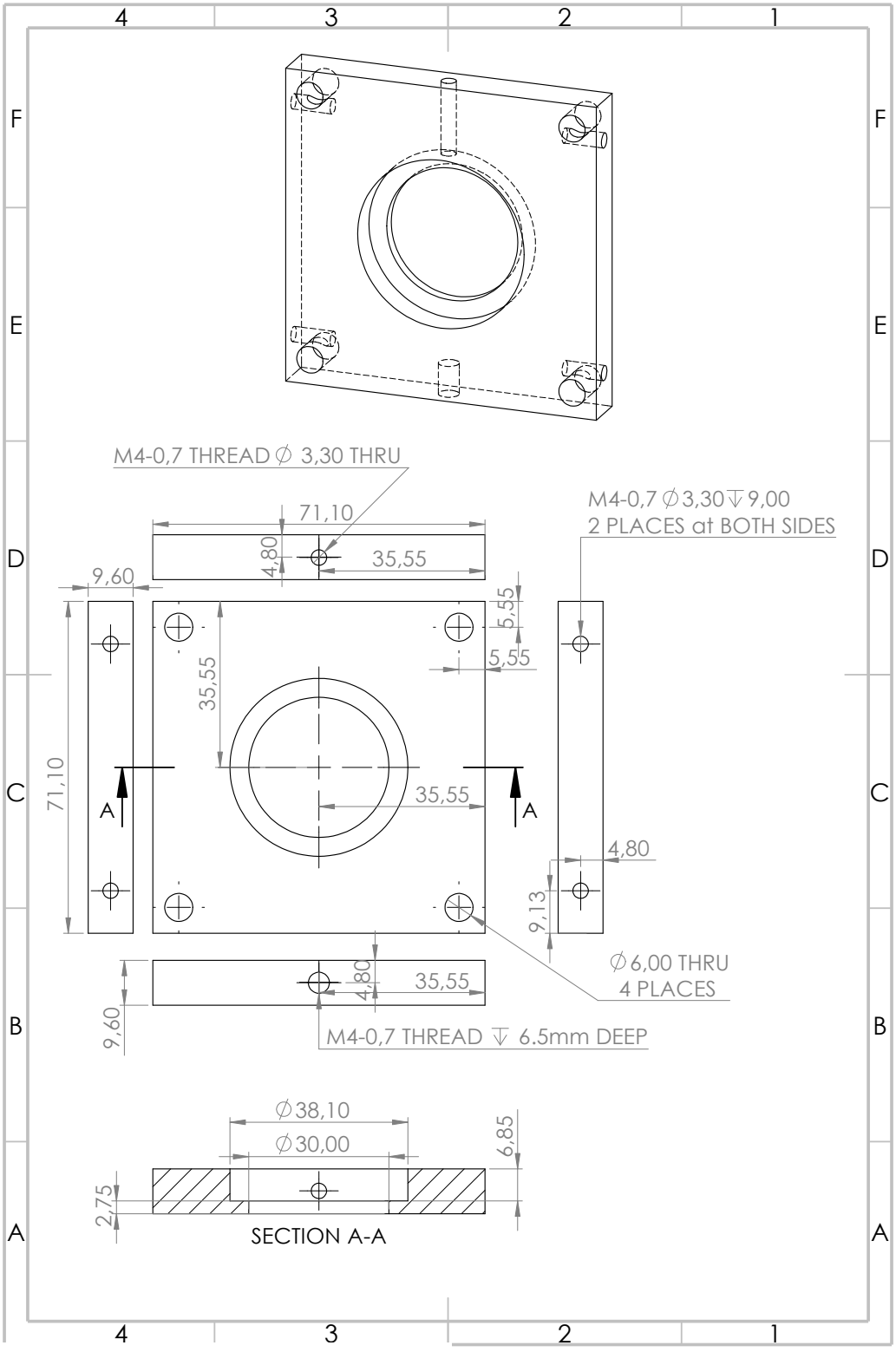

FIGURE A.2: DRAWING OF THE VIEWPORT WINDOW MOUNTING PLATE

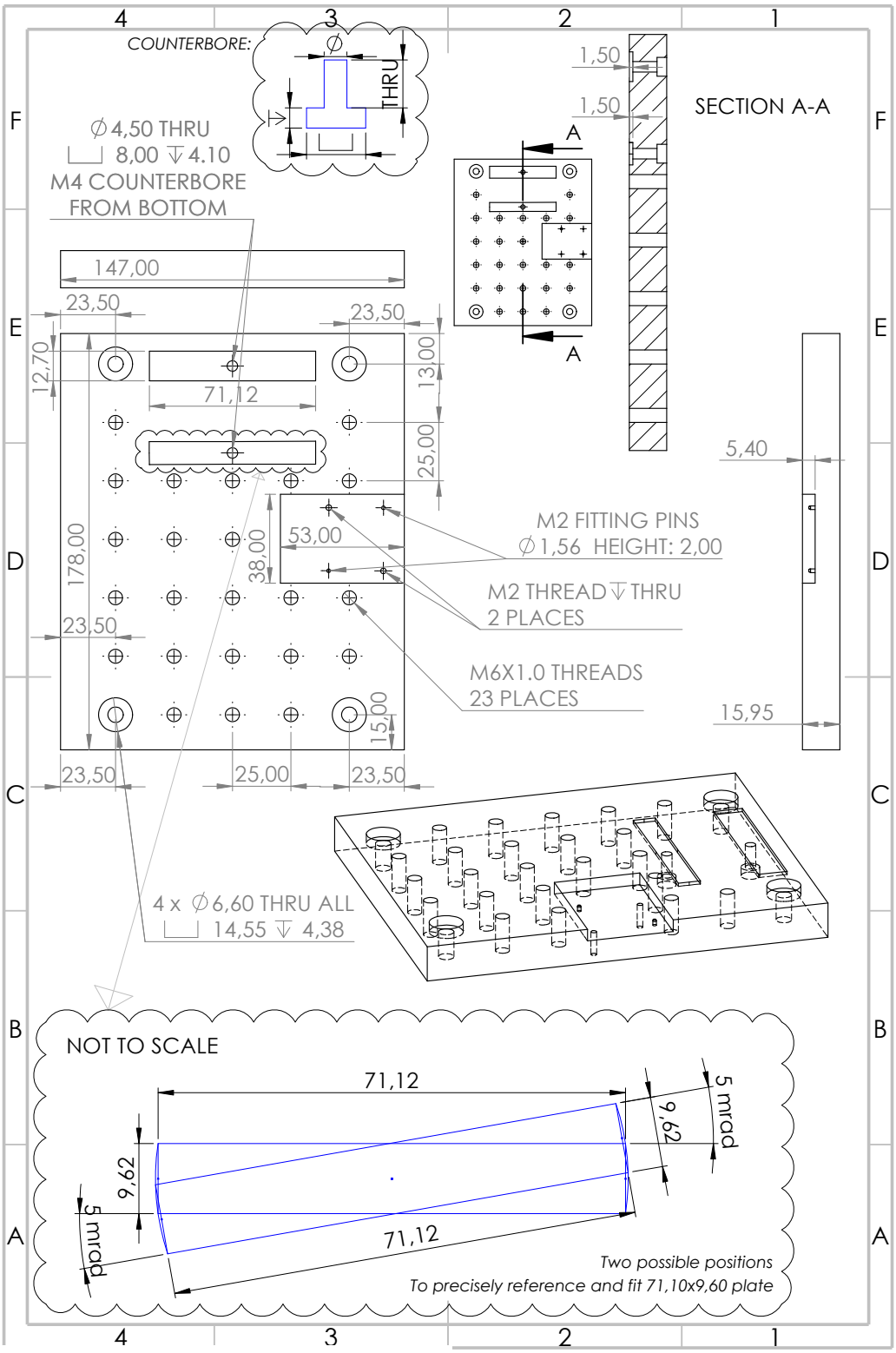

FIGURE A.3: MECHANICAL DRAWING OF THE CHARACTERIZATION TEST BENCH

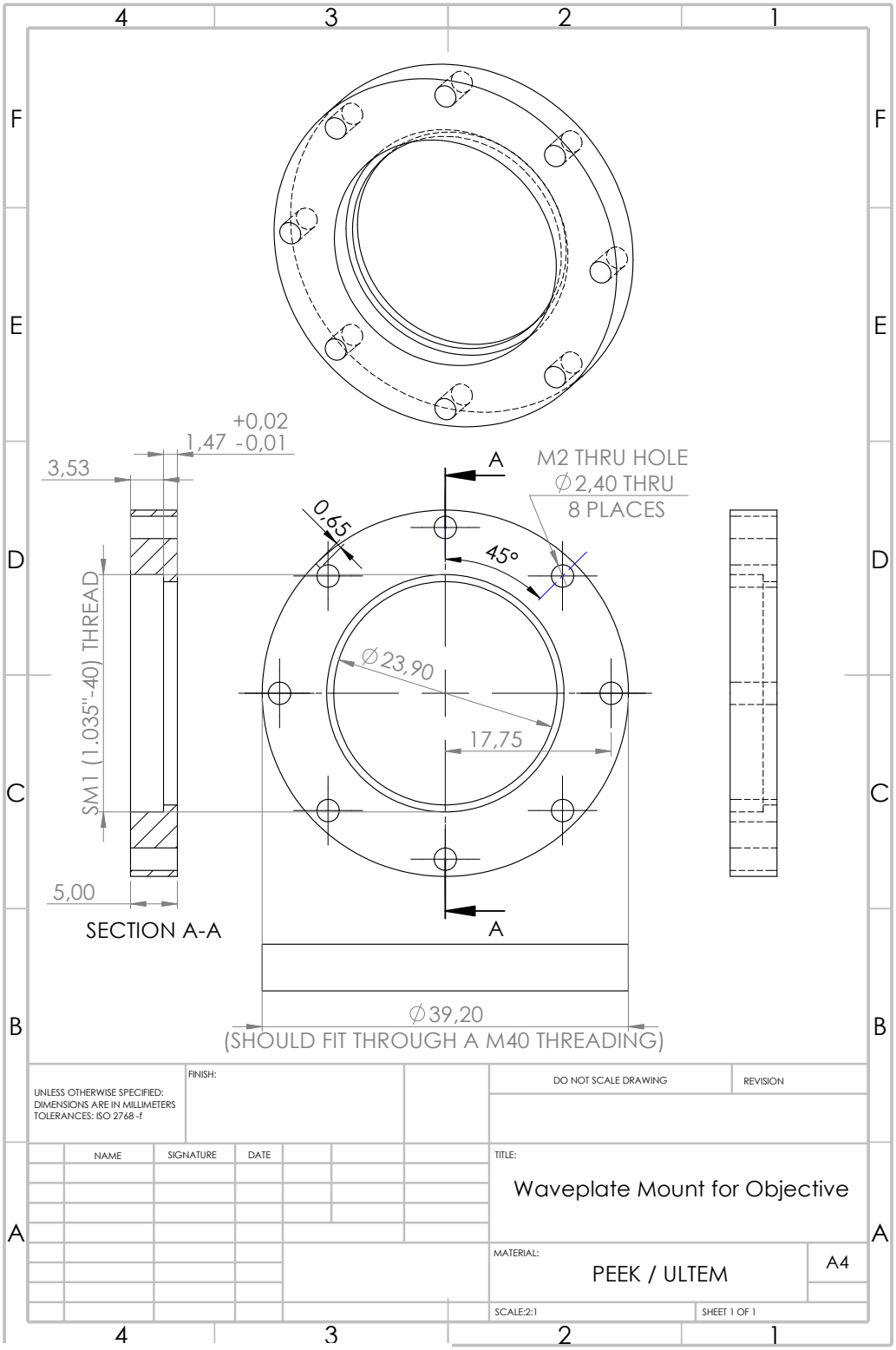

FIGURE A.4: MECHANICAL DRAWING OF THE WAVEPLATE MOUNT. This mount attaches the waveplate and the point mirror to the objective.

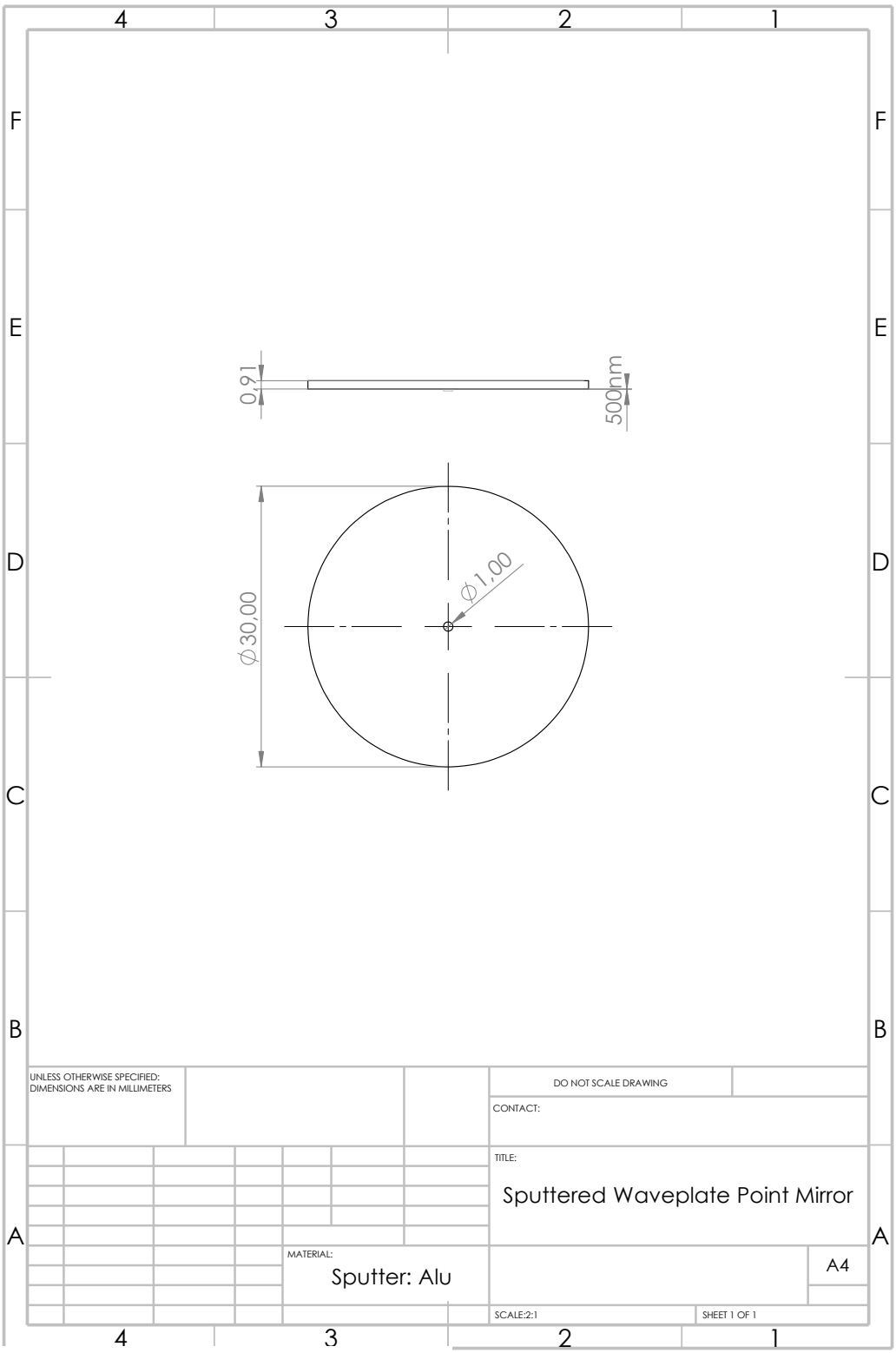

FIGURE A.5: MECHANICAL DRAWING OF THE WAVEPLATE WITH THE SPUTTERED POINT MIRROR.

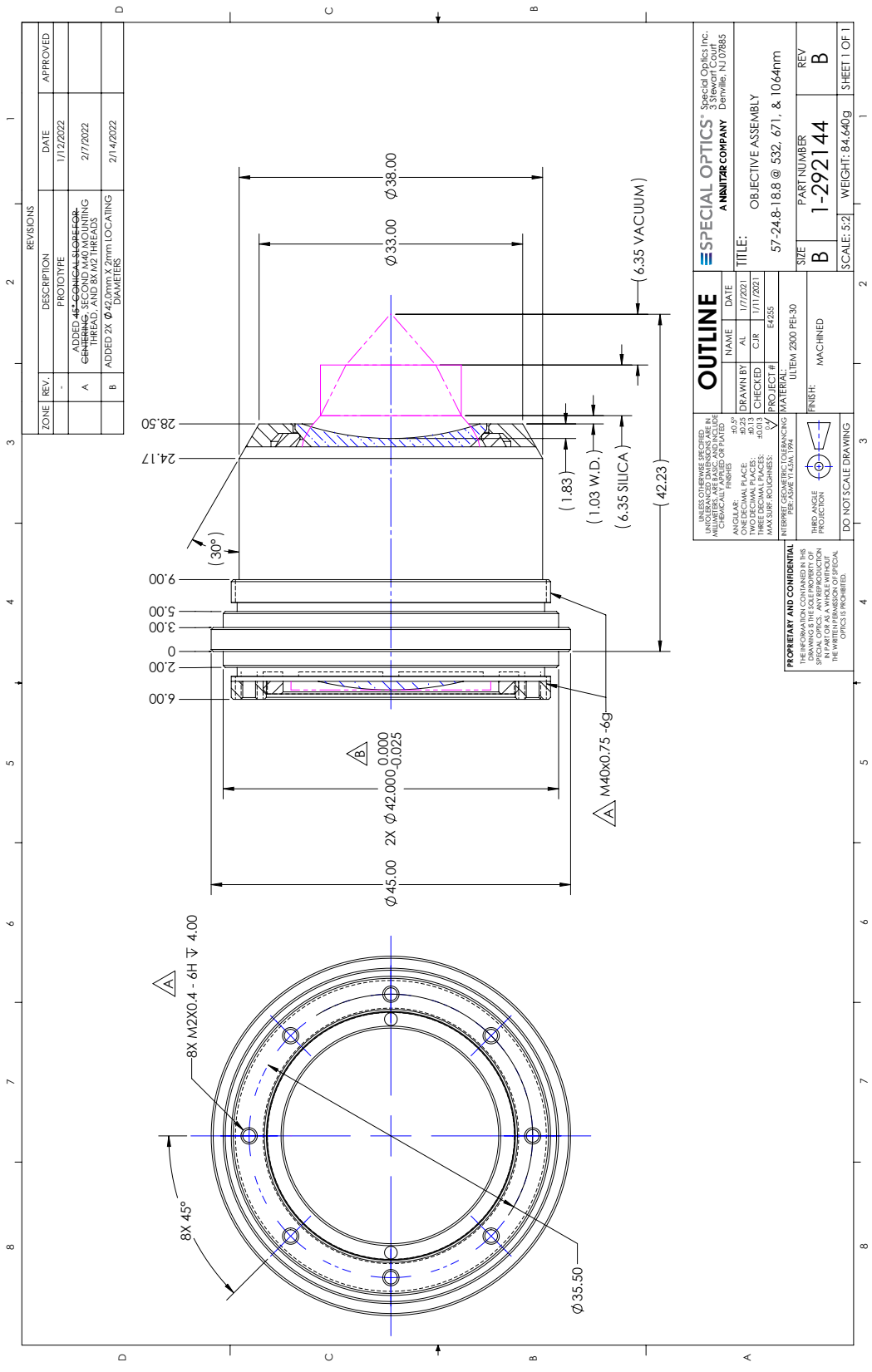

FIGURE A.6: MECHANICAL DRAWING OF THE HIGH NA OBJECTIVE. Courtesy of *Special Optics*.

A.2 Objective Inteferograms

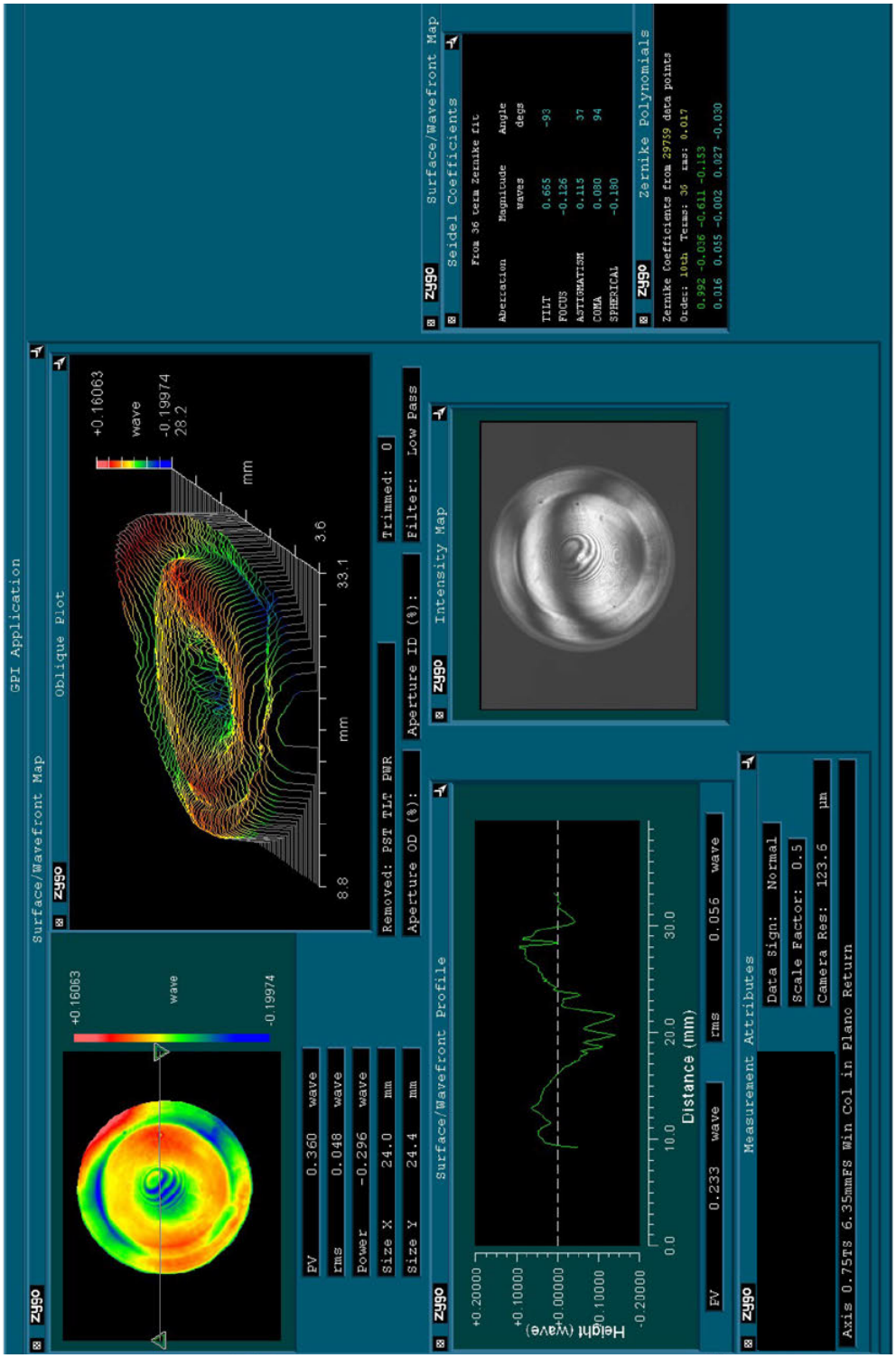

FIGURE A.7: INTERFEROGRAM OF THE OBJECTIVE ON THE OPTICAL AXIS. Performed at a wavelength of 632 nm. Courtesy of *Special Optics*.

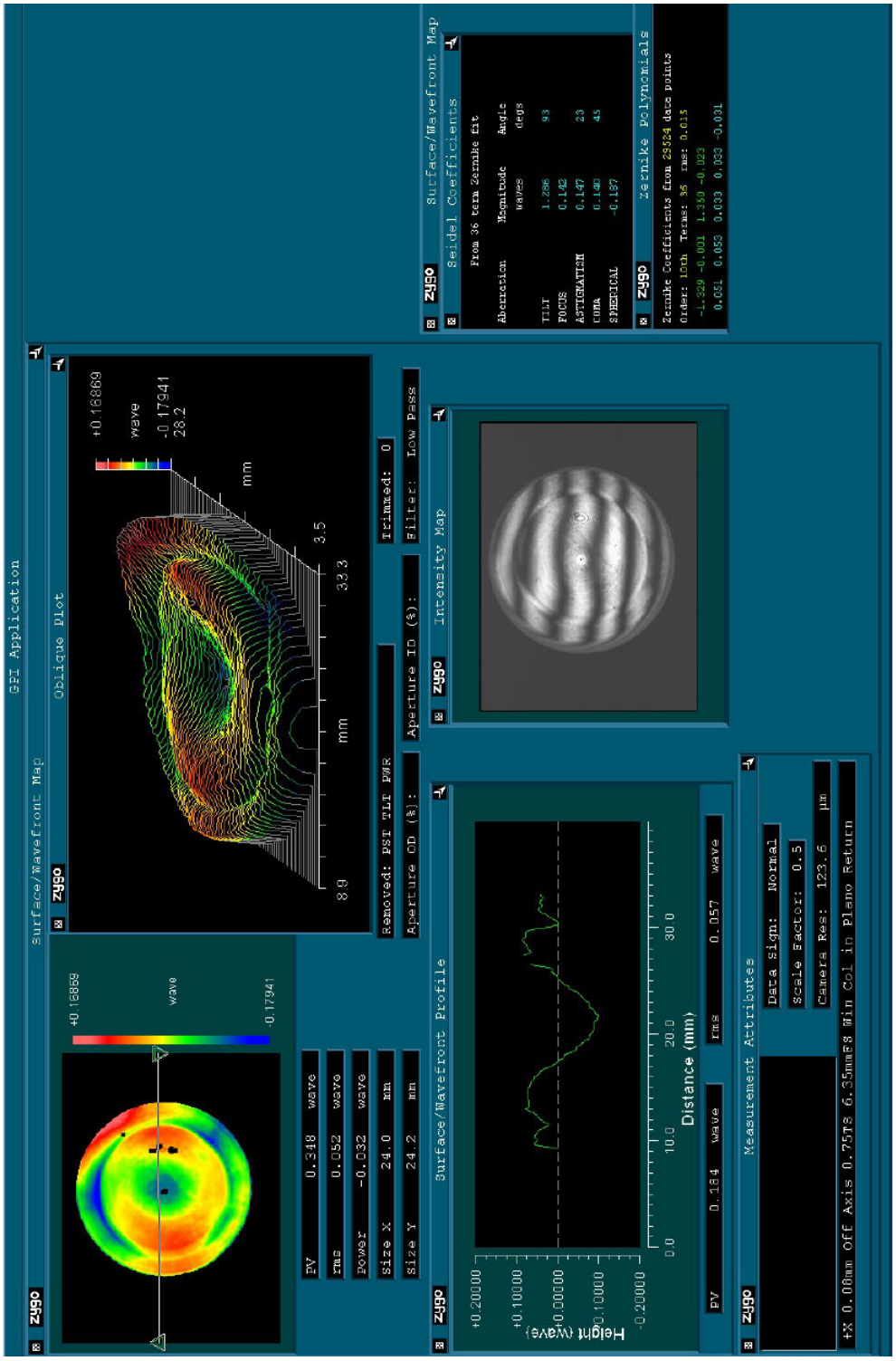

FIGURE A.8: OBJECTIVE INTERFEROGRAM OFF-AXIS IN X-DIRECTION. Performed at a wavelength of 632 nm. Courtesy of *Special Optics*.

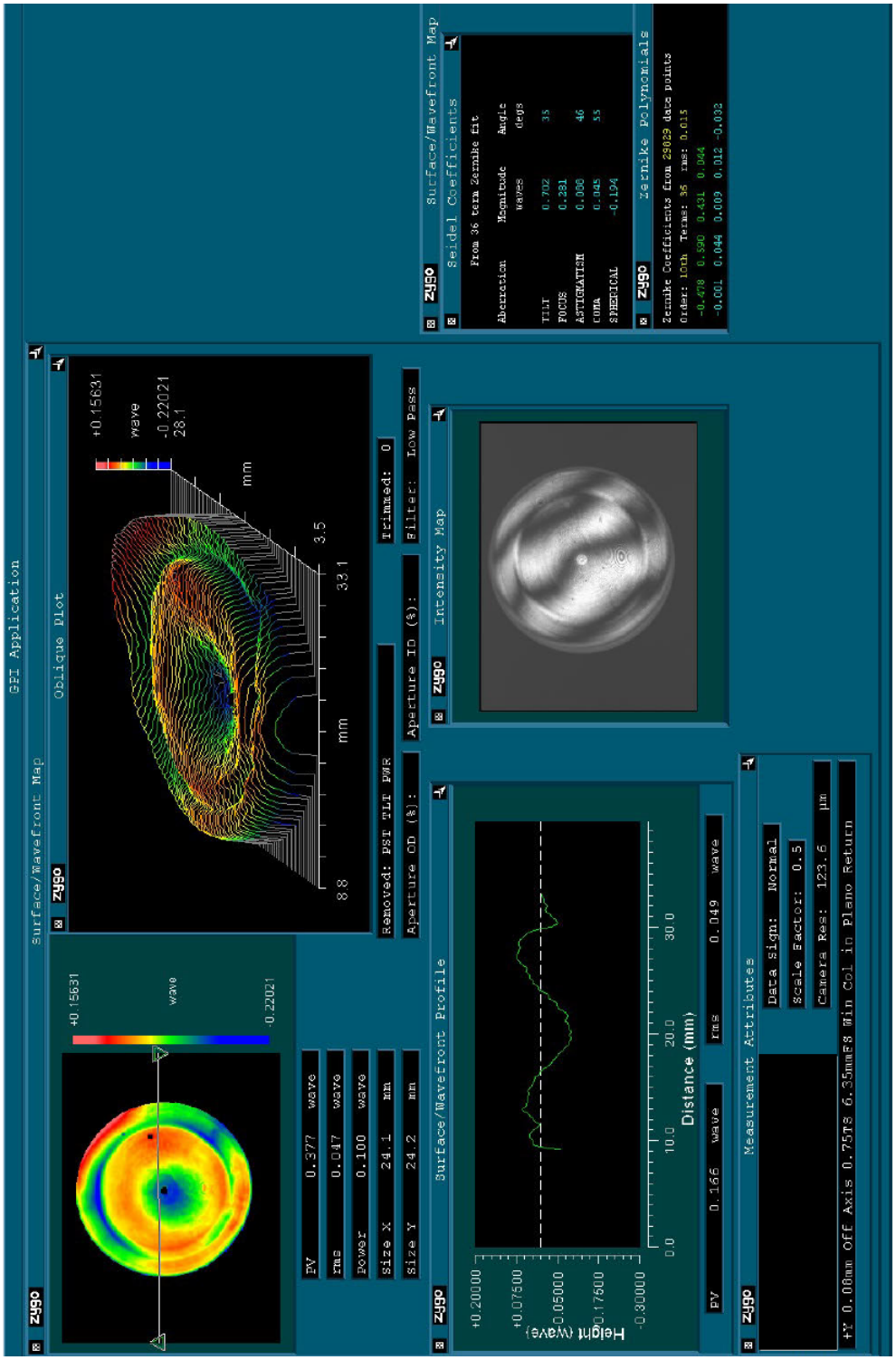

FIGURE A.9: OBJECTIVE INTERFEROGRAM OFF-AXIS IN Y-DIRECTION. Performed at a wavelength of 632 nm. Courtesy of *Special Optics*.

A.3 Pictures

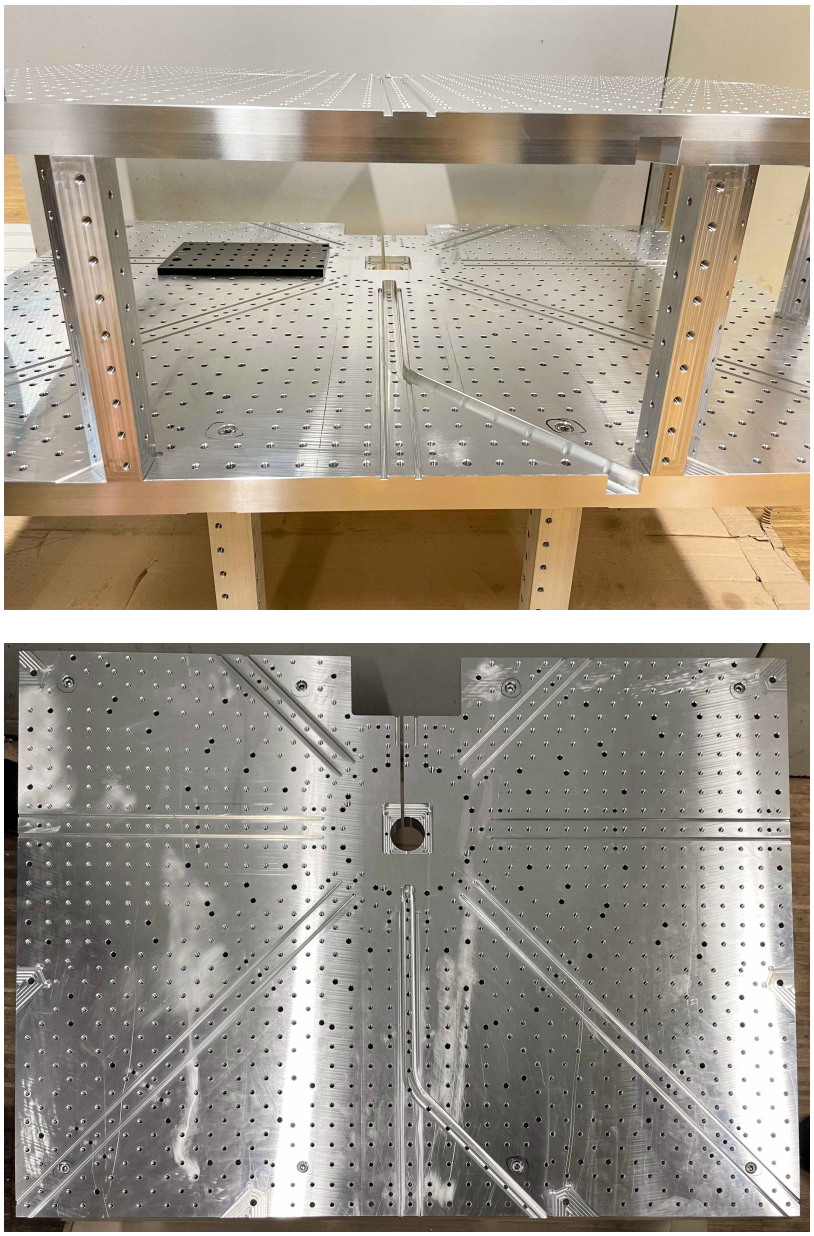

FIGURE A.10: PICTURES OF THE CUSTOM-DESIGNED BREADBOARDS. Before they will be mounted on the optical table, their material will be eloxated. These photos have been recorded in September 2022.

Danksagung

An dieser Stelle möchte ich mich bei allen bedanken, die mich während der Erstellung dieser Masterarbeit unterstützt und motiviert haben.

Zuerst gebührt mein Dank Selim, der mir diese Arbeit in seiner Gruppe ermöglicht hat. Danke für die hervorragende Betreuung, deine zugängliche Art und die vielen aufschlussreichen Gespräche.

Außerdem möchte ich Lauriane Chomaz für die Übernahme der Zweitkorrektur danken. Ich danke auch Matthias Weidemüller für die klärenden Diskussionen und das Liefern maßgebender theoretischer Grundlagen. Außerdem möchte ich Philipp P. für das Begleiten meiner ersten Schritte im Objektivdesign danken.

Ein besonderer Dank gebührt Tobias und Max. Danke, dass ihr keine Mühe gescheut habt, zu dieser Arbeit und meiner Freude im Team HQA beizutragen. Ich bedanke mich für all die guten Ratschläge, die spaßigen Momente und die beste Betreuung, die ich mir vorstellen kann.

Ebenso möchte ich mich bei der ganzen Ultracold Gruppe für eine herzliche Aufnahme bedanken. Mein Dank gilt Philipp L. für die vielen schönen Partien Beachvolleyball und Carl für die kompetitiven Skatrunden, die den Nachmittag aufgelockert haben. Ich bedanke mich auch bei Vivienne, Leo, Malaika und Marlene für die gemeinsame Zeit am HQA Projekt. Danke auch Sandra für die klärenden Diskussionen und das gewissenhafte Nachfüllen des Snackschrankes. Ebenfalls bedanke ich mich bei Johannes für eine sichere Rettung durch die Feuerwehr. Ich möchte mich auch bei allen danken, die diese Arbeit Korrektur gelesen haben.

Ein besonderer Dank gilt meinen Heidelberger Freunden David, Lukas und Felix für die zahlreichen unterhaltsamen Spieleabende und die emotionale Unterstützung in schwierigen Zeiten.

Insbesondere möchte ich mich bei meinen Bandkollegen David, Paul und Corbin bedanken. Ihr seid zu meiner Familie geworden und ohne diesen regelmäßigen Rückzugsort, die befreienden Gespräche und vor allen Dingen die Musik hätte ich mein Studium wahrscheinlich in Regelstudienzeit, aber dafür nicht mit intakter psychischer Gesundheit geschafft.

Schließlich möchte ich mich noch bei meiner Familie bedanken, deren stetige Unterstützung es mir ermöglicht, meine Träume zu verfolgen.

Declaration of Authorship

I, Micha BUNJES, declare that this thesis titled, "High-Resolution Optics for Modular Quantum Simulation" and the work presented in it are my own. I confirm that:

- Where I have consulted the published work of others, this is always clearly attributed.
- Where I have quoted from the work of others, the source is always given. With the exception of such quotations, this thesis is entirely my own work.
- I have acknowledged all main sources of help.

Signed: 

Date: 26.09.2022